INVESTIGATION OF INERTIAL PARTICLE PHENOMENA IN HOMOGENEOUS ISOTROPIC TURBULENCE

A Dissertation

Presented to the Faculty of the Graduate School

of Cornell University

in Partial Fulfillment of the Requirements for the Degree of

Doctor of Philosophy

by

Juan Pablo de Lima Costa Salazar

May 2010

INVESTIGATION OF INERTIAL PARTICLE PHENOMENA IN HOMOGENEOUS ISOTROPIC TURBULENCE

Juan Pablo de Lima Costa Salazar, Ph.D.

Cornell University 2010

This work is concerned with the study of inertial particles in homogeneous isotropic turbulent flows. In the first part we present the first detailed comparisons between experiments and direct numerical simulations (DNS) of inertial particle clustering, measured through the radial distribution function (RDF) and the correlation dimension. In a comparison of near-perfect parameter overlap, we observe good agreement between the RDF predictions of the DNS and the experimental observations. Our results provide important guidance on ways to improve future measurements. In the second part we use a high-resolution DNS at a low and a moderate Reynolds number to investigate inertial particle relative velocity statistics within the dissipation range and the inertial range of turbulence. Within the dissipation range we highlight the second-order longitudinal velocity structure function and study scaling properties as a function of Stokes number, a non-dimensional measure of particle inertia. We find clear evidence of so-called 'caustics' and also find support for the existence of a critical Stokes number, St_c, below which the influence of caustics is negligible, in agreement with recently published work. In the inertial range we calculate the scaling exponents of the velocity structure function of order 2 through 8 in the longitudinal and transverse directions. We find that with increasing inertia, the longitudinal structure function scaling exponents become more intermittent-like, in contrast to well known examples of single-point inertial particle statistics such

as acceleration. In addition, we find that the effect of filtering is primarily responsible for the observed behavior. In the third and final part we use DNS to investigate acceleration statistics of inertial particles. Specifically, we address the importance of biased sampling and biased filtering on the tails of the acceleration probability density function as a function of Stokes number. Our findings show that while biased sampling is the dominant effect, biased filtering is still relevant even at Stokes numbers as low as 0.2. Further, we attempt to uncover what aspects of the underlying flow are controlling particle acceleration statistics by studying the relationship between flow topology and inertial particle accelerations. This work highlights the interesting array of phenomena induced by inertia.

BIOGRAPHICAL SKETCH

Juan Pablo de Lima Costa Salazar was born on March 22, 1978 in Rio de Janeiro, Brazil, son of Claudia and Leonardo. Much of his childhood was spent in East Lansing, Michigan, and Urbana, Illinois, as his parents navigated through graduate school. In 1990 Juan moved with his mother to Florianópolis, Brazil, where he attended high-school, graduating in 1995. In 1996 Juan began his undergraduate education at the *Universidade Federal de Santa Catarina* (UFSC), Florianópolis, Brazil, graduating in October of 2002 with high honors in Mechanical Industrial Engineering. During this period he received a scholarship from the CAPES agency of the Brazilian Ministry of Education to study at the *Technische Hochschüle* in Karlsruhe, Germany, from January 1999 through February 2000. He later returned to Germany in August 2001 as an intern at Bosch Thermothechnik GmbH, located in the outskirts of Stuttgart, for a six-month period. In March 2003 Juan received a scholarship from the CAPES agency to pursue a masters degree, receiving a Masters in Science in Mechanical Engineering from UFSC in July 2004. In June 2004 he was awarded a scholarship from the CAPES agency to pursue a doctorate degree in Aerospace Engineering at Cornell University under the tutelage of Professor Lance R. Collins, which he began in August 2004. Juan has wholeheartedly enjoyed his stay in Ithaca and its beautiful surroundings. During his stay in upstate New York he has become an endurance cyclist and runner and is proud to have ridden around each of the 11 Finger Lakes, always departing from Ithaca.

To my mother, for putting me on this path a long time ago and to Grazie, for putting up with me.

ACKNOWLEDGEMENTS

First and foremost I would like to thank my advisor Lance R. Collins for his support and guidance throughout the years. He has made incredible efforts to make himself available to me and his other students in spite of his administrative obligations as department chair. The experience of being his graduate student could not have been more rewarding, even during the tough times when codes are not working and results make no sense. He has always been patient and insightful, and I am very grateful. This work would have not been possible without him.

I am very much indebted to Professor Hui Meng and her team at the Laser Flow Diagnostics Laboratory at SUNY-Buffalo, in particular Jeremy de Jong, Lujie Cao and Scott Woodward. They have been an integral part of my research, especially during my first years at Cornell when we worked hard to make sensible comparisons between experiments and simulations. Our weekly interactions were very beneficial and have allowed me an intimate glance at the life of an experimentalist.

I would also like to thank my other committee members Stephen B. Pope, Donald Koch and Zellman Warhaft, people which I admire and with whom I have had very pleasant interactions over the years. In particular I am very happy to have had the fortune to attend the classes Introduction to Fluid Mechanics, Analysis of Turbulent Flows and Computational Combustion offered by Professor Pope in the graduate program as well as the Aerosols & Colloids class offered by Professor Koch. These courses provided a sound basis upon which I could build. To Zellman I thank all the useful discussions during our Lagrangian meetings and his great sense of humor, along with all his published work, which combines scientific rigor and eloquence so masterfully.

Fellow graduate students and postdocs have been a source of inspiration and amusement during my stay in Ithaca. I thank Kamaraju Kusumanchi for his help with all programming and math related, Juan Camilo Isaza Betancourt for the many discussions about turbulence, and Sarma Rani and Shi Jin for the help during my learning phase of the particle code. In addition, many have become true friends, with whom I hope to stay connected throughout my life. Among them are Bernardo Cordovez, Edgar Cuji and Vishal Tandon.

To my mother and extended family Sonia I thank the example of work ethic. It has been a long time since I wrote my first essay in 4th grade, a biographical piece on an important historical figure. I chose Karl Marx. Since there were no children-friendly books available my mom and I made frequent trips to the library at the University of Illinois to delve in real books. It was my first research assignment and the beginning of my academic life. Ever since, this is all that I wanted to do.

I am deeply thankful to Grazie, my companion during my years at Cornell. She has always been supportive of my dreams and adventures, academic or not. Her daily gestures of affection gave me solace when nothing seemed to work. I will cherish our moments in Ithaca for the rest of my life. Without her love and support this would have been so much more difficult.

Finally, I am immensely grateful to the CAPES agency of the Brazilian Ministry of Education. I have received multiple scholarships since my undergraduate years and I would most likely not be here without their support.

TABLE OF CONTENTS

LIST OF TABLES

LIST OF FIGURES

CHAPTER 1

EXPERIMENTAL AND NUMERICAL INVESTIGATION OF INERTIAL PARTICLE CLUSTERING IN ISOTROPIC TURBULENCE*

This paper presents the first detailed comparisons between experiments and direct numerical simulations (DNS) of inertial particle clustering in nearly isotropic "box turbulence." The experimental system consists of a box 38 cm in each dimension with fans in the eight corners that sustain nearly isotropic turbulence in the center of the box. We inject hollow glass spheres with a mean diameter of 6 microns and measure the locations of several hundred particles in a 1 cm^3 volume in the center of the box using three-dimensional digital holographic particle imaging. We observe particle concentration fluctuations that result from inertial clustering (sometimes called 'preferential concentration'). The radial distribution function (RDF), a statistical measure of clustering, has been calculated from the particle position field. We select this measure because of its relevance to the collision kernel for particles (e.g., see Sundaram & Collins 1997). DNS of the equivalent system, with nearly perfect parameter overlap, also have been performed. We observe good agreement between the RDF predictions of the DNS and the experimental observations, despite some challenges in the interpretation of the experiments. The results provide important guidance on ways to improve the measurement.

*Salazar JPLC, de Jong J, Cao L, Woodward SH, Meng H, Collins LR. 2008. Experimental and numerical investigation of inertial particle clustering in isotropic turbulence. *J. Fluid Mech.* 600:245-56

1.1 Introduction

Numerical simulations of inertial particles in turbulence have shown that the particles tend to cluster outside of vortices, in the high-strain regions of the flow (Eaton & Fessler (1994), Squires & Eaton (1991)). Maxey (1987) correctly attributed this effect to the centrifugal force acting on the particles in regions of high rotation, and showed that the divergence of the *particle* velocity is *not* zero, but is proportional to the local difference between the squares of the rate-of-strain and rate-of-rotation tensors. The effect can give rise to rather dramatic non-uniformity of the particle concentration field. Particle clustering can influence a broad range of aerosol processes, such as particle settling (Aliseda et al. (2002), Wang & Maxey (1993)), evaporation/condensation (Shaw et al. (1998)), and interparticle collisions (Wang et al. (2000)). Sundaram & Collins (1997) identified the radial distribution function (RDF), evaluated at contact, as the precise correction to the collision kernel to account for clustering. The RDF is a measure of the probability of finding a second particle at a given separation distance from a test particle (McQuarrie (1976)). The RDF can be computed from a field of M particles by binning the particle pairs according to their separation distance, and calculating

$$g(r_i) = \frac{N_i/\Delta V_i}{N/V} \,, \tag{1.1}$$

where N_i is the number of particle pairs separated by a distance $r_i \pm \frac{\Delta r}{2}$, ΔV_i is the volume of the discrete shell located at r_i, $N = \frac{1}{2}M(M-1)$ is the total number of pairs and V is the total volume of the system. The subscript 'i' is the discrete index and does not refer to a vector quantity. Direct numerical simulations (DNS) have shown the RDF can reach values in excess of 100 for certain parameter values (Reade & Collins (2000a), Wang et al. (2000)). Subsequent numerical work

has quantified the dependence of the RDF on the particle Stokes number, and, to a lesser extent, the Reynolds number (Collins & Keswani (2004)). Theoretical investigations have yielded predictions of the RDF under a variety of assumptions (Chun et al. (2005), Falkovich et al. (2002), Zaichik & Alipchenkov (2003)). All of the results suggest that inertial clustering could profoundly influence the evolution of the size distribution of a coalescing aerosol.

One important application where particle clustering may play an important role is in the development of convective clouds in the atmosphere. Cloud droplets below 20 μm in diameter are known experimentally to have fairly low collection efficiencies; hence, most cloud models assume droplets grow by condensation alone until they reach a critical size. However, these models underpredict the breadth of the droplet size distribution and overpredict the time required for warm rain initiation by as much as one order of magnitude (Shaw (2003)). Shaw et al. (1998) hypothesized that droplet clustering may induce vapor supersaturation fluctuations that will broaden the droplet size distribution. Falkovich et al. (2002) argued that clustering-enhanced collisions may compensate for the lower efficiency of smaller droplets. Additionally, Reade & Collins (2000b) observed that particle inertia tends to broaden the size distribution of a coalescing aerosol.

Although the above arguments provide plausible explanations for the acceleration of cloud development in the atmosphere, quantitative measurement of inertial clustering remains largely based on DNS. There have been a few experimental images of clustered particles in turbulence (Eaton & Fessler (1994)); however, only recently have those measurements become quantitative. Wood et al. (2005) measured a two-dimensional projection of the RDF of entrained

particles in a turbulence box by shining a laser sheet at the particles, and measuring their x–y locations with a camera. They found clear evidence of clustering, albeit at levels lower than those found in the DNS study by Sundaram & Collins (1999). One possible explanation for the discrepancy is an attenuation effect due to the reduced dimension of the measurement, as described by Holtzer & Collins (2002). Saw et al. (2007) measured the one-dimensional RDF by sampling droplet arrivals at a fixed volume in a wind tunnel. Arrival statistics were used to compute the one-dimensional projection of the RDF, which too is susceptible to the error discussed in Holtzer & Collins (2002).

In this paper, we compare heretofore unavailable experimental measurements of the *three-dimensional* RDF of particles in a 'turbulence box' with DNS under conditions of excellent parametric overlap. These unique measurements were conducted using a cutting-edge digital holographic imaging technique, which provides three-dimensional particle locations. Spatial accuracy of the particle positions is such that the RDF can be calculated reliably up to $r/\eta \sim 1$, where $\eta = (\nu^3/\epsilon)^{1/4}$ is the Kolmogorov length scale, ν is the fluid kinematic viscosity and ϵ is the turbulent energy dissipation rate. These measurements suffer from none of the effects described above due to projection of the RDF to lower dimensions. The particle size distribution is moderately broad and, due to resolution limitations, the holographic imaging system may not be able to capture the smaller particles. We input an equivalent distribution of particles into the DNS that closely matches the distribution in the experiment, and then apply a high-pass particle size threshold filter to the DNS results to mimic the filtering done by the digital camera.

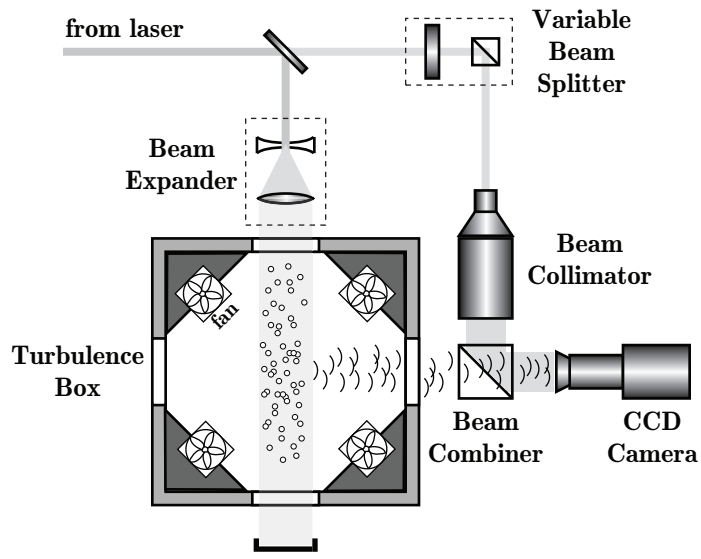

Figure 1.1: Schematic of the turbulence box and holographic imaging setup.

1.2 Experimental Method

1.2.1 Flow and Particle Characteristics

The turbulent flow facility consists of an air chamber ('turbulence box') that is 38 cm across, with fans in the eight corners of the box to produce the turbulent flow field (see figure 1.1). The design of the box is very similar to that used by Birouk et al. (1996). The flow field in the central region of the the box has been shown by de Jong et al. (2007) to be homogeneous and isotropic. Flow velocity statistics were obtained by particle image velocimetry (PIV), with use of a Spectra-Physics PIV-400 dual, injection-seeded Nd:YAG laser (400 mJ/pulse at 532 nm, 8 ns pulse width) and a sharpVISION 1300 CCD camera (10 bit, 1280x1024, 6.7 μm pixel array). The setup is able to reach a Reynolds number based on the Taylor microscale, R_λ, up to 187. However, due to concerns with achieving stationary statistics for the RDF that will be discussed later, we have limited the

Table 1.1: Table of flow parameters. Roman numerals indicate the different comparison conditions. We show 95% confidence intervals that were estimated using the method described by Benedict & Gould (1996) for the turbulence velocity statistics and Kline & McClintock (1953) for ϵ and related quantities. Further details can be found in de Jong et al. (2007).

	units	I	II	III
Experiment				
Horizontal r.m.s velocity u_{rms}	ms^{-1}	0.346 ± 0.005	0.529 ± 0.008	0.672 ± 0.010
Vertical r.m.s velocity v_{rms}	ms^{-1}	0.378 ± 0.005	0.582 ± 0.008	0.764 ± 0.011
Turbulent kinetic energy k	m^2s^{-2}	0.191 ± 0.004	0.449 ± 0.009	0.743 ± 0.016
Turbulent intensity $u' = \sqrt{2/3k}$	ms^{-1}	0.357 ± 0.004	0.547 ± 0.006	0.704 ± 0.007
Turbulent energy dissipation rate ϵ	m^2s^{-3}	1.33 ± 0.21	4.90 ± 0.76	11.0 ± 1.73
Large eddy length scale $L = k^{3/2}/\epsilon$	cm	6.29 ± 0.99	6.13 ± 0.96	5.82 ± 0.94
Large eddy time scale $T_e = L/u'$	s	0.18 ± 0.028	0.11 ± 0.018	0.08 ± 0.013
Kolmogorov length scale η	μm	226 ± 8.7	163 ± 6.3	133 ± 5.2
Kolmogorov time scale τ_η	10^{-3}s	3.37 ± 0.27	1.76 ± 0.14	1.17 ± 0.09
Kolmogorov velocity scale u_η	ms^{-1}	0.067 ± 0.003	0.093 ± 0.004	0.114 ± 0.005
Taylor micro-scale λ	mm	4.66 ± 0.37	3.72 ± 0.29	3.19 ± 0.26
Reynolds number R_λ	—	110 ± 9	135 ± 12	149 ± 13
Direct Numerical Simulations				
Reynolds number R_λ	—	108	134	147

maximum Reynolds number in the experiments to $R_\lambda \sim 150$. A summary of all of the relevant flow parameters for each of the conditions investigated is given in table 1.1. The turbulent energy dissipation rate ϵ reported in table 1.1 is calculated via the longitudinal second-order structure function $D_{LL}(r)$, assuming inertial subrange scaling $D_{LL}(r) = C_2(\epsilon r)^{2/3}$ with a universal constant $C_2 = 2.1$ (Sreenivasan (1995)). Figure 1.2 shows two independent measurements of the second-order longitudinal structure function in compensated coordinates, such that the ordinate value of the plateau region is ϵ. Refer to de Jong et al. (2007) for a complete discussion of the measurement of the dissipation rate in our system.

DNS has shown that the degree of particle clustering is a strong function of the particle Stokes number, defined here as $St \equiv \tau_p/\tau_\eta$, where $\tau_p \equiv \beta d^2/18\nu$ is the viscous response time of the particle, $\tau_\eta \equiv \sqrt{\nu/\epsilon}$ is the Kolmogorov time

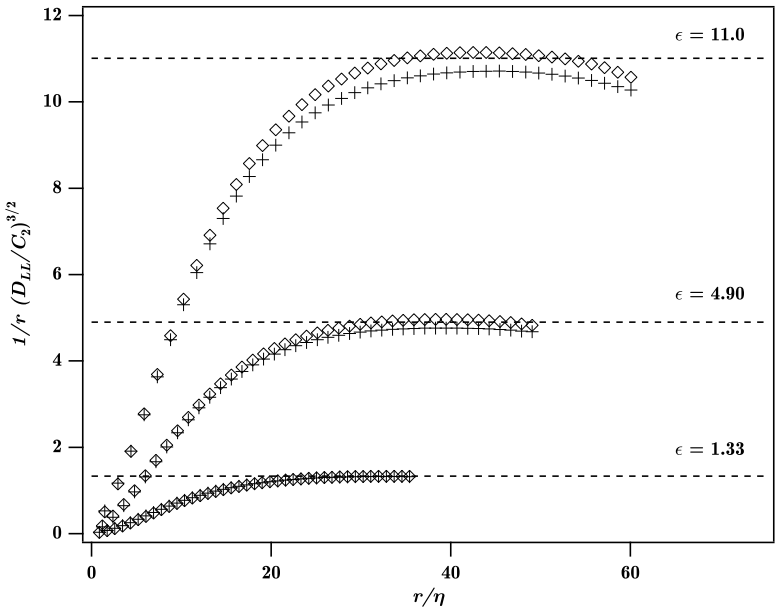

Figure 1.2: Compensated second order longitudinal structure functions (D_{LL}) for the different flow conditions. Symbols indicate independent realizations of the experiment.

scale, $\beta \equiv \rho_p/\rho$ is the ratio of the particle density to the fluid density and d is the particle diameter. Maximum clustering occurs for $St \sim 1$. In an attempt to maximize the signal-to-noise ratio in the experiment, we selected silver-coated hollow-glass spheres ($\beta = 1375$). The probability density function (PDF) of the particle size is shown in figure 1.3, both in terms of diameter and the corresponding Stokes number at the lowest and highest turbulence conditions in the study. Clearly, there is a broad range of particle Stokes numbers, peaked between 0.1–0.2 depending upon the fan speed. This range of Stokes numbers allows us to observe a good degree of particle clustering in the experiment.

Experiments were initiated by setting the fans to a particular condition and allowing the system to equilibrate. Particles were then injected into the top of the box, while simultaneously the digital camera recorded holograms at $\sim$ 10 Hz. Gravitational settling, as well as adhesion to box and fan surfaces, led to

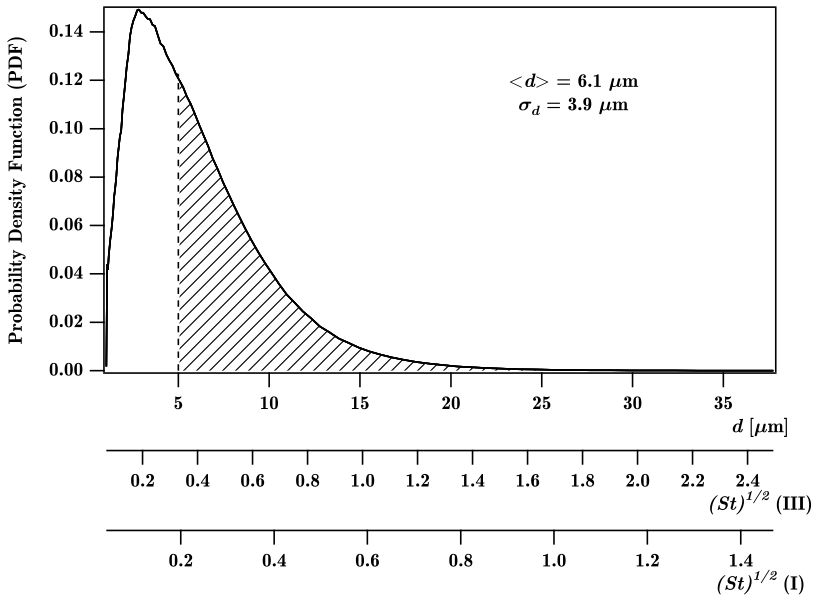

Figure 1.3: Particle size and particle Stokes PDFs for I and III. The particle size PDF was measured by a third party using the electrozone particle sensing technique. A sample filtering operation is shown for $d_c = 5\mu$m.

a decrease in the particle concentration over time; consequently, particles had to be re-injected periodically to sustain the concentration in the experimental volume within the desired range. The negligible particle mass loadings in the experiment ($O(10^{-4})$) led us to believe that the measured turbulence conditions were not substantially altered by particle injection, although we could not simultaneously measure particle and velocity field statistics.

1.2.2 Holographic Imaging

Digital holographic imaging, as in digital holographic PIV, employs a digital image sensor to record the hologram, and uses numerical algorithms to reconstruct the three-dimensional image volume (Owen et al. (2002), Pan & Meng (2003),

Xu et al. (2001)). It eliminates the notorious wet film processing of individual holograms and enables continuous-in-time, three-dimensional, volumetric particle/flow measurements. However, the low resolution of digital image sensors has restricted standard digital particle holography to the in-line configuration (forward scattering). The narrow angular spread of the in-line hologram recording, along with the finite digital sensor pixel size causes severe speckle noise and a large depth-of-focus in the reconstructed particle image. Consequently, the current generation of digital holographic imaging systems is limited to measurements at low particle densities (< 1 mm^{-3}) and small flow facilities (< 1 cm in each dimension).

The large size of our particle-laden turbulence chamber and the dense particle distribution prohibit the use of standard digital in-line holography due to its excessive speckle noise. We therefore employ a hybrid digital holographic system described in Meng et al. (2004) and Cao et al. (2007). In this approach (figure 1.1), the pulsed laser beam is split into a reference beam and a object illumination beam, allowing a selected volume of particles in the turbulence box to be imaged at 90°. The selected illumination and arrangement of 90° scattering avoids the excessive speckle noise from particles along the illumination path that are outside the volume of interest, as would occur in standard digital in-line holography. The 90° scattered light is then recorded via interference with the reference beam, which is folded into the hologram's optical axis. The recombination of the object and reference beams on-axis minimizes the spatial frequency of the holographic fringes, such that these can be resolved by the digital sensor. Such a design has the advantages of speckle-noise suppression provided by off-axis (side) scattering and the lower resolution requirement provided by on-axis (in-line) recording. Hence, the hybrid system enables 3D measurements in large

flow facilities with significant particle concentrations.

One challenge of the hybrid system is that side scattering does not allow the use of the complex amplitude method described in Pan & Meng (2003), designed to reduce the depth-of-focus and improve spatial resolution. Fortunately, images formed by 90° scattering inherently have up to an order of magnitude higher intensity-based axial definition than those formed by forward scattering; thus we employ an intensity based method to extract particle centroids from the reconstructed hologram, as described in Pan (2003). However, as intensity-based methods rely on thresholding of the reconstructed intensity field, smaller particles in a polydisperse distribution that have lower scattering intensity inevitably are lost during the thresholding, resulting in a particle size 'high-pass' filtering effect. Therefore, to achieve an accurate comparison between our experiments with a polydisperse distribution and DNS, this filtering effect must be taken into account.

Even with the hybrid scheme set for a relatively modest measurement volume of approximately 1 cm^3, the extracted particle density (~2 mm^{-3}) and number of particles extracted per hologram (~400) are both well below DNS values. To obtain acceptable statistical convergence, we must average over multiple holograms, weighted by the number of particles in each hologram.

1.3 Direct Numerical Simulations

The simulation domain consists of a three-dimensional cube of length 2π along each side (arbitrary units). Periodic boundary conditions make the flow-field amenable to Fourier spectral methods.

1.3.1 Governing Equations

The fluid is governed by the continuity and incompressible Navier-Stokes equations

$$\boldsymbol{\nabla} \cdot \boldsymbol{u} = 0 \,, \quad \frac{\partial \boldsymbol{u}}{\partial t} + \boldsymbol{u} \cdot \boldsymbol{\nabla} \boldsymbol{u} = -\frac{1}{\rho} \boldsymbol{\nabla} p + \nu \nabla^2 \boldsymbol{u} + \boldsymbol{F} \,, \tag{1.2}$$

where $\boldsymbol{u}(\boldsymbol{x}, t)$ is the fluid velocity, $p(\boldsymbol{x}, t)$ is pressure and $\boldsymbol{F}(\boldsymbol{x}, t)$ is a time-dependent, deterministic forcing function that injects energy into the first two wavenumbers to maintain statistically stationary, isotropic turbulence (Witkowska et al. (1997)). The influence of the particle volume on the continuity equation has been neglected due to the low particle volume loadings, $\Phi_v \sim O(10^{-7})$. Note the absence of a particle source term in the momentum equation. Reverse coupling is neglected, a simplification which is justified due to the neglibile mass loadings, $\Phi_m \sim O(10^{-4})$ (Boivin et al. (1998), Sundaram & Collins (1999)). Particles in the flow field are advanced according to the evolution equation derived by Maxey & Riley (1983), which for large particle-to-fluid density ratios (i.e., $\beta \gg 1$) simplifies to

$$\frac{d\boldsymbol{x}_p^{(i)}}{dt} = \boldsymbol{v}_p^{(i)} \,, \quad \frac{d\boldsymbol{v}_p^{(i)}}{dt} = \frac{\boldsymbol{u}\left[\boldsymbol{x}_p^{(i)}\right] - \boldsymbol{v}_p^{(i)}}{\tau_p^{(i)}} \,, \tag{1.3}$$

where $\boldsymbol{v}_p^{(i)}$ is the velocity of the i^{th} particle and $\boldsymbol{u}\left[\boldsymbol{x}_p^{(i)}\right]$ is the fluid velocity interpolated at the particle position $\boldsymbol{x}_p^{(i)}$. Additionally, we neglect gravitational settling. Wang & Maxey (1993) found no appreciable effect of gravitational settling on the particle concentration statistics for $v_g/u_\eta < 3$, where $v_g = \tau_p g$ is the gravitational settling velocity and $u_\eta = (\nu\epsilon)^{1/4}$ is the Kolmogorov velocity scale. In our simulations, $v_g/u_\eta \leq 1$ for all of the particles at all flow conditions. Moreover, 71%, 82% and 89% of the particles *after* filtering (see §1.3.3) have a settling velocity that is less than 10% of the Kolmogorov velocity scale in flow conditions I, II

and III respectively. Interparticle collisions are also neglected (Reade & Collins (2000a)).

1.3.2 Numerical Details

Equations (1.2) are solved on a 256^3 grid using a pseudospectral method. Details of the numerical method can be found in Brucker et al. (2007).

We initialize 600,128 particles with a Stokes (and response time) PDF that matches the experimental PDF shown in figure 1.3. Heun's method (two-stage, second-order Runge-Kutta) is used to numerically integrate (1.3) along each independent particle trajectory with use of an integrating factor. Fluid velocities at particle centers are obtained via an 8^{th} order Lagrangian interpolation scheme similar to the one described in Berrut & Trefethen (2004). Particle response times for the smallest particles are much smaller than the smallest fluid mechanical time scale, τ_η. Reducing the overall time step to accurately update these particles would be extremely wasteful of the CPU. Instead, the particle updates are 'sub-cycled,' wherein multiple particle time steps are taken per fluid time step, resulting in a more accurate description of the particle motions with only a modest increase in CPU.

1.3.3 Filtering

The finite resolution of the camera used to record the digital holograms restricts the range of particle sizes that can be accurately recorded. The camera pixel size is approximately 6.5 μm, hence one expects the camera will *filter* particles

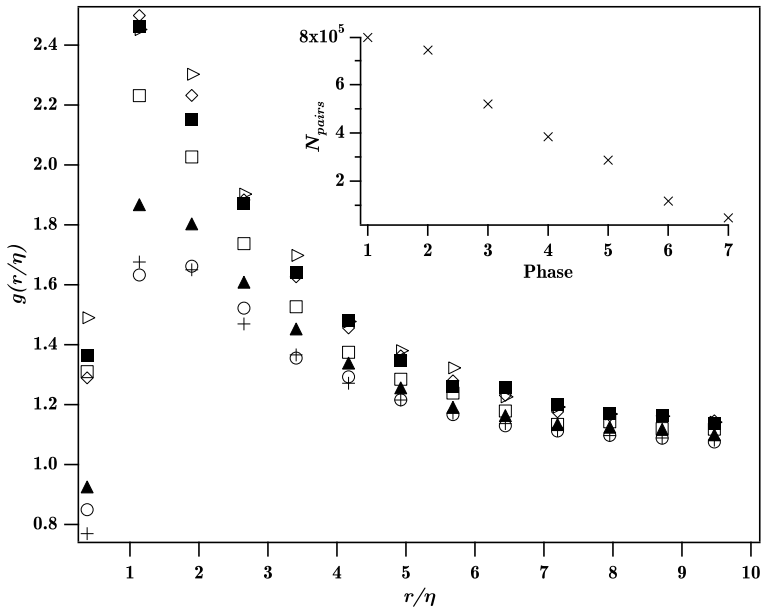

Figure 1.4: A time-series of RDFs (III) and number of particle pairs in each phase (inset):
+, Phase 1; ∘, Phase 2; ▲, Phase 3; □, Phase 4; ◊, Phase 5; ■, Phase 6; ▹, Phase 7.

of that size or smaller. Unfortunately, we have no *a priori* means of knowing which particles will be filtered. To mimic the finite resolution of the camera, we apply a high-pass particle size threshold filter with a variable diameter cutoff, d_c. Figure 1.3 shows the high-pass filter for a cutoff diameter, $d_c = 5\,\mu$m. Particles in the hatched region are used to compute the RDF. By varying the filter cut-off diameter over a reasonable range, $0\,\mu\text{m} \leq d_c \leq 10\,\mu\text{m}$, we observe the sensitivity of the RDF (see the inset in figure 1.5). Our approach is to fit d_c at one fan speed, and test the agreement between DNS and experiments at the other fan speeds, under the assumption that d_c is not sensitive to the conditions of the experiment.

1.4 Results and Discussion

At the conditions summarized in table 1.1, the RDF was computed by binning the particle pairs based on their separation distance, according to (1.1). The experimental volume is not periodic, thus making the analysis of particles near the boundaries ambiguous. To eliminate any bias from these particles, we treated the volume as periodic and paired those particles with reflected particles from elsewhere in the volume. Numerical experiments with DNS data (taken over non-periodic sub-domains) showed the error associated with this assumption to be small.

One unanticipated feature we observed is that following injection, the RDF evolves towards a stationary state. This can be seen in figure 1.4, which shows the RDF averaged over seven 'phases' following an injection. As shown in the inset of figure 3, the particle concentration is decreasing in time due to settling and losses to the fan and wall surfaces. When the particle number dropped below the detectable limit, we injected additional particles, causing the transient process to restart. Each 'phase' corresponds roughly to 1/2 second following the peak in the particle concentration of the injection cycle. The steady increase in the RDF over phases 1–5 is at least qualitatively similar to the build-up in the RDF observed in DNS at short times, starting from an initially random particle field. However, precise timings of the injection events were not made in this study, as we had not anticipated the transient behavior that was observed. Thus, the focus of this study will be on the stationary behavior we measured in the final two phases.

DNS at flow conditions that match the R_λ from each of the three experimental

conditions were performed. Particles with an identical Stokes number distribution for each experiment were introduced randomly, and the simulations were run for 10 τ_{eddy}, where $\tau_{\text{eddy}} \equiv L_{11}/u'$ is the large eddy turnover time, L_{11} is the longitudinal integral length scale and u' is the turbulence intensity. The DNS was continued for an additional 23 τ_{eddy} and the RDF was computed every 0.2 τ_{eddy} and averaged over the stationary period. The resulting statistical convergence of the RDF was substantially higher than in the experiments.

A complication in comparing the RDF from the experiments and DNS is that even for identically distributed particles, the RDF is sensitive to the size of the experimental volume. This can be understood by recognizing that the RDF (see 1.1) is normalized by the average pair density in the experimental volume V. Because of clustering, the average pair density for a small sample volume (such as that found in our experiments) will be larger than the corresponding value in the thermodynamic limit $V \to \infty$. To compensate, we renormalized the DNS RDF such that the average pair density used was based on the equivalent sample volume as in the experiment, measured in Kolmogorov units.

The RDFs for conditions I, II and III of table 1.1 are displayed in figure 1.5. As discussed in §1.3.3, the limited resolution of the camera filters the smaller particles. We compensate for the camera's filtering by introducing a high-pass particle size threshold filter with a cutoff d_c. As shown in the inset of figure 1.5, the RDF increases with increasing d_c. Because the particles removed by the filtering process have smaller Stokes numbers, their presence lowers the RDF, or conversely their removal increases it. The high-pass filter of $d_c = 8$ μm applied to DNS data shows the best agreement with the experiments at all three conditions. Note that we neglect the first experimental point that is low due to spatial

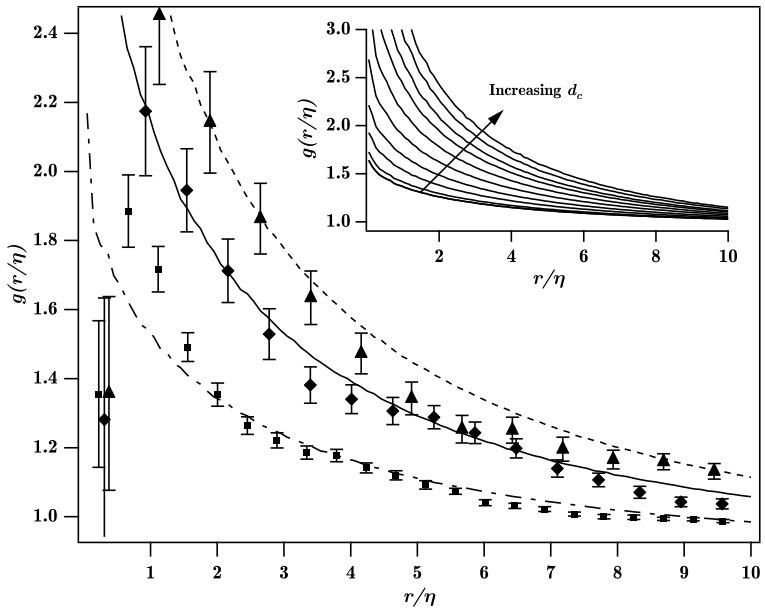

Figure 1.5: RDFs from experiment and DNS ($d_c = 8\,\mu$m). Error bars give the 95% confidence interval obtained via bootstrap: ——– – ——, I (DNS); ——, II (DNS); – – –, III (DNS); ■, I (Exp.); ⧫, II (Exp.) ; ▲, III (Exp.). Inset shows DNS RDFs (III) for $d_c = 0, 1, \cdots 10\,\mu$m. For $d_c = 8\,\mu$m: $\langle St \rangle = 0.21$ (I); $\langle St \rangle = 0.40$ (II); $\langle St \rangle = 0.60$ (III).

measurement errors (particularly in the axial direction) and statistical sampling errors. Aside from that point, the remainder of the experimental points are generally in quantitative agreement with the DNS. There are some discrepancies at $r/\eta \sim 5$, mainly due to a bump in the experimental points that we do not observe in the DNS, and for which we have no satisfactory explanation. A second discrepancy occurs at the lowest fan speed for $r/\eta \leq 2$. We could match these points by setting $d_c = 9$; however, we cannot justify this change.

An alternate measure of inertial particle clustering is the correlation dimension, D_2 (Grassberger & Procaccia (1983)). Bec et al. (2007) used this measure to quantify particle clustering. Table 1.2 shows the good agreement between D_2 obtained by nonlinear regression of the experimental measurements and D_2 from the DNS with filter $d_c = 8\,\mu$m. Chun et al. (2005) predicted the RDF for

Table 1.2: Correlation dimension, D_2, and the power-law exponent, c_1, from direct numerical simulations (DNS) and experiments (Exp) at the three conditions. Also shown is the expression $\tilde{c}_1 = d - D_2$ for $d = 3$.

	D_2		c_1		$\tilde{c}_1$	
	Exp	DNS	Exp	DNS	Exp	DNS
Case I	2.72	2.79	0.25	0.20	0.28	0.21
Case II	2.56	2.67	0.34	0.32	0.44	0.33
Case III	2.51	2.59	0.40	0.39	0.49	0.41

monodisperse particles should behave as a power law of the form $g(r) \sim (\eta/r)^{c_1}$. For a power-law RDF, the power c_1 is related to the correlation dimension as follows: $c_1 = d - D_2$, where $d = 3$ is the dimension of the space containing the particles. Table 1.2 shows a comparison of the values of c_1 obtained by regression of both data sets, and we see once again there is good agreement between experiment and simulations. The expected relationship between c_1 and D_2 ($\tilde{c}_1$ in Table 1.2) is better satisfied by the DNS than by the experimental data. This is mainly attributed to the lower statistical error in the DNS relative to the experiment.

The filtering operation we implemented in the DNS analysis is a crude approximation of the complex filtering performed by the camera. We anticipate the camera will give rise to a convolution of the size distribution rather than a strict high-pass filter. That is, the resolution of a particle of a given size will depend upon the number and size of the neighboring particles that surround it. We have explored this more complex filtering process by generating synthetic digital holograms using DNS particle positions. We ultimately selected the high-pass filter for its simplicity. We could not justify introducing a more complex function at this time, particularly given the other uncertainties in the experiment, and the difficulty of precisely matching the experiment in the DNS.

Our results support our contention that the high-pass filter is able to capture the primary effect of the filtering by the CCD camera.

1.5 Conclusions

Three-dimensional measurements of the positions of a polydisperse distribution of inertial particles in homogenous and isotropic box turbulence were performed using digital holography. Radial distribution functions were calculated from measurements at three flow conditions. For the first time, quantitative comparisons of the experimentally obtained RDF were made with results from direct numerical simulations performed on a 256^3 grid with 600,128 particles. Near perfect parameter overlap was achieved in terms of the particle Stokes number PDF and flow Reynolds number. A simple high-pass particle size threshold filter was introduced in the numerical results to mimic the resolution limitations of the CCD camera. We find very good agreement between experiment and DNS based on a filter cutoff $d_c = 8\ \mu$m. This value is reasonable, given the camera pixel size is $6.7\ \mu$m.

In future experiments, we plan to address the filtering problem by using a narrower particle size distribution. In addition, work is underway to extend the analysis of Pan & Meng (2003) to the hybrid scheme. This will allow us to more accurately distinguish particles from noise, and will improve the accuracy of the measurement in the axial direction (de Jong & Meng (2007)). Finally, by implementing a more precise injection scheme, we will be able to investigate the time dependence of the RDF and compare its transient behavior to the DNS.

This work was supported by the NASA Microgravity Fluid Physics Program

grants NNCO5GA45G and NNCO5GA37G, and by the National Science Foundation through grants CTS-0112514 and PHY-0554675. JPLCS acknowledges support from the Brazilian Ministry of Education through the CAPES agency.

REFERENCES

Aliseda A, Cartellier A, Hainaux F, Lasheras JC. 2002. Effect of preferential concentration on the settling velocity of heavy particles in homogeneous isotropic turbulence. *J. Fluid Mech.* 468:77–105

Bec J, Biferale L, Cencini M, Lanotte A, Musacchio S, Toschi F. 2007. Heavy particle concentration in turbulence at dissipative and inertial scales. *Phys. Rev. Lett.* 98:084502

Benedict LH, Gould RD. 1996. Towards better uncertainty estimates for turbulence statistics. *Exp. Fluids* 22:129–136

Berrut JP, Trefethen LN. 2004. Barycentric Lagrange interpolation. *Siam Rev.* 46:501–517

Birouk M, Chauveau C, Sarh B, Quilgars A, Gökalp I. 1996. Turbulence effects on the vaporization of monocomponent single droplets. *Combust. Sci. Tech.* 113–114:413–428

Boivin M, Simonin O, Squires KD. 1998. Direct numerical simulation of turbulence modulation by particles in isotropic turbulence. *J. Fluid Mech.* 375:235–263

Brucker KA, Isaza JC, Vaithianathan T, Collins LR. 2007. Efficient algorithm for simulating homogeneous turbulent shear flow without remeshing. *J. Comp. Phys.* 225:20–32

Cao L, Pan G, Woodward S, Meng H. 2007. Hybrid digital holographic imaging system for 3D dense particle field measurement. In *7th International Symposium on Particle Image Velocimetry*. PIV2007

Chun J, Koch DL, Rani S, Ahluwalia A, Collins LR. 2005. Clustering of aerosol particles in isotropic turbulence. *J. Fluid Mech.* 536:219–251

Collins LR, Keswani A. 2004. Reynolds number scaling of particle clustering in turbulent aerosols. *New Journal of Physics* 6:119

de Jong J, Cao L, Woodward S, Salazar JPLC, Collins LR, Meng H. 2007. Dissipation measurement in zero-mean-flow isotropic turbulence. *Exp. Fluids* In review

de Jong J, Meng H. 2007. Digital holographic particle validation via complex wave. *Appl. Optics* 46:7652–7661

Eaton JK, Fessler JR. 1994. Preferential concentration of particles by turbulence. *Int. J. Multiphase Flow* 20:169–209

Falkovich G, Fouxon A, Stepanov MG. 2002. Acceleration of rain initiation by cloud turbulence. *Nature* 419:151–154

Grassberger P, Procaccia I. 1983. Characterizations of strange attractors. *Phys. Rev. Lett.* 50:346–349

Holtzer GL, Collins LR. 2002. Relationship between the intrinsic radial distribution function for an isotropic field of particles and lower-dimensional measurements. *J. Fluid Mech.* 459:93–102

Kline SJ, McClintock FA. 1953. Describing uncertainties in single-sample experiments. *Mechanical Engineering* 75:3–8

Maxey MR. 1987. The gravitational settling of aerosol particles in homogeneous turbulence and random flow fields. *J. Fluid Mech.* 174:441–465

Maxey MR, Riley JJ. 1983. Equation of motion for a small rigid sphere in a nonuniform flow. *Phys. Fluids* 26:883–889

McQuarrie DA. 1976. *Statistical Mechanics*. New York: Harper & Row

Meng H, Pan G, Pu Y. 2004. Holographic particle image velocimetry: from film to digital recording. *Measurement Sci. and Tech.* 15:673–685

Owen R, Zozylya A, Benoit M, Klaus D. 2002. Microgravity materials and life sciences research applications of digital holography. *Appl. Optics* 41:3927–3935

Pan G. 2003. *Digital holographic imaging for 3D particle and flow measurement*. Ph.D. thesis, State University of New York at Buffalo

Pan G, Meng H. 2003. Digital holography of particle fields: reconstruction by use of complex amplitude. *Applied Optics* 42:827–833

Reade WC, Collins LR. 2000a. Effect of preferential concentration on turbulent collision rates. *Phys. Fluids* 12:2530–2540

Reade WC, Collins LR. 2000b. A numerical study of the particle size distribution of an aerosol undergoing turbulent coagulation. *J. Fluid Mech.* 415:45–64

Saw EW, Shaw RA, Ayyalasomayajula S, Chuang PY, Gylfason A. 2007. Inertial clustering of particles in high-Reynolds-number turbulence. *Phys. Rev. Lett.* In review

Shaw RA. 2003. Particle-turbulence interactions in atmospheric clouds. *Annu. Rev. Fluid Mech.* 35:183–227

Shaw RA, Reade WC, Collins LR, Verlinde J. 1998. Preferential concentration of cloud droplets by turbulence: effects on the early evolution of cumulus cloud droplet spectra. *J. Atmos. Sci.* 55:1965–1976

Squires KD, Eaton JK. 1991. Preferential concentration of particles by turbulence. *Phys. Fluids A* 3:1169–1178

Sreenivasan KR. 1995. On the universality of the Kolmogorov constant. *Phys. Fluids* 7:2778–2784

Sundaram S, Collins LR. 1997. Collision statistics in an isotropic, particle-laden turbulent suspension i. direct numerical simulations. *J. Fluid Mech.* 335:75–109

Sundaram S, Collins LR. 1999. A numerical study of the modulation of isotropic turbulence by suspended particles. *J. Fluid Mech.* 379:105–143

Wang LP, Maxey MR. 1993. Settling velocity and concentration distribution of heavy particles in homogeneous isotropic turbulence. *J. Fluid Mech.* 256:27

Wang LP, Wexler AS, Zhou Y. 2000. Statistical mechanical description and modeling of turbulent collision of inertial particles. *J. Fluid Mech.* 415:117–153

Witkowska A, Brasseur JG, Juvé D. 1997. Numerical study of noise from isotropic turbulence. *J. Comput. Acoust.* 5:317–336

Wood AM, Hwang W, Eaton JK. 2005. Preferential concentration of particles in homogeneous and isotropic turbulence. *Int. J. Multiphase Flow* 31:1220–1230

Xu L, Jericho M, Meinertzhagen I, Kreuzer H. 2001. Digital in-line holography for biological applications. *Proc. Nat. Acad. Sci.* 98:11301–11305

Zaichik LI, Alipchenkov VM. 2003. Pair dispersion and preferential concentration of particles in isotropic turbulence. *Phys. Fluids* 15:1776–1787

CHAPTER 2

INERTIAL PARTICLE RELATIVE VELOCITY STATISTICS IN HOMOGENEOUS ISOTROPIC TURBULENCE*

In the present study we investigate the scaling of relative velocity structure functions for inertial particles of order two and higher, both in the dissipation range and the inertial subrange using direct numerical simulations (DNS). Within the inertial subrange our findings show that contrary to the well-known attenuation in the tails of the one-point probability density function with increasing inertia (Bec et al. 2006), the exact opposite occurs with the velocity structure function at sufficiently large Stokes numbers. We observe reduced scaling exponents for the structure function when compared to that of the fluid, similar to what occurs with a passive scalar. DNS allows us to isolate effects due to biased sampling of the velocity field by inertial particles, a result of preferential concentration, and those that originate from filtering, i.e., the tendency of inertial particles to attenuate the velocity fluctuations in the fluid. By isolating these effects, we verify that it is filtering that accounts for most of the scaling behaviour in the inertial subrange. In the dissipation range we see evidence of so-called 'crossing trajectories,' the 'sling effect' or 'caustics,' and find good agreement with the theory put forth by Wilkinson et al. (2006) and Falkovich & Pumir (2007) for Stokes numbers greater than 0.5. We also look at the scaling exponents within the context of the model proposed by Bec et al. (2010). Another interesting finding is that inertial particles at low Stokes numbers sample regions of higher kinetic energy than the fluid particle field, the converse occurring at high Stokes numbers. The trend at low Stokes numbers is predicted by the theory of Chun et al. (2005). This work is relevant to modeling the particle

*To be submitted to the *Journal of Fluid Mechanics.*

collision rate (Sundaram & Collins 1997), and highlights the interesting array of phenomena induced by inertia.

2.1 Introduction

Turbulent flows laden with inertial particles, i.e., particles with density larger than the carrier fluid, are relevant to natural phenomena such as cloud formation (Shaw 2003, Warhaft 2009a), plankton distribution (Malkiel et al. 2006) and planetesimal formation (Johansen et al. 2007) in addition to engineering processes such as aerosol drug delivery (Li et al. 1996), powder manufacturing (Moody & Collins 2003) and spray combustion (Faeth 1996). Over the past few decades, numerical solutions of the full Navier-Stokes equations, known as direct numerical simulations (DNS), have been feasible and only very recently have the Reynolds numbers of these simulations approached the range of values found in laboratory experiments (Ishihara et al. 2009). Even then, both experiments and DNS lag far behind Reynolds numbers observed in atmospheric phenomena (Warhaft 2009b). Nonetheless, even at low to moderate Reynolds numbers, many of the underlying physical mechanisms can be studied, providing insight into complex phenomena such as the formation of clouds (Siebert et al. 2010b).

The collision kernel presented in Sundaram & Collins (1997), which gives the rate of two-particle collisions per unit volume of the fluid, requires knowledge of two inertial particle pair statistics: (i) the radial distribution function at contact; and (ii) the mean inward relative velocity along the line of centers of the two particles. The radial distribution function (McQuarrie 1976) corrects

the collision kernel for the non-uniformity in the spatial distribution of particles that results from the spontaneous clustering or preferential concentration that occurs with inertial particles (Balachandar & Eaton 2010). The inward relative velocity then controls the rate at which the particles encounter each other. DNS studies of inertial particles to date have mainly focused on quantifying the clustering phenomenon (Bec et al. 2007, Chen et al. 2006, Chun et al. 2005, Coleman & Vassilicos 2009, Collins & Keswani 2004, Goto & Vassilicos 2008, Maxey 1987, Reade & Collins 2000a, Shaw et al. 1998, Squires & Eaton 1991, Sundaram & Collins 1997, Wang & Maxey 1993). This important body of work, along with the related experimental investigations (de Jong et al. 2010, Eaton & Fessler 1994, Salazar et al. 2008, Saw et al. 2008, Wood et al. 2005) has led to a greater understanding of the underlying mechanisms of clustering, which has enabled development of useful models and parameterizations (Ayala et al. 2008, Chun et al. 2005, Coleman & Vassilicos 2009, Goto & Vassilicos 2008, Wang et al. 2000, Zaichik & Alipchenkov 2003, 2009, Zhou et al. 2001). However, as noted by Sundaram & Collins (1997), inertia also influences the relative velocity statistic in complex and profound ways. The classical works of Saffman & Turner (1956) and Abrahamson (1975) give analytical results for the limits of zero and infinite inertia respectively, and there exist parameterizations for intermediate values of the Stokes number (Ayala et al. 2008), nevertheless there remain fundamental questions concerning the role of Reynolds number in these relationships, how gravitational settling couples with turbulence, and what effect differences in the particle sizes have on the mean relative velocity statistic. In principle, full knowledge of the collision kernel will allow the prediction of the evolution of the size distribution of a droplet population (Reade & Collins 2000b) in applications as complicated as an atmospheric cloud. In particular,

the role of turbulence in clouds remains controversial, with some advocating for its significance (Falkovich et al. 2002, Shaw et al. 1998, Siebert et al. 2010a, Wilkinson et al. 2006), while others have questioned its importance (Chaumat & Brenguier 2001, Grabowski & Vaillancourt 1999, Vaillancourt et al. 2001), in part because of this lack of a complete understanding of the phenomenon.

In the present study we investigate the scaling of relative velocity structure functions of order two and higher for inertial particles in both the dissipation range and the inertial subrange. The relative velocity structure function of order p is herein given by

$$G_p^{\parallel,\perp}(r, St) \equiv \left\langle \left[\Delta\mathbf{v} \cdot \mathbf{e}^{\parallel,\perp} \right]^p \right\rangle (r) \,, \tag{2.1}$$

where $\langle\cdot\rangle$ indicates the ensemble average, $\parallel$ and $\perp$ represent the directions parallel (longitudinal) and perpendicular (transverse) to the separation vector $\mathbf{r}$, respectively, $\mathbf{e}$ is the unit vector in the direction given by the superscript, $\Delta\mathbf{v}(r, St) \equiv \mathbf{v}(\mathbf{x} + \mathbf{r}, St) - \mathbf{v}(\mathbf{x}, St)$, $\mathbf{v}(\mathbf{x}, St)$ is the particle velocity at position $\mathbf{x}$, $St \equiv \tau_p/\tau_\eta$ is the particle Stokes number, which is a non-dimensional measure of its inertia, $\tau_p = \rho_p d^2/(18\rho\nu)$ is the particle relaxation time and $\tau_\eta \equiv \sqrt{\nu/\langle\varepsilon\rangle}$ is the Kolmogorov time scale, characteristic of the turbulence small scales. In the above expressions, d is the particle diameter, ρ_p is the particle density, ρ is the fluid density, ν is the fluid kinematic viscosity and ε is the instantaneous, local turbulent kinetic energy dissipation rate. Note that $\mathbf{v}(\mathbf{x}, St = 0) = \mathbf{u}(\mathbf{x})$, where $\mathbf{u}(\mathbf{x})$ is the fluid velocity at position $\mathbf{x}$.

Recent work (Falkovich et al. 2002, Falkovich & Pumir 2007, Wilkinson et al. 2006) has drawn attention to the role played by caustics, also referred to as crossing trajectories (Yudine 1959) or the sling effect, whereby the inertial particle velocity field need not be single-valued at a given point. This results when par-

ticles are flung from different regions of the flow towards the same point. These studies suggest that caustics can increase the collision rate significantly.

In this work we seek evidence of caustics and their effects on two-point statistics relevant to the interparticle collision rate and dispersion. DNS allows us to isolate effects due to biased sampling of the velocity field by inertial particles and those that originate from filtering, i.e., the tendency of inertial particles to filter higher frequency modes of the velocity field with increasing inertia, or in other words, the tendency of becoming more sluggish. All statistics computed are compared to those of fluid particles.

Our findings show that contrary to the well-known attenuation in the PDF tails of one-point statistics with increasing inertia (Ayyalasomayajula et al. 2006, Bec et al. 2006), the exact opposite occurs with two-point statistics at sufficiently large Stokes number. This in turn leads to reduced scaling exponents of the structure function when compared to that of the fluid, similar to what occurs with a passive scalar. However, we believe the origin of this apparent increased intermittency lies in the caustics. Although caustics apply in the strict sense to a zero separation distance, we extend the notion to the inertial subrange, interpreting caustics as leading to an increased decorrelation with respect to collocated fluid particles. We also find that low St particles tend to sample regions of the flow with higher kinetic energy. This biased sampling reaches a maximum at $St \approx 0.2$.

Table 2.1: Table of DNS flow statistics. The turbulent kinetic energy is given by $\int_0^{\kappa_{\max}} E(\kappa)d\kappa$, where $E(\kappa)$ is the energy spectrum function and $\kappa_{\max}$ is the largest resolved wavenumber. The longitudinal integral length scale is given by $L = \pi/(2u'^2)\int_0^{\kappa_{\max}} [E(\kappa)/\kappa]\, d\kappa$.

	units	I	II
Reynolds number $R_\lambda = u'^2\sqrt{15/(\nu\langle\varepsilon\rangle)}$	—	60	120
Turbulent kinetic energy k	$\left[\mathrm{L^2T^{-2}}\right]$	1.43	1.43
Turbulent intensity $u' = \sqrt{2/3k}$	$\left[\mathrm{LT^{-1}}\right]$	0.98	0.98
Turbulent energy dissipation rate ϵ	$\left[\mathrm{L^2T^{-3}}\right]$	0.33	0.32
Longitudinal integral scale L	[L]	1.60	1.44
Integral time scale $T = L/u'$	[T]	1.64	1.48
Kolmogorov length scale η	[L]	0.046	0.017
Kolmogorov time scale τ_η	[T]	0.184	0.097
Kolmogorov velocity scale u_η	$\left[\mathrm{LT^{-1}}\right]$	0.248	0.175
Small scale resolution $\kappa_{\max}\eta$	–	5.4	2.0
Normalized simulation time T_{end}/T	–	19.8	22.0
Number of grid points N^3	–	256^3	256^3
Number of particles at each St	–	32,768	32,768

2.2 Numerical methods

We consider the case of small ($d \ll \eta$) and heavy ($\rho_p/\rho \gg 1$) particles, where $\eta \equiv \left[\nu^3/\langle\varepsilon\rangle\right]^{1/4}$ is the Kolmogorov length scale. Basset forces are neglected, as well as lubrication effects and added mass. Gravitational forces are also neglected. In the limit of low volume Φ_v and mass fractions Φ_m we may neglect effects on the continuity equation and reverse-coupling (Boivin et al. 1998, Sundaram & Collins 1999). In addition, interparticle collisions are not considered. The resulting governing equations for the inertial particles are (Maxey & Riley 1983)

$$\frac{d\mathbf{X}}{dt} = \mathbf{v}\,, \tag{2.2}$$

$$\frac{d\mathbf{v}}{dt} = \dot{\mathbf{v}} = \frac{\mathbf{u}-\mathbf{v}}{\tau_p}\,, \tag{2.3}$$

where $\mathbf{X}$, $\mathbf{v}$ and $\dot{\mathbf{v}}$ are the particle position, velocity and acceleration, respectively. The fluid particles are advanced by solving the Navier-Stokes equations

in spectral space and performing an inverse FFT to obtain the velocity values on a regularly spaced grid. The fluid velocities are then interpolated to the particle positions via an 8^{th} order Lagrangian interpolation scheme (Berrut & Trefethen 2004). The position of fluid particles is advanced according to

$$\frac{d\mathbf{X}}{dt} = \mathbf{u} \, . \tag{2.4}$$

The effect of biased sampling of the flow field by particles due to their inertia can be isolated (i.e., without filtering) by computing fluid particle statistics along inertial particle trajectories. Likewise, the effect of filtering can be isolated (i.e., without biased sampling) by computing the inertial particle 'velocity' via (2.3) along fluid particle trajectories based on (2.4). The combination of mixed simulations enables us to disentangle filtering effects from biased sampling effects that both influence inertial particle statistics.

The fluid velocity field $\mathbf{u}(\mathbf{x})$ is computed via a parallel pseudo-spectral code, details of which can be found in Brucker et al. (2007). We use a deterministic forcing scheme to ensure statistical stationarity, whereby the amount of energy dissipated by viscous forces is injected in the two lowest wavenumbers, maintaining the total kinetic energy constant. The inertial particles are advanced by Heuns' method with use of an integrating factor. Since the particle relaxation times at low St are generally much smaller than the fluid time-step Δt_f, we take multiple particle time-steps per fluid time-step, where fluid velocities are interpolated linearly in time. For all St we ensure $\Delta t_p/\tau_p \leq 0.1$, where Δt_p is the particle time-step. The combination of Heuns' method with the linear interpolation in time is second-order accurate. Table 1 contains a summary of relevant DNS parameters for the two cases studied.

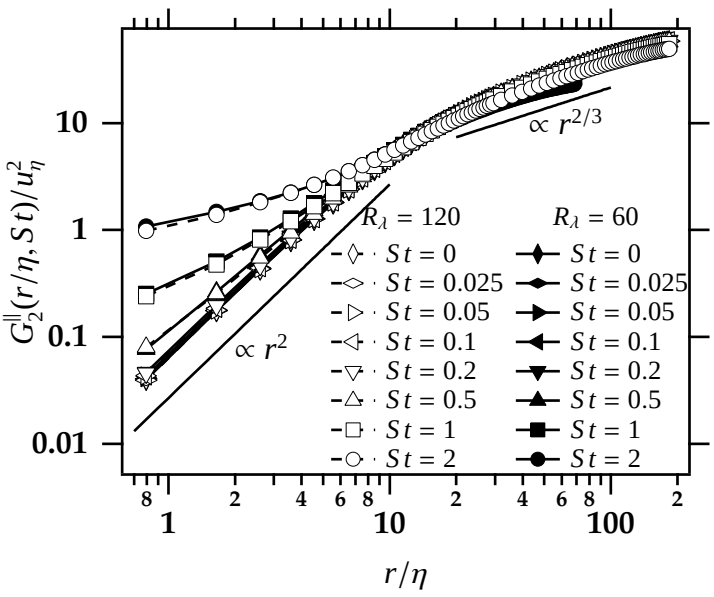

Figure 2.1: Second-order longitudinal structure function normalized by the square of the Kolmogorov velocity. Straight lines show the expected scaling for the dissipation range (r^2) and inertial subrange ($r^{2/3}$).

2.3 Results and Discussion

Kolmogorov (1941) presented three hypotheses that constitute what is now widely known as K41 theory. The hypothesis of local isotropy states that at sufficiently large Reynolds number R_λ and far from boundaries, the small scale turbulence is isotropic. Kolmogorov's first similarity hypothesis states that at sufficiently large R_λ and in the absence of boundary effects, there is a range of scales $l \ll l_{EI}$ such that statistics are solely determined by the viscosity ν and the transfer of energy from the large to the small scales in the form of the turbulence kinetic energy dissipation rate ε, where l_{EI} is the scale of the energy containing eddies. This defines the universal equilibrium range. The second similarity hypothesis states that under the same conditions there is a range of scales $\eta \ll l \ll l_{EI}$, such that statistics are determined by ε, independent of ν. This

defines the inertial subrange. The dissipation range is the range of scales $l \ll \eta$. Application of this theory to the second order structure function $G_2^{\parallel}(r, St = 0)$ (fluid particles) yields

$$G_2^{\parallel}(r, St = 0) = \begin{cases} C_2 \left[\langle\varepsilon\rangle r\right]^{2/3} & \text{for } \eta \ll r \ll l_{EI} \,, \\ \frac{\langle\varepsilon\rangle}{15\nu} r^2 & \text{for } r \ll \eta \,, \end{cases} \tag{2.5}$$

where $C_2 \approx 2.1$ (Sreenivasan 1995) is an empirical constant (called the 'Kolmogorov constant') not determined by the theory. Figure 2.1 shows $G_2^{\parallel}(r, St = 0)$ as a function of r in logarithmic coordinates. The scaling ranges for the fluid particles are easily identified; straight lines with slopes of 2 and 2/3 are shown for clarity. We also include curves for the finite Stokes particles. It is evident there is a systematic shift of these curves with increasing Stokes number, particularly in the dissipation range (although systematic deviations exist in both ranges, as will be shown). The next sections discuss the scaling in the dissipation range and inertial subrange in more detail.

2.3.1 The dissipation range

The second-order structure function shown in figure 2.1 displays the expected r^2 scaling for fluid particles ($St = 0$) in the dissipation range. However, with increasing Stokes number there is a systematic departure from the fluid particle curve, which becomes pronounced for $St > 0.2$. Bec et al. (2010) proposed a scaling of the form

$$G_p^{\parallel}(r, St) \propto r^{\xi_p(St)} \,, \tag{2.6}$$

where $0 \leq \xi_p(St) \leq p$. This assumption is consistent with the limits $\xi_p(St \to 0) = p$ (fluid limit) and $\xi_p(St \to \infty) = 0$ (ballistic limit), and is plausible at

intermediate values of the Stokes number, where Bec et al. (2010) empirically found the following functional form fit the data well

$$\xi_p(St) = \begin{cases} p & \text{for } p \leq \alpha \ln(7/St)\,, \\ \alpha \ln(7/St) & \text{for } St \leq 7\,, \\ 0 & \text{for } St > 7\,. \end{cases} \tag{2.7}$$

From figure 4 in their paper we estimate the coefficient $\alpha = 0.36$, independent of the Reynolds number. One can attribute this variation in the power to the existence of 'caustics' or folds in the velocity distribution of inertial particles at a given point, of continuously varying strength. When caustics appear, inertial particle velocities at a point in the fluid are not perfectly correlated. Wilkinson et al. (2006) and Falkovich et al. (2002) analyzed velocity difference statistics of two inertial particles at zero separation distance embedded in a white noise fluid velocity and derived an Arrhenius-like expression of the form

$$\langle |\Delta \mathbf{v}|^p \rangle (r \to 0, St) = B^p \exp\left[-pA/St\right]\,, \tag{2.8}$$

where $\Delta\mathbf{v}$ implies sampling two different inertial particles at a given point, and the coefficients A and B are independent of the Stokes number, but are implicit functions of the Reynolds number. Note that (2.8) implies a continuous variation of caustics with Stokes number. Moreover, this relationship is compatible with (2.6) proposed by Bec et al. (2010) only if $\xi_p = 0$, which in their analysis occurs for $St \gtrsim 7$.

To assist us in understanding the limit $r \to 0$, it is useful to introduce the following decomposition of the particle velocity, found by rearranging (2.3)

$$\mathbf{v} = \mathbf{u} - \tau_p \dot{\mathbf{v}}\,. \tag{2.9}$$

Substituting this into (2.1), the second order structure function can be expanded as follows

$$G_2^{\parallel}(r,St) = \underbrace{\left\langle \left[\Delta\mathbf{u}\cdot\mathbf{e}^{\parallel}\right]^2 \right\rangle(r)}_{G_2^{\parallel}(r,St=0)} - 2\underbrace{\tau_p \left\langle \left[\Delta\mathbf{u}\cdot\mathbf{e}^{\parallel}\right]\left[\Delta\dot{\mathbf{v}}\cdot\mathbf{e}^{\parallel}\right] \right\rangle(r)}_{\equiv G_{u\dot{v}}^{\parallel}(r,St)} + \underbrace{\tau_p^2 \left\langle \left[\Delta\dot{\mathbf{v}}\cdot\mathbf{e}^{\parallel}\right]^2 \right\rangle(r)}_{\equiv G_{\dot{v}^2}^{\parallel}(r,St)} . \quad (2.10)$$

The existence of caustics implies $\lim_{r\to 0} G_2^{\parallel}(r,St) \neq 0$. If we consider the limiting behaviour of the terms on the right hand side of (2.10), the first two terms will vanish in the limit $r \to 0$ due to the smooth variation of the fluid velocity difference $\Delta\mathbf{u}$, and hence only the third term is capable of producing a nonzero (caustic) result. Hence, we coin this term the caustic structure function. If the power law in (2.6) suggested by Bec et al. (2010) is valid, with $\xi_p(St) < p$ when caustics are present, then we expect under that circumstance the third term to be dominant for $r/\eta \ll 1$.

Another question to consider is whether caustics exist at all finite values of the Stokes number. This is certainly implied by (2.8) whereas (2.6) implies they exist only for $St > 7$. One way to approach this question is to consider the limit $St \ll 1$. Following Maxey (1987), we have $\dot{\mathbf{v}} = \mathbf{a}$ to leading order, where $\mathbf{a}$ is the fluid acceleration at the particle position. This implies the inertial particle velocity is an *analytic* function of the fluid velocity (Shotorban & Balachandar 2006, 2009), which is inconsistent with the formation of caustics. This suggests that the Stokes number must exceed a critical value, say St_c, for caustics to form. Below this value, we expect a smooth variation of all three correlations on the RHS of (2.10), or equivalently by a Taylor series expansion $G_2^{\parallel}(r, St < St_c) \propto r^2$.

Superimposing all of these considerations, we arrive at the following general expression for the second-order longitudinal structure function in the dissipa-

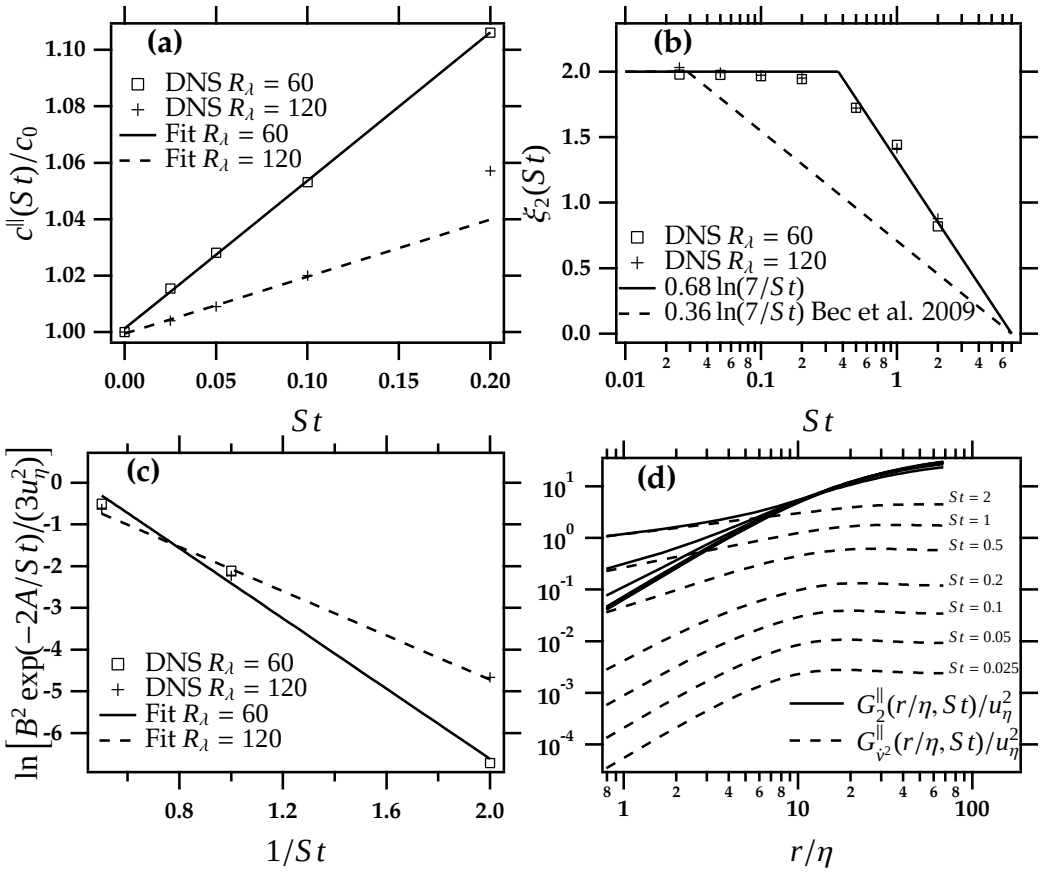

Figure 2.2: Results from the multi-variable least squares regression of the DNS data to (2.11). (a) $c^{\parallel}(St)$ normalized by c_0 for the two Reynolds numbers—solid and dashed curves are linear fits to the small Stokes data based on (2.13); (b) power ξ_2 vs Stokes number, solid lines are the regressed coefficients we obtain (see table 2.2) and dashed line is from the fit by Bec et al. (2010); (c) Arrhenius plot of b in (2.12) for $St > St_c$ to obtain coefficients A and B; and (d) plot of $G^{\parallel}_{\dot{\nu}^2}(r, St)$ on the RHS of the decomposition given in (2.10) vs r/η demonstrating the dominance of this term at small separations and higher Stokes numbers.

tion range of turbulence

$$G_2^{\parallel}(r,St) = \begin{cases} c^{\parallel}(St)r^2 & \text{for } St < St_c\,, \\ \frac{1}{3}B^2\exp\left[-2A/St\right] + c^{\parallel}(St)r^{\xi_2(St)} & \text{for } St_c \le St \le 7\,, \\ \frac{1}{3}B^2\exp\left[-2A/St\right] & \text{for } St > 7\,, \end{cases} \tag{2.11}$$

where $c^{\parallel}(St)$, $\xi_2(St)$, A and B are unknowns that will be determined from a regression analysis of the DNS. We begin that analysis by fitting the structure function for each Stokes number using a nonlinear regression to an expression of the form

$$G_2^{\parallel}(r,St) = ar^d + b\,, \tag{2.12}$$

where a, b and d are the fitting parameters. We then analyze the Stokes number dependence of these parameters in the context of the form proposed in (2.11), which allows us to identify St_c. For example, the coefficients A and B in (2.11) are obtained from a fit of the Stokes number dependence of b to the functional form $1/3B^2\exp\left[-2A/St\right]$ in the range $St \ge St_c$. Likewise we consider the Stokes number dependence of the power d (equivalent to ξ_2). Within the range $St < St_c$, we expect $c^{\parallel}(St)$ to be smooth in the limit $St \to 0$, allowing us to perform a perturbation expansion in St

$$\lim_{St\to 0} c^{\parallel}(St) = c_0 + Stc_1^{\parallel} + \cdots\,, \tag{2.13}$$

where $c_0 = \langle\varepsilon\rangle/(15\nu)$ is the coefficient for a fluid particle. We determine $c_1^{\parallel}$ in this range from a least-squares fit of a as a function of St, where the coefficients a are themselves obtained from a least-squares fit by setting $d = 2$ and $b = 0$ in (2.12). The maximum Stokes number we have simulated is $St = 2$, hence we will not consider the third branch of (2.11), which we include mainly for completeness and consistency with the expression of Bec et al. (2010).

Table 2.2: Table of coefficients for 2.11 and 2.13 obtained from the multiple regression analysis of the DNS data.

	$R_\lambda = 60$	$R_\lambda = 120$
$c_1^{\parallel}/c_0$	0.53	0.20
A	2.11	1.33
B/u_η	4.26	2.32
$\zeta_2(St < St_c)$	2	
$\zeta_2(St \geq St_c)$	$0.68\ln(7/St)$	

The main results from the two-step regression analysis are shown in figure 2.2 and the resulting coefficients are summarized in table 2.2. In general the quality of the regression of the data to (2.11) is quite good. For example, the linear regime for $c^{\parallel}$ is apparent in figure 2.2(a). Notice the slope is a sensitive function of Reynolds number at least over the range in this study. It is very difficult to discern from the DNS whether or not there exists a critical Stokes number for caustics. For a finite sample of inertial particles, the probability of two particles coexisting at precisely the same point vanishes, and so we must gather statistics of particles in a small neighborhood around a test particle. The challenge is to numerically distinguish the caustic (nonzero intercept) from the variation due to the small, but always finite separation distance. However, some support for the existence of St_c is found in figure 2.2(b), which shows the power ξ_2 as a function of the Stokes number. Notice the regressed power is nearly identically 2 until the $St = 0.5$ case, at which point it decreases with a functional behavior similar to the one proposed by Bec et al. (2010), but with a modified coefficient for our data of $\alpha = 0.68$. The sudden change in the slope between $St = 0.2$ and 0.5 supports the existence of a critical Stokes number in this range. It does not appear to be sensitive to the Reynolds number. If we define the critical Stokes number by the intersection of the two lines in figure 2.2(b) we have $2 = \alpha \ln(7/St_c)$, which we can solve for the critical Stokes number $St_c = 7\exp(-2/\alpha) = 0.37$. It is inter-

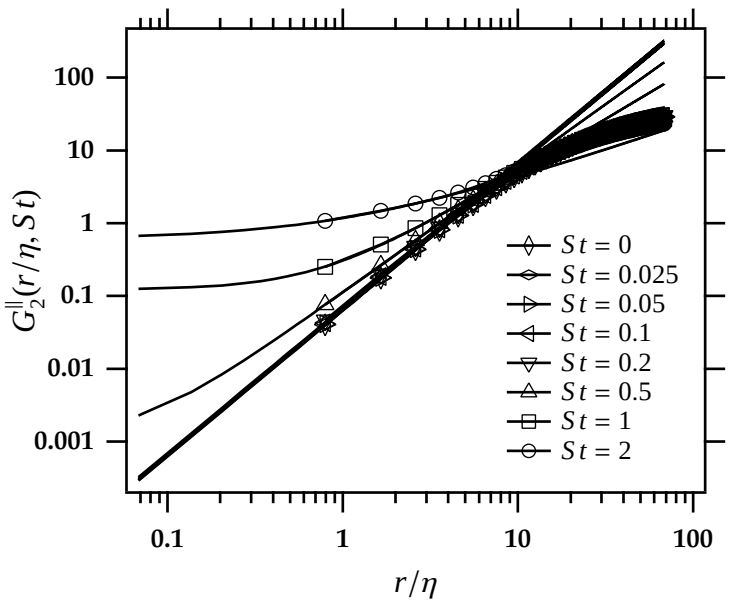

Figure 2.3: Comparison of the second-order structure function $G_2^{\parallel}(r/\eta, St)$ based on (2.11) and using the fitted coefficients given in table 2.2 (solid lines) with the DNS (symbols).

esting that the critical Stokes number is less than unity, implying even modest inertia will give rise to caustics. In the Arrhenius plot shown in figure 2.2(c), we have only considered the higher Stokes number values (i.e., $St \geq 0.5$) because the intercepts for the lower values were noisy. We see a reasonable fit to the Wilkinson et al. (2006) and Falkovich & Pumir (2007) relationship, with coefficients that are sensitive to the Reynolds number, as was found by Falkovich & Pumir (2007). Finally figure 2.2(d) tests our conjecture that $G_{\dot{v}^2}^{\parallel}(r, St)$ in (2.10) dominates at $r/\eta \ll 1$ and $St > St_c$. We see excellent convergence of this term to $G_2^{\parallel}$ in this limit.

Figure 2.3 shows a comparison of the model (2.11) with the fitted coefficients given in table 2.2 with all of the DNS. There is reasonably good correspondence for all of the Stokes numbers. We conclude that while (2.11) has not been derived from first principles, it is consistent with the formulations of Bec et al. (2010) and

Falkovich & Pumir (2007), and it provides a simple, accurate correlation of the data within the dissipation range.

2.3.2 The inertial subrange: second-order statistics

Next we consider the scaling of second-order structure functions in the inertial subrange as a function of the particle Stokes number. In figure 2.4, we show the second-order structure function normalized by the kinetic energy of the (a) fluid and (b) inertial particles, respectively. The collapse of the curves obtained by the latter normalization is quite apparent. We can partially explain this by recognizing

$$G_2^{\parallel}(r, S\,t) = \frac{4}{3} k_p(S\,t)\,[1 - f(r, S\,t)]\ , \tag{2.14}$$

where $k_p(S\,t) \equiv \frac{1}{2}\langle \mathbf{v} \cdot \mathbf{v} \rangle$ is the average particle kinetic energy per unit mass and $f(r, S\,t)$ is the two-particle, longitudinal correlation function (Pope 2000). By normalizing the second-order structure function by the particle kinetic energy, the behaviour of the correlation function (or more precisely one minus this quantity) is isolated, which apparently is much less sensitive to the particle Stokes number. Furthermore, the unexpected non-monotonic trend exhibited by the structure function (which rises then falls with increasing Stokes number) is related to the particle kinetic energy. Figure 2.5 shows the kinetic energy of the particles as a function of Stokes number. Notice the counterintuitive increase at small Stokes numbers. Also shown on the plot are the kinetic energy of the fluid along the particle trajectory (biased sampling) and the kinetic energy of particles along fluid trajectories (filtering). As you can see, the latter is a monotonically decreasing function of Stokes number; indeed, filtering is known to reduce the kinetic energy of the particle field by an amount that scales like

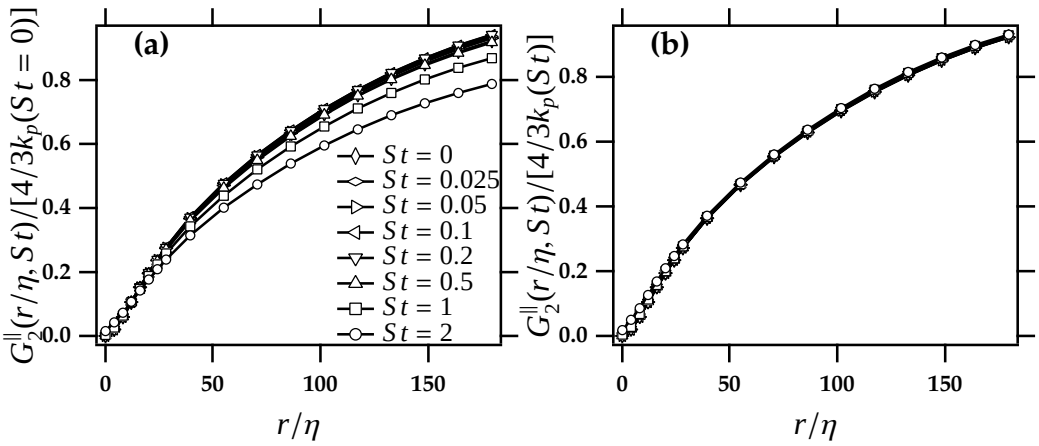

Figure 2.4: Second-order inertial particle structure function for $R_\lambda = 120$ in the inertial subrange normalized by (a) the the fluid kinetic energy; and (b) the kinetic energy of the particle field.

$k_p/k_f = 1/[1 + St f(R_\lambda)]$, where $k_f \equiv \frac{1}{2}\langle \mathbf{u} \cdot \mathbf{u} \rangle$ is the fluid kinetic energy per unit mass (Abrahamson 1975). We conclude that filtering cannot be responsible for the increase in k_p at small Stokes numbers. The biased sampling curve shows the increase at small St and is therefore responsible for the non-monotonic behaviour of $k_p(St)$.

As discussed in Salazar & Collins (2010), the theory of Chun et al. (2005) can be used to estimate the effect of biased sampling in the low Stokes number limit. For a given function of the inertial particle velocity Φ, the average over the inertial particle field (with biased sampling) to leading order in St is given by

$$\langle \Phi \rangle_p = \langle \Phi \rangle + St\tau_\eta \int_{-\infty}^{t} \langle \Phi(t) \left[S^2(s) - W^2(s) \right] \rangle ds \,, \tag{2.15}$$

where S^2 and W^2 are the second invariants of the rate-of-strain and rate-of-rotation tensors, respectively. Equation (2.15) predicts the leading order effect of particle inertial with knowledge only of Lagrangian *fluid* statistics. The solid line in figure 2.5 shows the prediction of the Chun et al. (2005); the slope is in good agreement with the slope found in the DNS at $St = 0$.

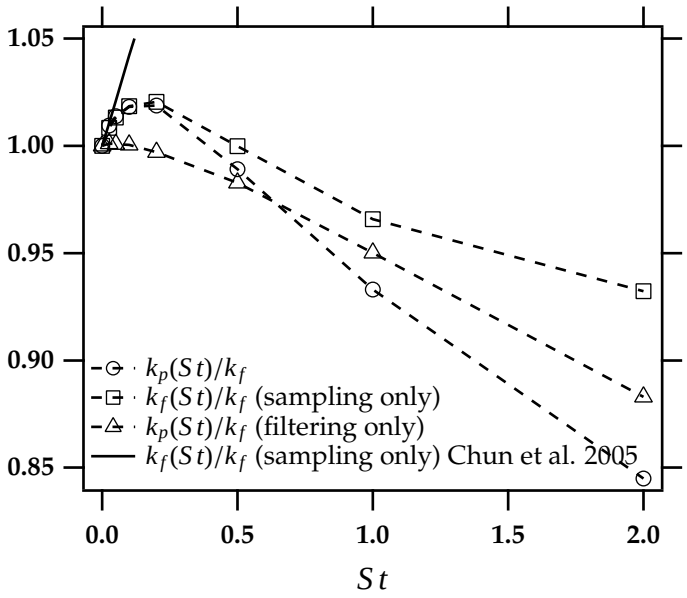

Figure 2.5: Inertial particle mean kinetic energy, normalized by the fluid kinetic energy, as a function of the Stokes number for $R_\lambda = 120$. Notice the ratio increases above one, peaks at $St \approx 0.2$ and thereafter decreases with increasing Stokes number. The solid line is the prediction of (2.15) based on the theory of Chun et al. (2005).

Experimental work by Gibert et al. (2010) at $R_\lambda = 442$ confirms the trend found with Stokes number in the inertial subrange over the range $0 \leq St \leq 0.5$, with $d/\eta \sim 1$ and $\rho_p/\rho = O(1)$. They considered the more general structure function $G_2(r, St) \equiv \langle \Delta\mathbf{v} \cdot \Delta\mathbf{v} \rangle$; however, for isotropic turbulence this can be expressed as $G_2(r, St) = G_2^{\parallel}(r, St) + 2G_2^{\perp}(r, St)$. In the limit $St \ll 1$ if we assume $\dot{\mathbf{v}} \approx \mathbf{a}$ (Maxey 1987), we can express $G_2(r, St)$ as (to leading order in Stokes number)

$$G_2(r, St) = G_2(r, St = 0) + 4\tau_p \langle \varepsilon \rangle \,, \tag{2.16}$$

where we have made use of $\langle \Delta\mathbf{u} \cdot \Delta\mathbf{a} \rangle = -2\langle \varepsilon \rangle$ (Hill 2006). Gibert et al. (2010) derived a theoretical estimate of $\Gamma(r, St) = G_2(r, St)/G_2(r, St = 0)$ by using inertial subrange scaling for the second-order fluid structure function, $G_2(r, St = 0) = 11/3C_2(\langle \varepsilon \rangle r)^{2/3}$, where $C_2 = 2.1$ is a universal constant for fully developed turbulence (Sreenivasan 1995). For heavy particles ($\rho_p/\rho_f \gg 1$), their expression

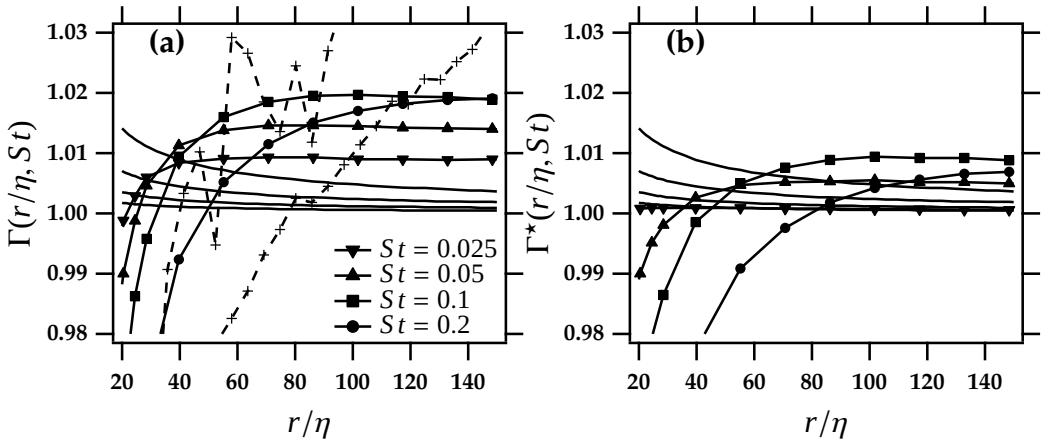

Figure 2.6: Second-order inertial particle structure function for $R_\lambda = 120$ in the inertial subrange normalized by (a) the second-order structure function for the fluid; and (b) the second order structure function for the fluid collocated at inertial particle positions. In (a) also shown (dashed line with crosses) is the experimental data from Gibert et al. (2010). The lower curve is for $St = 0.24$ and upper curve is for $St = 0.45$. The solid lines correspond to the expression given by (2.17), where the curves rise with increasing St.

reduces to

$$\Gamma(r, St) = 1 + \frac{12}{11C_2} St \left(\frac{r}{\eta}\right)^{-2/3} . \tag{2.17}$$

Figure 2.6(a) shows the ratio $\Gamma(r, St)$ for our DNS and the experimental data of Gibert et al. (2010). Also shown is the theoretical expression given by (2.17). The DNS data shows that at the lower values of Stokes number the trend is increasing and then at higher Stokes numbers it begins to decrease, eventually going below unity (not shown). This is in qualitative agreement with the experimental study, except for the range of St at which we observe the increase, $0 \leq St \lesssim 0.2$. The theoretical curves show a very small correction to the fluid particle structure function and in general are not in quantitative agreement with our DNS. It must be noted that (2.17) does not take into account the effects due to biased sampling. The effects of biased sampling are not significant on

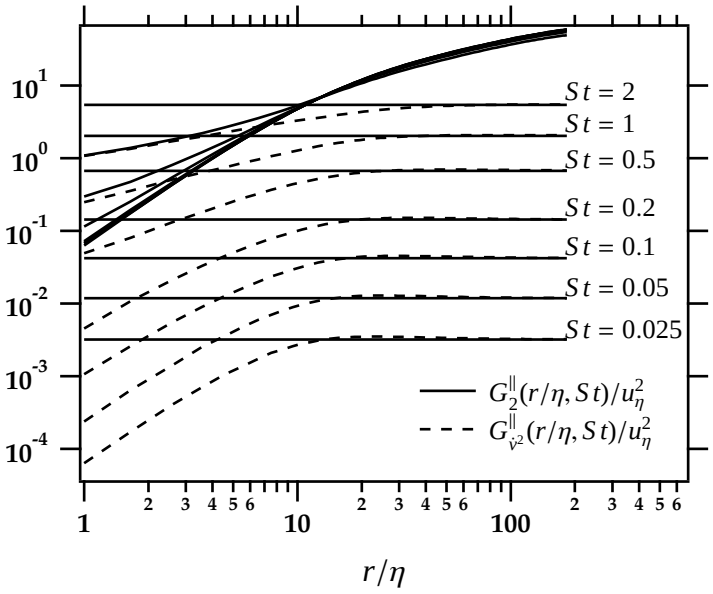

Figure 2.7: Figure showing $G_{\dot{v}^2}^{\parallel}(r/\eta, St)$ in the inertial subrange (flat) for $R_\lambda = 120$. The solid horizontal lines are equal to $2/3\tau_p^2\langle\dot{\mathbf{v}}\cdot\dot{\mathbf{v}}\rangle$.

$G_2(r, St = 0)$, but the same cannot be said about $\langle\varepsilon\rangle$. From (2.16) we can consider the effects of biased sampling by averaging fluid quantities over inertial particle trajectories. We define $\Gamma^\star(r, St)$ as the ratio of the inertial particle structure function to the fluid structure function computed along inertial particle paths $G_2^\star(r, St)$. This gives,

$$\Gamma^\star(r, St) = 1 + \frac{4\tau_p\langle\varepsilon\rangle_p}{G_2^\star(r, St)}\,, \tag{2.18}$$

where $\langle\cdot\rangle_p$ indicates an ensemble of a fluid quantity at inertial particle locations. We find that (2.18), shown in figure 2.6(b) agrees reasonably well with the DNS for $St \leq 0.1$ and therefore provides an alternate explanation for the increasing trend with Stokes number found at small values of that parameter.

We can exploit the decomposition given in (2.10) in the inertial subrange as well, and this provides some additional insight on the behaviour of the structure function at higher values of the Stokes number. Figure 2.7(a) shows $G_2^{\parallel}(r, St)$ and $G_{\dot{v}^2}^{\parallel}(r, St)$ in the inertial subrange for several values of the Stokes number.

Remarkably, the curves for $G^{\parallel}_{\dot{v}^2}(r, St)$ are nearly flat, indicating the correlation throughout the inertial subrange is independent of the separation distance, but sensitive to the value of the Stokes number. The solid horizontal lines in the plot are given by $2/3\tau_p^2\langle\dot{\mathbf{v}}\cdot\dot{\mathbf{v}}\rangle$, indicating that the particle accelerations in the inertial subrange are completely uncorrelated (i.e., $\langle\dot{\mathbf{v}}(\mathbf{x})\cdot\dot{\mathbf{v}}(\mathbf{x}+\mathbf{r})\rangle = 0$ for $\mathbf{r}$ in the inertial subrange). For $St \geq 0.5$ the "caustic" contribution to the second-order structure function, in the form of $G^{\parallel}_{\dot{v}^2}$, is non-negligible. All of these results taken together are quite unexpected and require further investigation.

2.3.3 The inertial subrange: higher-order statistics

In order to study the intermittency characteristics of the inertial-particle relative velocity, we consider higher-order structure functions in the inertial subrange. The results for the longitudinal and transverse structure functions of orders 2–8 for $R_\lambda = 60$ and 120 are given in figures 2.8 and 2.9, respectively. It is readily apparent that departures of the longitudinal exponents from K41 and K62 increase with both the power p and Stokes number St. These departures are often used as a measure of the internal intermittency (Pope 2000). Turbulence models, in particular multifractal (Frisch 1995) and shell (Biferale 2003) models have had reasonable success in predicting the dependence of these exponents on the order. The higher intermittency corrections for the inertial particles are reminiscent of a similar trend found for scalars (Warhaft 2000); however, the degree is even greater for the inertial particles and grows with the Stokes number. The same cannot be said about the transverse structure function, which exhibits very different behaviour. Specifically, for $p < 6$, the exponents can be substantially larger than the expected value from K62. Moreover, the exponents increase with

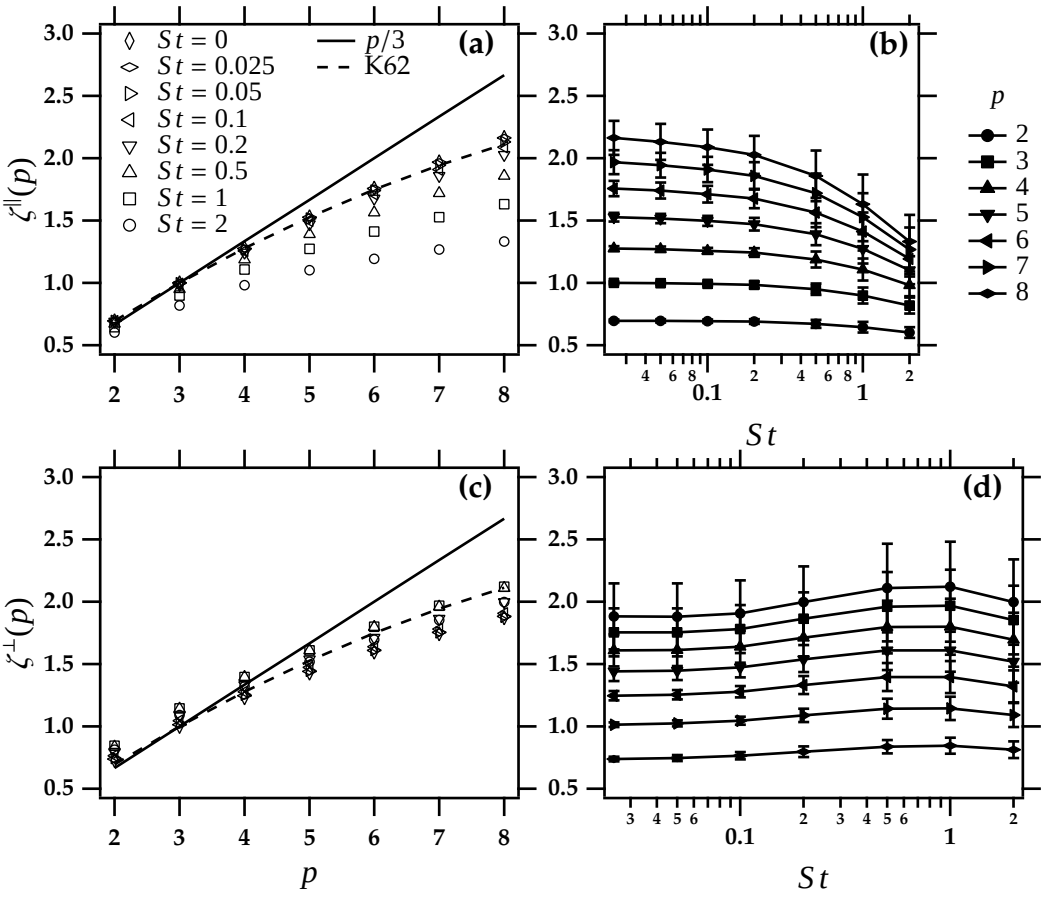

Figure 2.8: Exponents for the inertial particle structure function in the longitudinal (a, b) and transverse (c, d) directions for $R_\lambda = 60$ and at the indicated Stokes number and power. Vertical lines are error bars indicating one standard deviation.

increasing Stokes number, the opposite trend to that found for the longitudinal structure function. Unlike the case of the fluid structure function computed in an incompressible flow, relations between the longitudinal and transverse inertial particle structure functions are not available.

As noted by Bec et al. (2006) and Ayyalasomayajula et al. (2008), inertial particle statistics are impacted by both the biased sampling due to preferential concentration (Balachandar & Eaton 2010) and the filtering of the underlying fluid fluctuations by caused by inertia. In order to separate these two effects, we con-

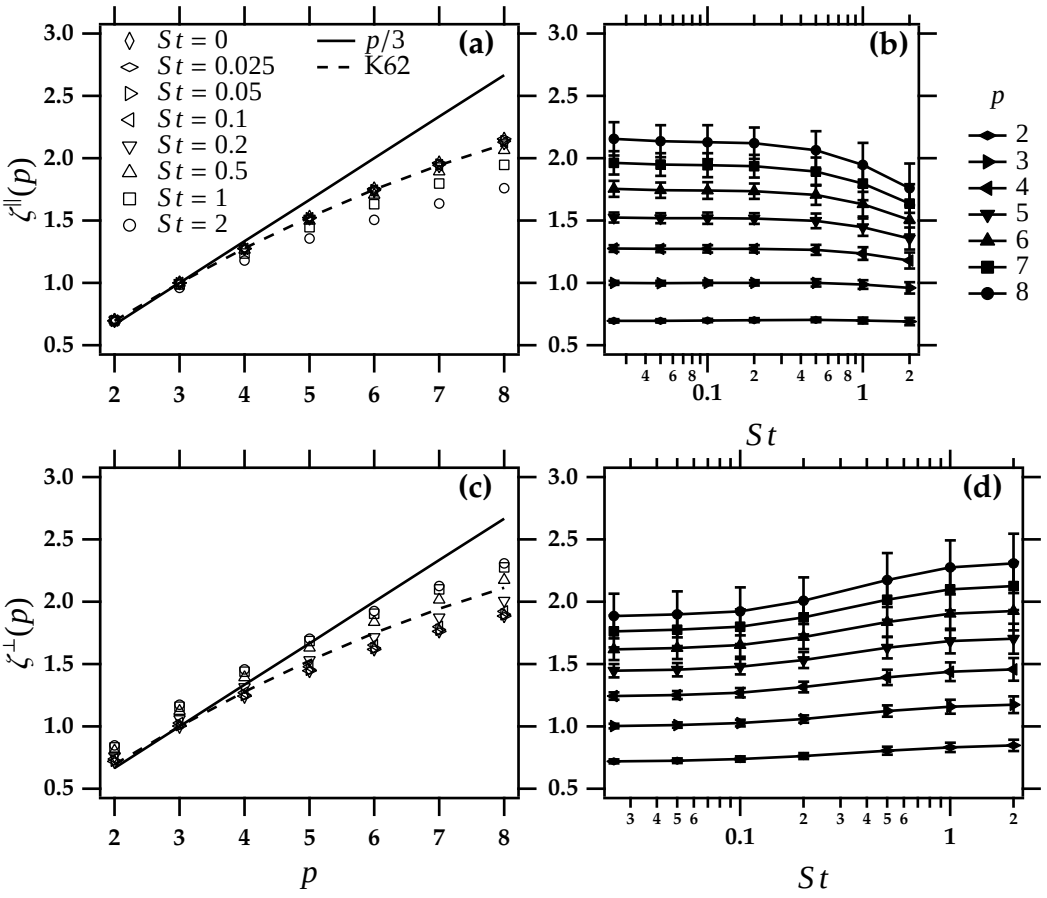

Figure 2.9: Exponents for the inertial particle structure function in the longitudinal (a, b) and transverse (c, d) directions for $R_\lambda = 120$ and at the indicated Stokes number and power. Vertical lines are error bars indicating one standard deviation.

sider structure functions of fluid particles along inertial particle paths (biased sampling, no filtering) and inertial particles along fluid particle paths (filtering, no biased sampling). The results for the longitudinal structure function of orders 2–8 are shown in figure 2.10. It is readily apparent that filtering (not biased sampling) is the dominant effect controlling the changes in the structure function exponents. This is in stark contrast to inertial particle acceleration statistics. As shown by Bec et al. (2006), biased sampling is the dominant effect at low St, although there is still an effect of filtering on the tails of the probability density

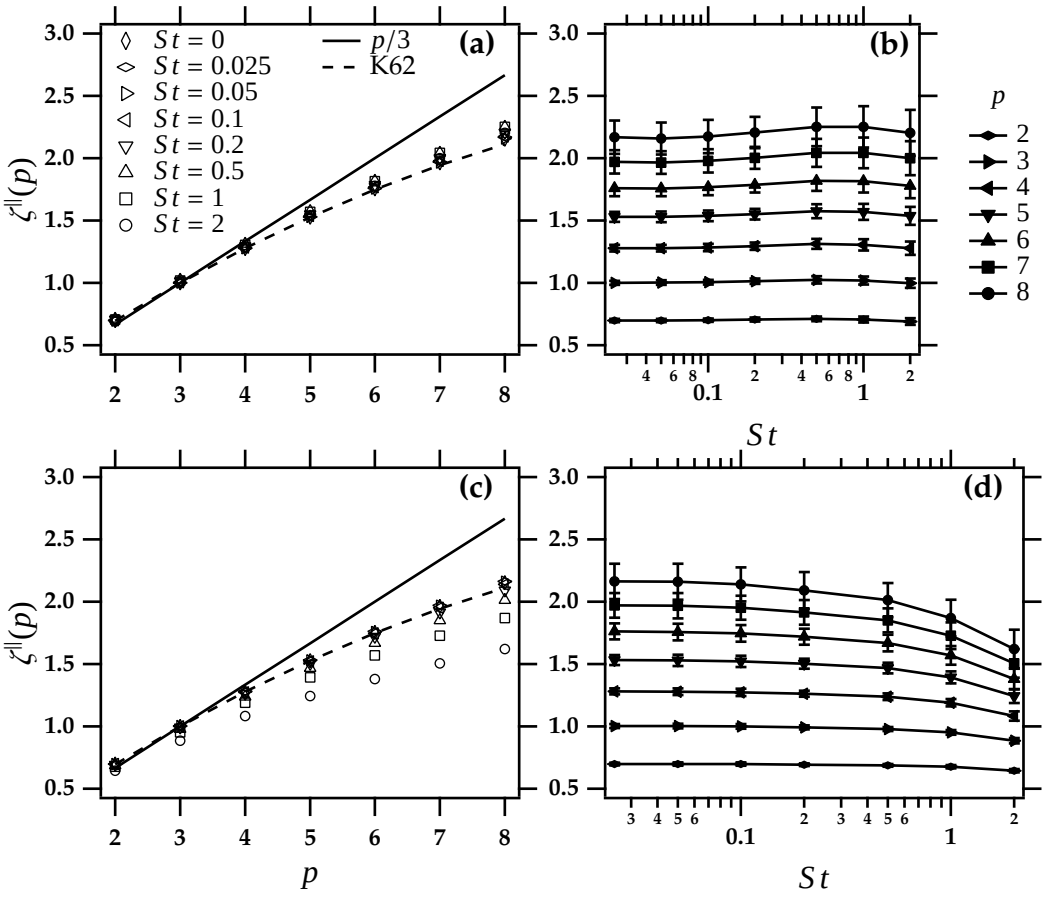

Figure 2.10: Exponents for the longitudinal structure function of orders 2–8 at $R_\lambda = 120$ for: fluid particles along inertial particle trajectories as a function of (a) power p (at the indicated Stokes number) and (b) Stokes number (at the indicated power p), isolating the effect of biased sampling; inertial particles along fluid particle trajectories as a function of (c) power p (at the indicated Stokes number) and (d) Stokes number (at the indicated power p), isolating the effect of filtering.

function of acceleration (Ayyalasomayajula et al. 2008). Why it is that filtering is playing a more significant role in the structure function is not entirely clear. We conjecture that a single-particle statistic such as the particle acceleration can be more strongly impacted by biased sampling than a two-particle statistic such as the structure function, since in the case of the latter, it is the combined environment of the two particles that will matter, and this necessarily will diminish

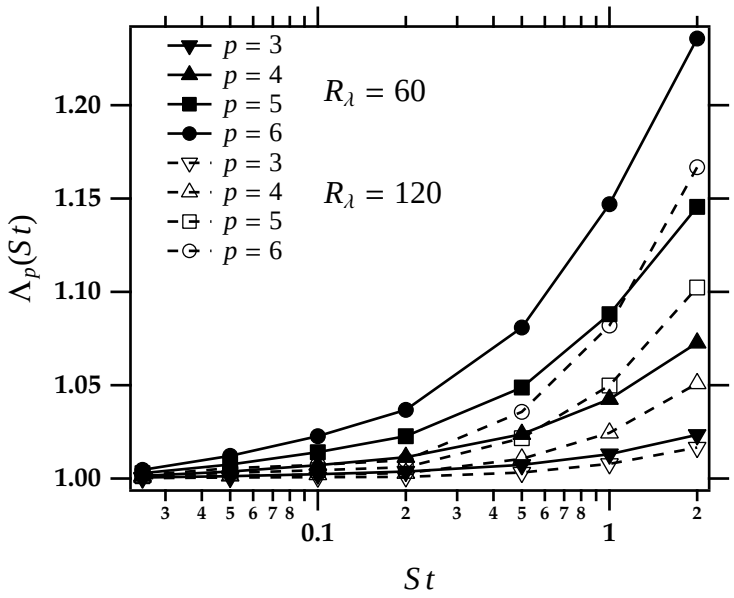

Figure 2.11: Normalized moment ratio as defined in (2.19), evaluated in the inertial subrange at the indicated power. Filled and open symbols correspond to $R_\lambda = 60$ and 120, respectively.

the biased sampling effect.

An alternative measure of the 'internal intermittency' of the inertial particle velocity field can be found from the following ratio

$$\Lambda_p \equiv \frac{G_p^{\parallel}(r, St)/\left[G_2^{\parallel}(r, St)\right]^{p/2}}{G_p^{\parallel}(r, St=0)/\left[G_2^{\parallel}(r, St=0)\right]^{p/2}} \,. \tag{2.19}$$

Note that by definition $\Lambda_2 = 1$ and $\Lambda_p > 1$ implies the particle velocity is more intermittent (has a broader probability density function) than the fluid velocity. Figure 2.11 shows the behaviour of Λ_p in the inertial subrange as a function of the Stokes number. In general, Λ_p increases with increasing Stokes number and power p, suggesting a growth in intermittency with both parameters; these results are also confirmed by examining the probability density functions of relative velocity in the inertial subrange (not shown). Perhaps unexpected is that the relative increase in intermittency with respect to the fluid as a function of St is smaller at $R_\lambda = 120$.

2.4 Conclusions

The scaling of relative velocity statistics in both the dissipation range and the inertial subrange is studied. In the dissipation range we find support for a Reynolds number dependent critical Stokes number St_c, below which there are no caustics. In our present DNS $St_c \approx 0.2.$, the same value at which the study by Falkovich & Pumir (2007) began to find significant caustic effects, over a similar range of R_λ. For $St \geq 0.5$ we find good agreement with theory developed by Wilkinson et al. (2006) and Falkovich & Pumir (2007). Our findings for the scaling exponent $\xi_2(St \geq 0.5)$ of the structure function within the dissipation range are also consistent with recent work by Bec et al. (2010). In the inertial subrange we find qualitative agreement with measurements of the inertial particle second order structure function reported by Gibert et al. (2010) at higher R_λ than available in our DNS. Inertial subrange scaling of inertial particle structure functions of order 2 up to 8 is found to resemble that of increasingly intermittent turbulence as St increases, demonstrated by the scaling exponents $\zeta_p(St)$ and by normalized moment ratios. By manipulating the evolution equations for inertial particles and fluid particles we are able to isolate inertial effects of biased sampling and filtering. We find that unlike single-particle statistics where biased sampling largely accounts for the observed behavior at low St and filtering at high St, it is filtering that dominates at all St for two-particle statistics in the inertial subrange. We introduce the caustic structure function as a means of quantifying the underlying mechanism of caustic formation not only in the dissipation range, but also in the inertial subrange. We believe this work will prove to be useful in modeling the inertial particle collision kernel and relative dispersion in the inertial subrange.

The authors are grateful to J. Bec and L.-P. Wang for insightful discussions at the Kavli Institute for Theoretical Physics at the University of Santa Barbara during the "Physics of Climate Change" program held in 2008 that was sponsored by the National Science Foundation under grant PHY-0551164, and to Z. Warhaft and E. Bodenschatz for their contributions to the work. This study was supported by the National Science Foundation under grant CBET-0756510. J.P.L.C.S. acknowledges support from the Brazilian Ministry of Education through the CAPES agency.

REFERENCES

Abrahamson J. 1975. Collision rates of small particles in a vigorously turbulent fluid. *Chem. Eng. Sci.* 30:1371–1379

Ayala O, Rosa B, Wang LP, Grabowski WW. 2008. Effects of turbulence on the geometric collision rate of sedimenting droplets. part 1. results from direct numerical simulation. *New J. Phys.* 10:075015

Ayyalasomayajula S, Gylfason A, Collins LR, Bodenschatz E, Warhaft Z. 2006. Lagrangian measurements of inertial particle accelerations in grid generated wind tunnel turbulence. *Phys. Rev. Lett.* 97:144507

Ayyalasomayajula S, Warhaft Z, Collins LR. 2008. Modeling inertial particle acceleration statistics in isotropic turbulence. *Phys. Fluids* 20:094104

Balachandar S, Eaton JK. 2010. Turbulent dispersed multiphase flow. *Ann. Rev. Fluid Mech.* 42:111–133

Bec J, Biferale L, Boffetta G, Celani A, Cencini M, et al. 2006. Acceleration statistics of heavy particles in turbulence. *J. Fluid Mech.* 550:349–358

Bec J, Biferale L, Cencini M, Lanotte AS, Musacchio S, Toschi F. 2007. Heavy particle concentration in turbulence at dissipative and inertial scales. *Phys. Rev. Lett.* 98:084502

Bec J, Biferale L, Cencini M, Lanotte AS, Toschi F. 2010. Intermittency in the velocity distribution of heavy particles in turbulence. *J. Fluid Mech.* 646:527–536

Berrut JP, Trefethen LN. 2004. Barycentric Lagrange interpolation. *Siam Rev.* 46:501–517

Biferale L. 2003. Shell models of energy cascade in turbulence. *Ann. Rev. Fluid Mech.* 35:441–468

Boivin M, Simonin O, Squires KD. 1998. Direct numerical simulation of turbulence modulation by particles in isotropic turbulence. *J. Fluid Mech.* 375:235–263

Brucker KA, Isaza JC, Vaithianathan T, Collins LR. 2007. Efficient algorithm for simulating homogeneous turbulent shear flow without remeshing. *J. Comp. Phys.* 225:20–32

Chaumat L, Brenguier JL. 2001. Droplet spectra broadening in cumulus clouds. Part II: Microscale droplet concentration heterogeneities. *J. Atmos. Sci.* 58:642–654

Chen L, Gogo S, Vassilicos JC. 2006. Turbulent clustering of stagnation points and inertial particles. *J. Fluid Mech.* 553:143–155

Chun J, Koch DL, Rani S, Ahluwalia A, Collins LR. 2005. Clustering of aerosol particles in isotropic turbulence. *J. Fluid Mech.* 536:219–251

Coleman SW, Vassilicos JC. 2009. A unified sweep-stick mechanism to explain particle clustering in two- and three-dimensional homogeneous, isotropic turbulence. *Phys. Fluids* 21:113301

Collins LR, Keswani A. 2004. Reynolds number scaling of particle clustering in turbulent aerosols. *New Journal of Physics* 6:119

de Jong J, Salazar JPLC, Cao L, Woodward SH, Collins LR, Meng H. 2010. Measurement of inertial particle clustering and relative velocity statistics in isotropic turbulence using holographic imaging. *Int. J. Multiphase Flow* 36:324–332

Eaton JK, Fessler JR. 1994. Preferential concentration of particles by turbulence. *Int. J. Multiphase Flow* 20:169–209

Faeth GM. 1996. Spray combustion phenomena. *Int. Combust. Symp.* 26:1593–1612

Falkovich G, Fouxon A, Stepanov MG. 2002. Acceleration of rain initiation by cloud turbulence. *Nature* 419:151–154

Falkovich G, Pumir A. 2007. Sling effect in collisions of water droplets in turbulent clouds. *J. Atm. Sci.* 64:4497

Frisch U. 1995. *Turbulence: The Legacy of A. N. Kolmogorov*. Cambridge University Press

Gibert M, Xu H, Bodenschatz E. 2010. Inertial effects on two-particle relative dispersion in turbulent flows. *Euro. Phys. Lett.* Submitted

Goto S, Vassilicos JC. 2008. Sweep-stick mechanism of heavy particle clustering in fluid turbulence. *Phys. Rev. Lett.* 100:035504

Grabowski WW, Vaillancourt P. 1999. Comments on 'Preferential concentration of cloud droplets by turbulence: Effects on the early evolution of cloud droplet spectra' by Shaw, Reade, Collins and Verlinde. *J. Atmos. Sci.* 56:1433–1436

Hill RJ. 2006. Opportunities for use of exact statistical equations. *J. Turbulence* 7:N43

Ishihara T, Gotoh T, Kaneda Y. 2009. Study of high-Reynolds-number isotropic turbulence by direct numerical simulation. *Ann. Rev. Fluid Mech.* 41:165–180

Johansen A, Oishi JS, Mac Low MM, Klahr H, Henning T. 2007. Rapid planetesimal formation in turbulent circumstellar disks. *Nature* 448:1022–1025

Kolmogorov AN. 1941. The local structure of turbulence in an incompressible viscous fluid for very large Reynolds numbers. *Dokl. Akad. Nauk. SSSR* 30:299–303

Li WI, Perzl M, Heyder J, Langer R, Brain JD, et al. 1996. Aerodynamics and aerosol particle deaggregation phenomena in model oral-pharyngeal cavities. *J. Aerosol. Sci.* 27:1269–1286

Malkiel E, Abras JN, Widder EA, Katz J. 2006. On the spatial distribution and nearest neighbor distance between particles in the water column determined from in situ holographic measurements. *J. Plankton Res.* 28:149–170

Maxey MR. 1987. The gravitational settling of aerosol particles in homogeneous turbulence and random flow fields. *J. Fluid Mech.* 174:441–465

Maxey MR, Riley JJ. 1983. Equation of motion for a small rigid sphere in a nonuniform flow. *Phys. Fluids* 26:883–889

McQuarrie DA. 1976. *Statistical Mechanics*. New York: Harper & Row

Moody EG, Collins LR. 2003. Effect of mixing on nucleation and growth of titania particles. *Aerosol Sci. Tech.* 37:403–424

Pope SB. 2000. *Turbulent Flows*. New York: Cambridge University Press

Reade WC, Collins LR. 2000a. Effect of preferential concentration on turbulent collision rates. *Phys. Fluids* 12:2530–2540

Reade WC, Collins LR. 2000b. A numerical study of the particle size distribution of an aerosol undergoing turbulent coagulation. *J. Fluid Mech.* 415:45–64

Saffman PG, Turner JS. 1956. On the collision of drops in turbulent clouds. *J. Fluid Mech.* 1:16–30

Salazar JPLC, Collins LR. 2010. Acceleration statistics in homogeneous isotropic turbulence: the effects of filtering, biased sampling and flow topology. *Phys. Fluids* In preparation

Salazar JPLC, de Jong J, Cao L, Woodward S, Meng H, Collins LR. 2008. Experimental and numerical investigation of inertial particle clustering in isotropic turbulence. *J. Fluid Mech.* 600:245–256

Saw EW, Shaw RA, Ayyalasomayajula S, Chuang PY, Gylfason A. 2008. Inertial clustering of particles in high-Reynolds-number turbulence. *Phys. Rev. Lett.* 100:214501

Shaw RA. 2003. Particle-turbulence interactions in atmospheric clouds. *Annu. Rev. Fluid Mech.* 35:183–227

Shaw RA, Reade WC, Collins LR, Verlinde J. 1998. Preferential concentration of cloud droplets by turbulence: effects on the early evolution of cumulus cloud droplet spectra. *J. Atmos. Sci.* 55:1965–1976

Shotorban B, Balachandar S. 2006. Particle concentration in homogeneous shear turbulence simulated via Lagrangian and equilibrium Eulerian approaches. *Phys. Fluids* 18:065105

Shotorban B, Balachandar S. 2009. Two-fluid approach for direct numerical simulation of particle-laden turbulent flows at small Stokes numbers. *Phys. Rev. E* 79:056703

Siebert H, Gerashchenko S, Lehmann K, Gylfason A, Collins LR, et al. 2010a. Towards understanding the role of turbulence on droplets in clouds: In situ and laboratory measurements, and numerical modeling. *Atmos. Res.* In review

Siebert H, Shaw RA, Warhaft Z. 2010b. Statistics of small scale velocity fluctuations in marine stratocumulus clouds. *J. Atmos. Sci.* 67:262–273

Squires KD, Eaton JK. 1991. Preferential concentration of particles by turbulence. *Phys. Fluids A* 3:1169–1178

Sreenivasan KR. 1995. On the universality of the Kolmogorov constant. *Phys. Fluids* 7:2778–2784

Sundaram S, Collins LR. 1997. Collision statistics in an isotropic, particle-laden turbulent suspension i. direct numerical simulations. *J. Fluid Mech.* 335:75–109

Sundaram S, Collins LR. 1999. A numerical study of the modulation of isotropic turbulence by suspended particles. *J. Fluid Mech.* 379:105–143

Vaillancourt PA, Yau MK, Grabowski WW. 2001. Microscopic approach to cloud droplet growth by condensation. Part I: Model description and results without turbulence. *J. Atmos. Sci.* 58:1945–1965

Wang LP, Maxey MR. 1993. Settling velocity and concentration distribution of heavy particles in homogeneous isotropic turbulence. *J. Fluid Mech.* 256:27–68

Wang LP, Wexler AS, Zhou Y. 2000. Statistical mechanical description and modeling of turbulent collision of inertial particles. *J. Fluid Mech.* 415:117–153

Warhaft Z. 2000. Passive scalars in turbulent flows. *Ann. Rev. Fluid Mech.* 32:203–240

Warhaft Z. 2009a. Laboratory studies of droplets in turbulence: towards understanding the formation of clouds. *Fluid Dyn. Res.* 41:011201

Warhaft Z. 2009b. Why we need turbulence experiments at high Reynolds number. *Fluid Dyn. Res.* 41:021401

Wilkinson M, Mehlig B, Bezuglyy V. 2006. Caustic activation of rain showers. *Phys. Rev. Lett.* 97:048501

Wood AM, Hwang W, Eaton JK. 2005. Preferential concentration of particles in homogeneous and isotropic turbulence. *Int. J. Multiphase Flow* 31:1220–1230

Yudine MI. 1959. Physical considerations on heavy-particle dispersion. *Adv. Geophys.* 6:185–191

Zaichik LI, Alipchenkov VM. 2003. Pair dispersion and preferential concentration of particles in isotropic turbulence. *Phys. Fluids* 15:1776–1787

Zaichik LI, Alipchenkov VM. 2009. Statistical models for predicting pair dispersion and particle clustering in isotropic turbulence and their applications. *New J. Phys.* 11:103018

Zhou Y, Wexler AS, Wang LP. 2001. Modelling turbulent collision of bidisperse inertial particles. *J. Fluid Mech.* 433:77–104

CHAPTER 3

ACCELERATION STATISTICS IN HOMOGENEOUS ISOTROPIC TURBULENCE: THE EFFECTS OF FILTERING AND BIASED SAMPLING AND FLOW TOPOLOGY*

In this study we investigate the effect of biased sampling, i.e., the preference of inertial particles for regions of the flow with low vorticity, and filtering, i.e., the tendency of inertial particles to attenuate the fluid velocity fluctuations, on the acceleration probability density function of inertial particles. In particular, we find that the concept of biased filtering presented in Ayyalasomayajula et al. (2008) is relevant to higher order moments of acceleration. Flow topology and its connection to acceleration is explored through invariants of the velocity-gradient, strain-rate and rotation-rate tensors. A semi-quantitative analysis is performed where we assess the contribution of specific flow topologies to acceleration moments. Our findings show that the contributions of regions of high rotation and low strain decrease significantly with Stokes number, a non-dimensional measure of particle inertia. The contribution from regions of low rotation and high strain exhibit a peak at a Stokes number of approximately 0.2. Following the methodology of Ooi et al. (1999), we compute mean conditional trajectories in planes formed by pairs of tensor invariants in time. Among the interesting findings is the existence of a stable focus in the plane formed by the second invariants of the strain-rate and rotation-rate tensors. Contradicting the results in Ooi et al. (1999), we find a stable focus in the plane formed by the second and third invariants of the strain-rate tensor. We confirm the conjecture presented in Collins & Keswani (2004) at a higher Reynolds number than the original study, whereby inertial particle clustering is expected to saturate at

*To be submitted to *Physics of Fluid*.

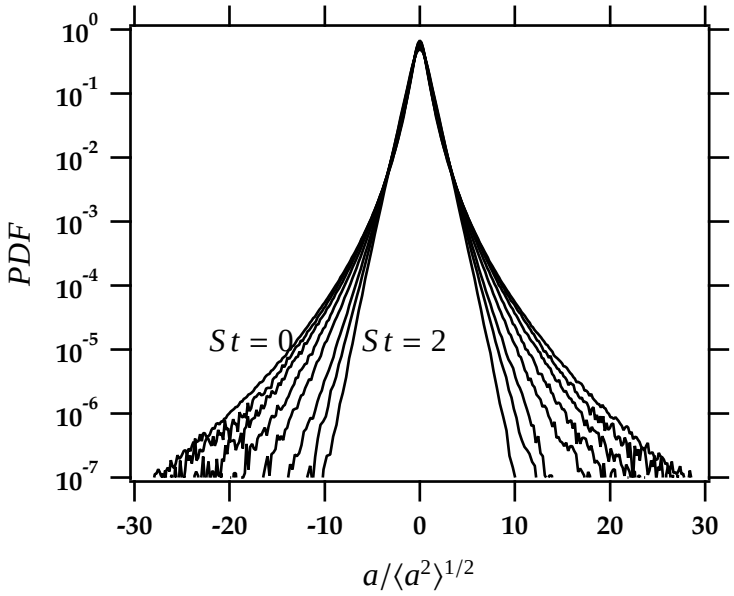

Figure 3.1: Normalized acceleration PDFs for different Stokes numbers. From the outer- to the innermost PDF: $St = 0$, $St = 0.025$, $St = 0.05$, $St = 0.1$, $St = 0.2$, $St = 0.5$, $St = 1$, and $St = 2$.

large Reynolds number. This result is confirmed by theory presented in Chun et al. (2005). This work complements the study of Bec et al. (2006) and we believe is useful for those interested in modeling inertial particle acceleration.

3.1 Introduction

Acceleration is a key component of stochastic models that possess Reynolds number dependence, multiple time-scales and a one-time continuously differentiable velocity autocorrelation function (Pope 2002, Sawford 1991). Because of the usefulness of stochastic equations in models for turbulent relative dispersion (Salazar & Collins 2009, Sawford 2001) and Lagrangian PDF methods (Pope 1985, 1994), a large number of DNS and experiments have been devoted to the study of acceleration statistics of fluid particles (Biferale et al. 2004, Gylfason

et al. 2004, La Porta et al. 2001, Mordant et al. 2004a,b, Reynolds et al. 2005, Sawford et al. 2003, Vedula & Yeung 1999, Voth et al. 2002, 1998, Yeung 1997, Yeung et al. 2007, 2006a,b). Beginning with the work of Bec et al. (2006), acceleration statistics of inertial particles have been the focus of many recent experiments (Ayyalasomayajula et al. 2006, Brown et al. 2009, Gerashchenko et al. 2008, Qureshi et al. 2008, Volk et al. 2008, Xu & Bodenschatz 2008) and DNS (Calzavarini et al. 2009, Jung et al. 2008, Lavezzo et al. 2009, Toschi & Bodenschatz 2009). The current work is intended to provide a better understanding of inertial particle acceleration, aiding the development of finite-inertia particle models.

Particle inertia is quantified by the Stokes number, which for a particle of diameter d and density ρ_p embedded in a fluid of kinematic viscosity ν and density ρ is given by $St_f \equiv \tau_p/\tau_f$, where $\tau_p \equiv \frac{1}{18}\frac{\rho_p}{\rho}\frac{d^2}{\nu}$ is the particle relaxation time and τ_f is a flow timescale, typically taken to be the Kolmogorov timescale $\tau_\eta \equiv \left(\nu^3/\langle\varepsilon\rangle\right)^{1/4}$, where ε is the instantaneous, local turbulent kinetic energy dissipation rate. There are two important effects due to particle inertia. Previous work has established that at low to moderate St[1] inertial particles selectively sample the fluid velocity field owing to a centrifuging mechanism that ejects them from regions of high rotation causing them to accumulate in regions of high strain (Maxey 1987). This results in particle number densities much larger than the expected value at small separation distances, an effect referred to as clustering or preferential concentration (Bec et al. 2007, Eaton & Fessler 1994, IJzermans et al. 2009, Salazar et al. 2008, Saw et al. 2008, Shaw et al. 1998, Squires & Eaton 1991b, Sundaram & Collins 1997, Wang & Maxey 1993, Wood et al. 2005). At larger St there is evidence supporting the clustering of particles in the

[1]Whenever the subindex is omitted, the Stokes number is based upon the Kolmogorov time scale.

vicinity of acceleration stagnation points (Chen et al. 2006, Coleman & Vassilicos 2009, Goto & Vassilicos 2008). We refer to this as biased sampling, whereby fluid statistics calculated along inertial particle paths will differ from those calculated along a fluid particle path. Secondly, inertial particles are less responsive to fluid acceleration as a result of inertial damping, i.e., inertial particles act as low-pass filters of the frequency content of the underlying fluid velocity field. We shall henceforth refer to this effect as filtering. Biased sampling and filtering are not decoupled since both have their origin in the particle inertia. However, it is possible to artificially decouple these effects by manipulating the evolution equations for inertial particles, a technique employed originally by Bec et al. (2006) in the study of the inertial particle acceleration probability density function. In this paper we employ a similar method to isolate effects of sampling and filtering on fluid particle acceleration statistics.

Advances in particle tracking methods and technology has enabled the study of fluid and inertial particle Lagrangian statistics in laboratory turbulent flows (Berg et al. 2006, 2009, Bourgoin et al. 2006, Gerashchenko et al. 2008, Gibert et al. 2009, La Porta et al. 2001, Lüthi et al. 2007, Malik et al. 1993, Mordant et al. 2004a,b, Ott & Mann 2000, Ouellette et al. 2006a,b, Virant & Dracos 1997, Volk et al. 2008, Voth et al. 2002, 1998, Xu et al. 2006a,b, 2008), a realm previously only accessible to direct numerical simulation (DNS) (Benzi et al. 2009, Biferale et al. 2008, 2005, Squires & Eaton 1991a, Yeung 1994, 2001, 2002, Yeung & Borgas 2004, Yeung & Pope 1989, Yeung et al. 2006a,b). In the context of inertial particles, Lagrangian measurements in the Cornell wind tunnel (Ayyalasomayajula et al. 2006) showed that the normalized acceleration probability density function (PDF) became less intermittent with increasing Stokes number, as can be seen in Figure 3.1 from the present study. This behavior is non-trivial since the accelera-

tion variance of inertial particles diminishes with increasing Stokes number (Bec et al. 2006). Therefore, a narrowing of the tails in the normalized PDF tails from this effect cannot be explained solely on grounds of the reduction in acceleration variance. The DNS study of Bec et al. (2006) addressed this issue by sampling fluid particle statistics along inertial particle trajectories. They showed excellent agreement between the PDF of fluid acceleration sampled along inertial particle trajectories and the corresponding PDF for inertial particles at $St = 0.16$ and $R_\lambda = 185$, where R_λ is the Taylor microscale Reynolds number. Hence the authors concluded that the change in the PDF shape at low St can be explained by the biased sampling of the flow field by inertial particles. However, results from a vortex model presented in Ayyalasomayajula et al. (2008) showed that even at low St biased sampling alone does not capture the complete effect of inertia on the acceleration PDF tails. As explained by the authors, this can be better understood by considering an inertial particle subject to a sinusoidal fluid acceleration with frequency ω and magnitude $\sqrt{2}\mathcal{A}$. It was shown that the ratio of inertial particle acceleration variance $\langle a_p^2 \rangle$ to the fluid particle acceleration variance $\langle a_f^2 \rangle$ over one period of oscillation is,

$$\frac{\langle a_p^2 \rangle}{\langle a_f^2 \rangle} = \frac{1}{1 + St_\omega^2}, \tag{3.1}$$

where $St_\omega \equiv \tau_p \omega$ is the Stokes number based on the oscillation frequency. Equation 3.1 shows that the filtering is a function of the magnitude of the acceleration event $\mathcal{A}$ inasmuch as ω is a function of $\mathcal{A}$. They conjectured that if the timescale of the acceleration event is a function of its magnitude, then there will be a biased filtering of the velocity field, i.e, a particle may filter small- and large-magnitude events differently. Results from the vortex model supported their conjecture that $\omega = f(\mathcal{A})$. In the current study we also find that the acceleration time scale decreases as the magnitude of the acceleration event increases

and show that filtering still has an effect on the acceleration PDF tail at Stokes numbers as low as 0.2.

Complementing the work of Bec et al. (2006), we study the effects of biased sampling and filtering on the tails of the acceleration PDF and the acceleration autocorrelation function using DNS. We also investigate the relationship between the acceleration magnitude and the local flow topology and Stokes number in the context of filtering and biased sampling. We use invariant plots of the velocity-gradient, rotation-rate and strain-rate tensors to characterize flow topology following the original work of Chong et al. (1990).

In §3.2 the DNS and particle codes are briefly described, with emphasis on the method used to isolate the effects of biased sampling and filtering. In the first part of §3.3 we present our results for the acceleration PDF and the acceleration autocorrelation function, the findings of which support the model proposed by Ayyalasomayajula et al. (2008). In the second part we discuss flow topology and how it relates to acceleration events as a function of Stokes number. In §3.4 we summarize our main findings and offer suggestions towards future research on the subject.

3.2 Numerical methods

The pseudo-spectral DNS code we use is thoroughly described in Brucker et al. (2007). Of particular relevance to this study is the forcing scheme we use to obtain statistically stationary turbulence. Energy is injected in the two lowest wavenumbers at each time step offsetting the losses in kinetic energy owing to viscous forces, such that the total kinetic energy remains constant throughout

Table 3.1: Table of DNS flow statistics. The turbulent kinetic energy is given by $\int_0^{\kappa_{\max}} E(\kappa)d\kappa$, where $E(\kappa)$ is the energy spectrum function and $\kappa_{\max}$ is the largest resolved wavenumber. The longitudinal integral length scale is given by $L = \pi/(2u'^2)\int_0^{\kappa_{\max}} [E(\kappa)/\kappa]\, d\kappa$.

	units	
Reynolds number $R_\lambda = u'^2\sqrt{15/(\nu\langle\varepsilon\rangle)}$	—	120
Turbulent kinetic energy k	$\left[\mathrm{L^2T^{-2}}\right]$	1.43
Turbulent intensity $u' = \sqrt{2/3k}$	$\left[\mathrm{LT^{-1}}\right]$	0.98
Turbulent energy dissipation rate ϵ	$\left[\mathrm{L^2T^{-3}}\right]$	0.32
Longitudinal integral scale L	[L]	1.44
Integral time scale $T = L/u'$	[T]	1.48
Kolmogorov length scale η	[L]	0.017
Kolmogorov time scale τ_η	[T]	0.097
Kolmogorov velocity scale u_η	$\left[\mathrm{LT^{-1}}\right]$	0.175
Small scale resolution $\kappa_{\max}\eta$	–	2.0
Normalized simulation time T_{end}/T	–	22.0
Number of grid points N^3	–	256^3
Number of particles at each St	–	32,768

the simulation. Table 3.1 summarizes the main fluid statistics.

The evolution equations for small $d/\eta \ll 1$ inertial particles were derived in final form by Maxey & Riley (1983). For large particle to fluid density ratios $\beta \equiv \rho_p/\rho_f \gg 1$ effects of added mass can be neglected. We also neglect the Basset history term and Faxén corrections to Stoke's law. Because of the low mass and low volume fractions, two-way coupling and effects on the continuity equation are neglected, respectively (Elghobashi 2006). The inertial particle evolution equations for position and velocity are,

$$\frac{dX_i}{dt} = v_i \tag{3.2}$$

$$\frac{dv_i}{dt} = \frac{u_i(\mathbf{X}) - v_i}{\tau_p}\,, \tag{3.3}$$

where X_i is the particle position, v_i is the particle velocity and $u_i(\mathbf{X})$ is the fluid velocity evaluated at the particle position. Equations 3.2 and 3.3 are solved numerically using Heun's method (two-stage Runge-Kutta) with use of an in-

tegrating factor. The fluid velocity is interpolated at the particle position by an 8-th order Lagrangian polynomial (Berrut & Trefethen 2004). The following Stokes numbers are simulated: $St = 0.025,\ 0.05,\ 0.1,\ 0.2,\ 0.5,\ 1,\ 2$.

In order to isolate the effects of filtering we artificially force inertial particles to follow fluid particle trajectories. This is accomplished by evolving the inertial particles according to,

$$\frac{dX_i}{dt} = u_i \tag{3.4}$$

$$\frac{dv_i}{dt} = \frac{u_i(\mathbf{X}) - v_i}{\tau_p}\,. \tag{3.5}$$

In this way any effects due to biased sampling are removed while those of filtering are retained. The effect of biased sampling can be isolated by computing fluid statistics along inertial particle trajectories.

Along each particle track (inertial or fluid) the full velocity gradient tensor is computed and stored in addition to position and velocity vectors at an interval of approximately $0.1\tau_\eta$. The data is periodically stored and the Lagrangian tracks are assembled *a posteriori*.

3.3 Results and discussion

3.3.1 The role of biased sampling and filtering on the acceleration PDF

We begin by comparing our single component square-root acceleration variance results to those of Bec et al. (2006) in Figure 3.2, where $\langle a^2 \rangle = \langle a_i a_i \rangle / 3$. Owing

to the difference in R_λ, the results are scaled by the fluid acceleration variance $a_0\langle\varepsilon^3/\nu\rangle^{1/4}$, where the constant a_0 was calculated from the empirical relationship provided by Ishihara et al. (2007). We have emphasized the low St range in this plot by using a logarithmic axis for that coordinate. Also shown is the model for acceleration variance presented in Zaichik & Alipchenkov (2008). The results we obtain are in excellent agreement to those of Bec et al. (2006). We also see that the model of Zaichik & Alipchenkov (2008) represents well the filtering effect that it is intended to replicate. Particle inertia has a significant effect on acceleration variance, even at Stokes numbers as low as 0.1. The results show that for $St \leq 0.2$ the effect of inertia on the acceleration variance is captured by the effect of biased sampling. As St increases beyond 2 it is filtering that captures the effect of inertia. In the intermediate range $0.2 \lesssim St \lesssim 2$ neither biased sampling nor filtering completely captures the inertial particle acceleration variance accurately. Theory presented in Chun et al. (2005) showed that the effect of biased sampling at low St is of $O(St)$, whereas the simple toy model given in Equation 3.1 shows that the leading term due to filtering is expected to scale as $O(St^2)$, in agreement with our observations.

Contributions to acceleration variance come predominantly from the central part of the PDF. Our interest is now turned to the tails of the PDF, which contribute significantly to higher order moments. Figure 3.3 shows details of the tail of the PDF for increasing St as a function of biased sampling and filtering. At $St = 0.025$ there is already a measurable discrepancy between the PDF of fluid particles and inertial particles at $O(1e^{-6})$. At this low Stokes number the PDF that captures the filtering effect is indistinguishable from the fluid PDF as is the PDF from biased sampling with respect to that of the inertial particle. However, at $St = 0.2$ we see that the PDF representing the effect of biased sampling alone

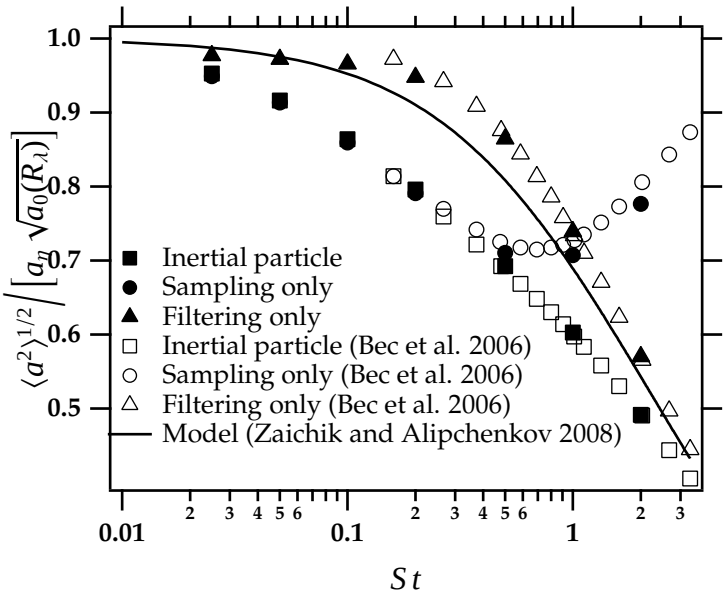

Figure 3.2: Square root of acceleration variance normalized by the square root of the fluid acceleration variance as a function of Stokes number.

is not coincident with the inertial particle PDF deep in the tails, in agreement with the vortex model of Ayyalasomayajula et al. (2008). As St increases further, we see the sampling-only PDF approaches that of the fluid particle, while filtering-only PDF approaches the inertial particle PDF. It is interesting to note that the PDF of biased sampling appears to be more intermittent than that of the fluid at $St = 2$. Higher-order moments of single acceleration components are plotted in Figure 3.4. As the order increases the effect of biased filtering becomes important at ever lower St, as can be seen by the departure of the curve for biased sampling from the inertial particle curve.

With the objective of testing the hypothesis put forth in Ayyalasomayajula et al. (2008), in Figure 3.5 we plot the single component acceleration autocorrelation function of fluid particles sampled along inertial particle trajectories

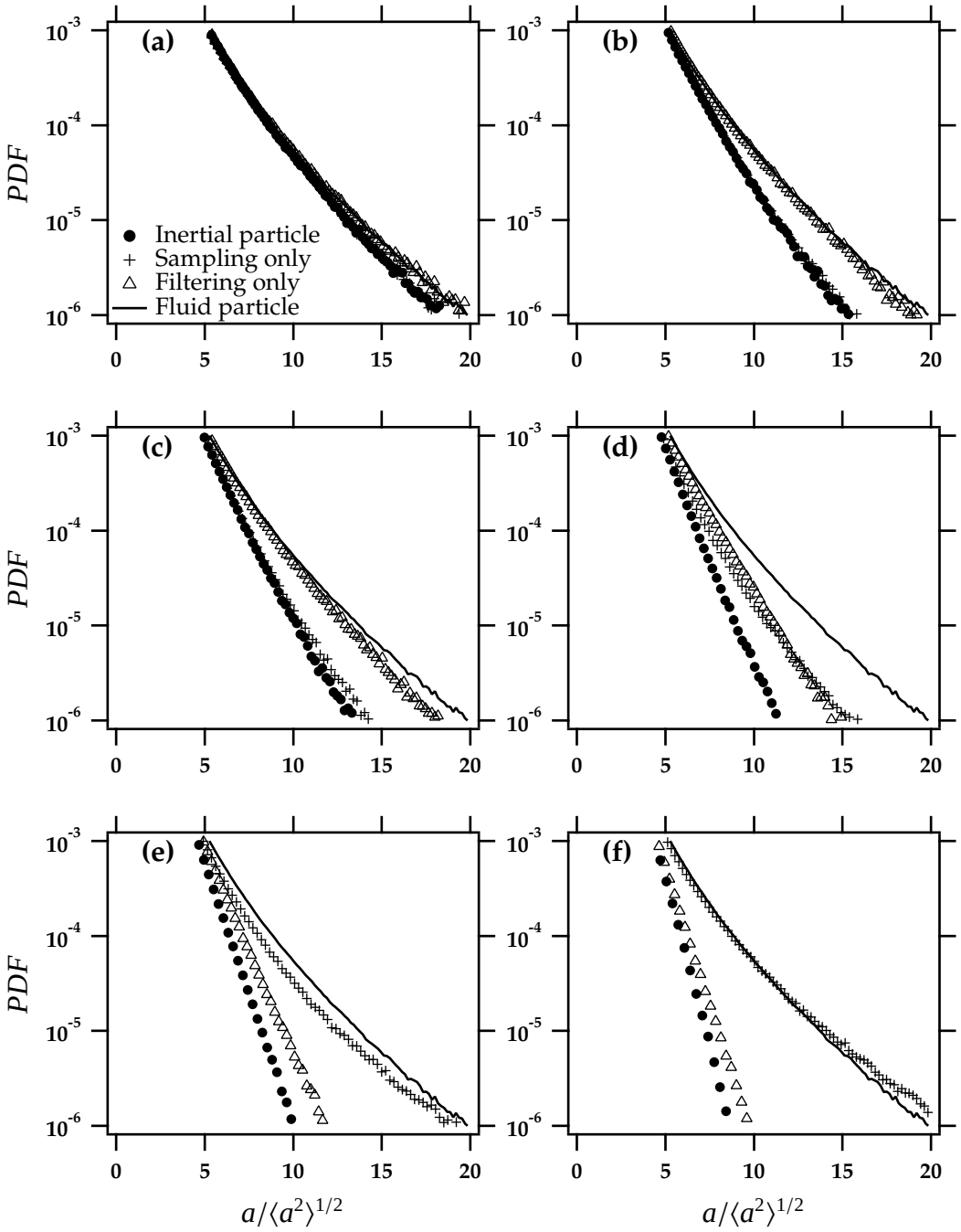

Figure 3.3: Effects of filtering and biased sampling on the acceleration PDF for (a) St=0.025, (b) St=0.1, (c) St=0.2, (d) St=0.5, (e) St=1.0, and (f) St=2.0.

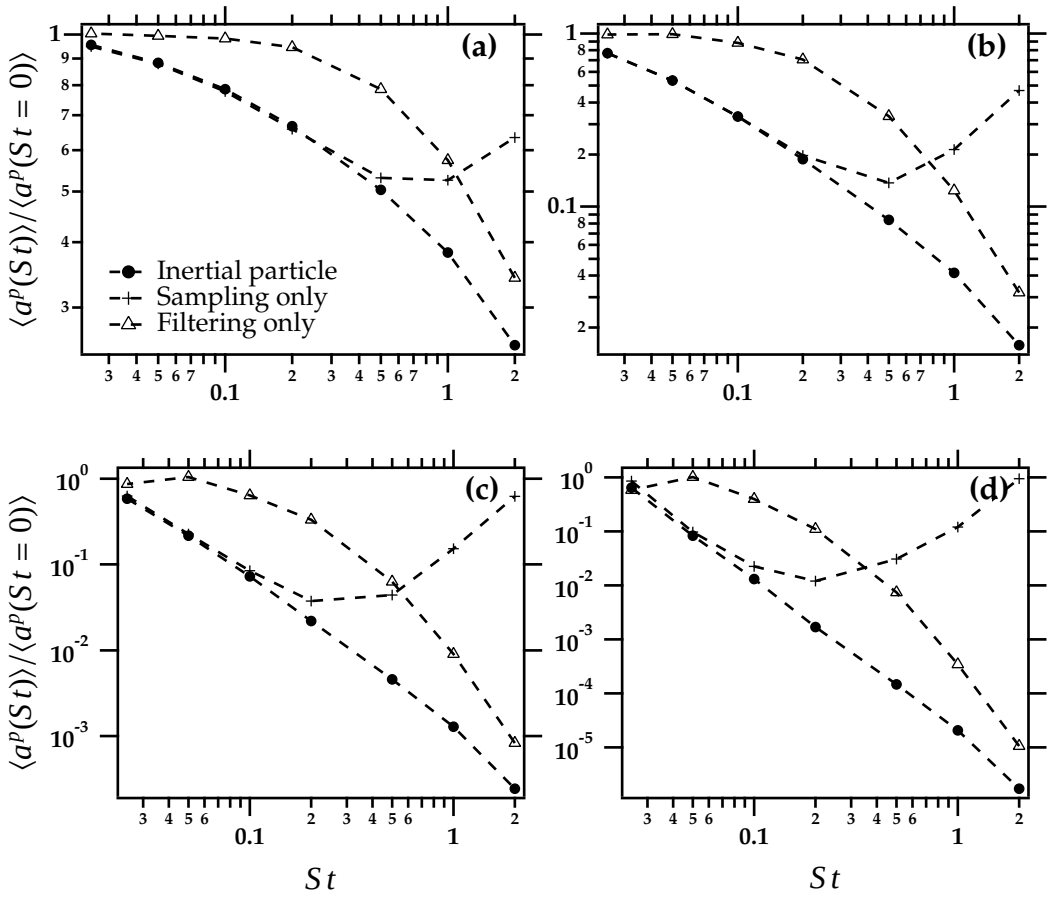

Figure 3.4: Effects of filtering and biased sampling on the ratio $\langle a^p(St)\rangle/\langle a^p(St=0)\rangle$ for (a) $p = 2$, (b) $p = 4$, (c) $p = 6$, and (d) $p = 8$.

conditioned on the magnitude of the acceleration, given by

$$\rho_{a|N} = \left.\frac{\langle a(t)a(t+\Delta t)\rangle}{N\langle a^2\rangle}\right|_{a^2(t)\geq N\langle a^2\rangle}, \tag{3.6}$$

where N is an non-negative integer. It is evident from this figure that the correlation times t_0, herein defined as the first zero-crossing of the curves (Tennekes & Lumley 1972, Yeung & Pope 1989), are a decreasing function of acceleration magnitude. Figure 3.5 shows the case for $St = 0.2$, however the same trends are verified within the entire range of Stokes numbers of this study. Although in qualitative agreement with the vortex model, the reduction in correlation times

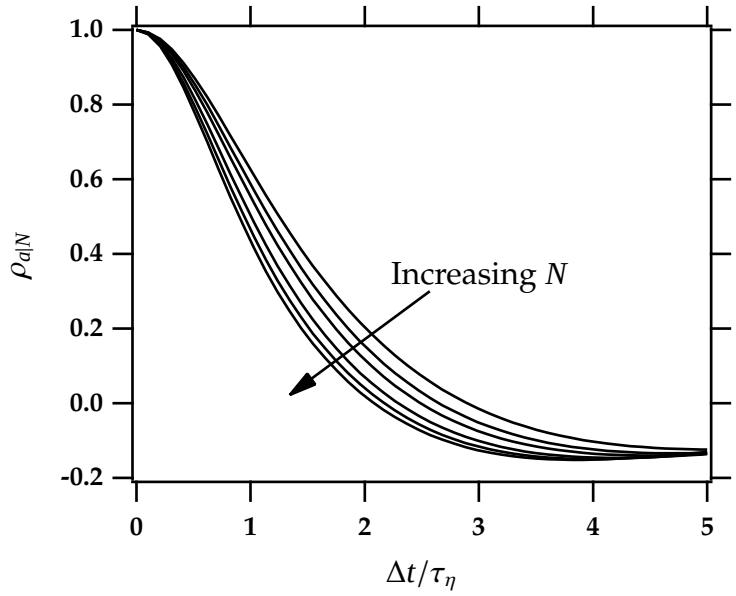

Figure 3.5: Single component acceleration autocorrelation function of fluid particles sampled along inertial particle trajectories (sampling-only) for $St = 0.2$ and $N = 0, 2, 4, 5, 6, 8$.

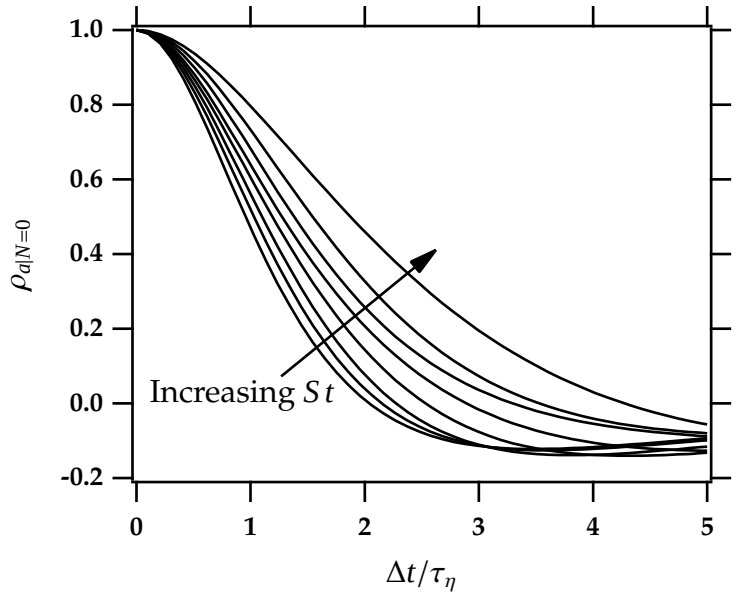

Figure 3.6: Inertial particle single component conditional acceleration autocorrelation function ($N = 0$) for $St = 0, 0.025, 0.05, 0.1, 0.2, 0.5, 1, 2$.

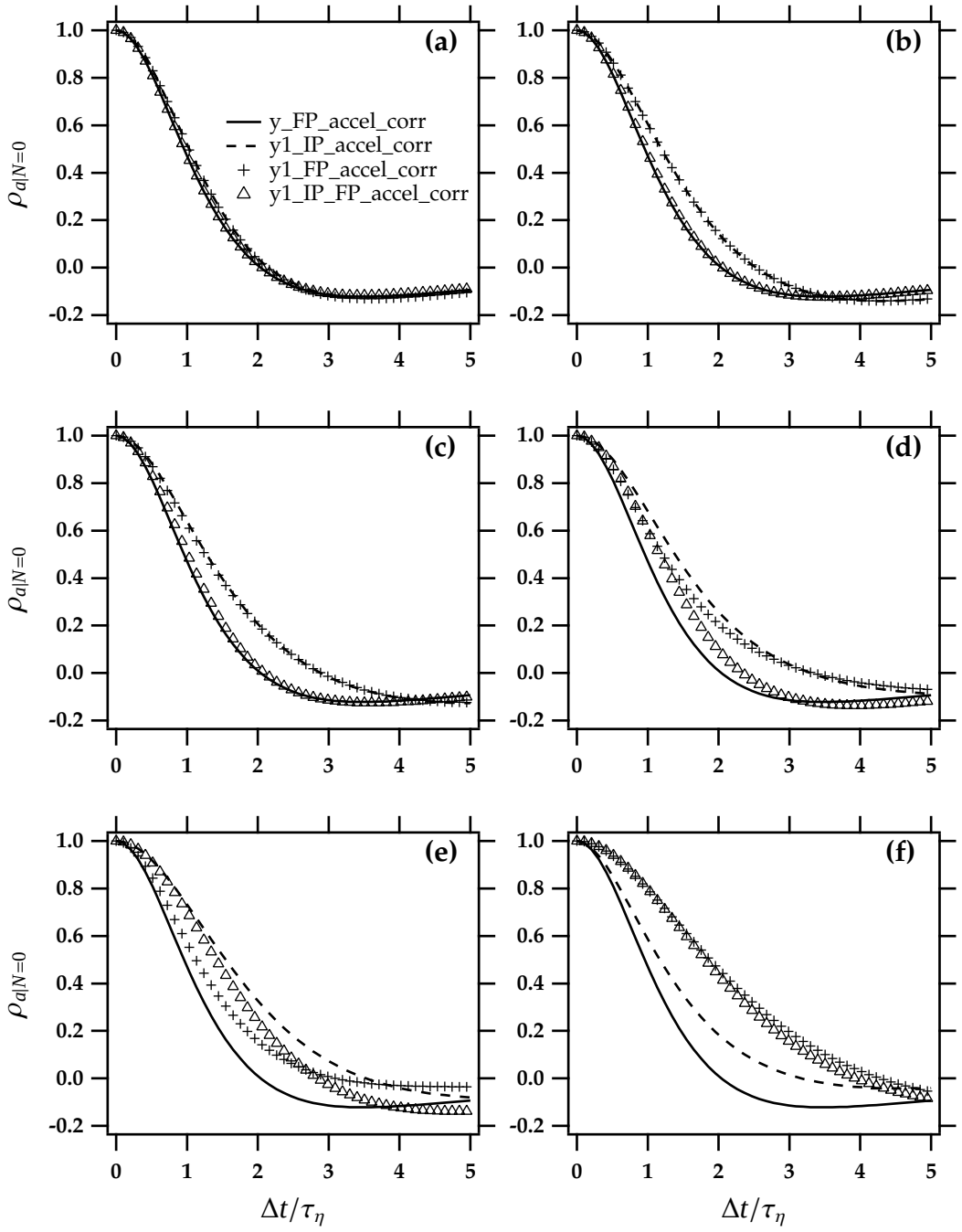

Figure 3.7: Effects of filtering and biased sampling on the acceleration autocorrelation function for (a) $St = 0.025$, (b) $St = 0.1$, (c) $St = 0.2$, (d) $St = 0.5$, (e) $St = 1$, and (f) $St = 2$.

seen here is less dramatic (see Figure 7 in Ayyalasomayajula et al. (2008)). This exaggeration of the filtering effect in the model enhances the discrepancies in the tails of the PDF. Nonetheless, biased filtering does occur and it is important in determining the shape of the normalized acceleration PDF. The acceleration autocorrelation function for inertial particles is shown in Figure 3.6. As expected, with increasing inertia the correlation times increase, since the the particles are progressively less responsive to changes in the acceleration vector. The recent study by Jung et al. (2008) has examined the behavior of the inertial particle acceleration correlation functions over a wide range of Stokes numbers. In Figure 3.7 we show the effects of biased sampling and filtering on the acceleration autocorrelation function. Much like the case of the acceleration variance (Figure 3.3), the biased sampling effect accounts well for the behavior in the acceleration autocorrelation of inertial particles up to $St \approx 0.2$. Only beyond $St = 2$ does the filtering effect closely emulate the inertial particle acceleration autocorrelation curve. This reinforces the need for models that are capable of accounting for the effect of biased sampling, especially at low St, such as the vortex model of Ayyalasomayajula et al. (2008). In addition, theory presented in Chun et al. (2005) and rederived in the appendix for convenience, is capable of obtaining inertial particle statistics in the limit $St \to 0$ with knowledge of only fluid particle trajectories. This theory can be applied to models for fluid particles.

3.3.2 Acceleration and flow topology

There is clear evidence of the important role that biased sampling has on the acceleration statistics of inertial particles, particularly in the limit of small Stokes

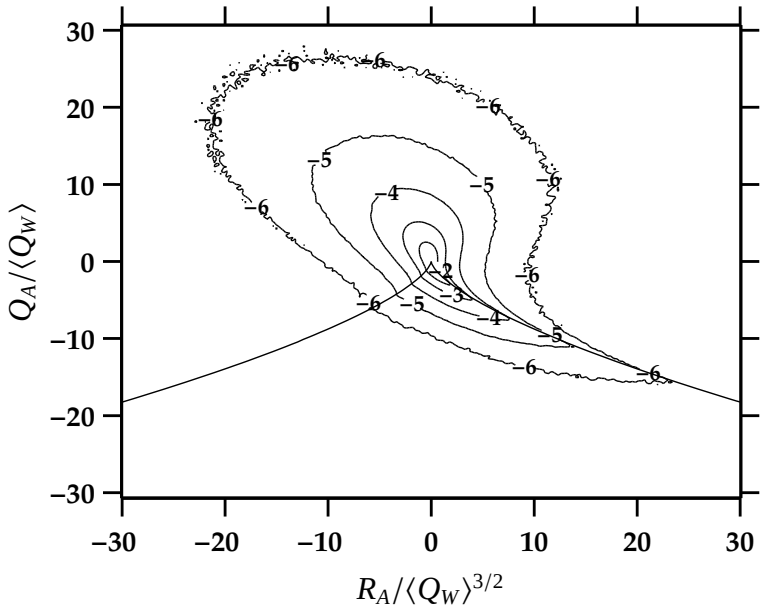

Figure 3.8: Joint PDF of invariants (R_A, Q_A) for fluid particles. The exponents of the decade are indicated on the contour lines.

numbers. However, it is not clear what aspects of the underlying flow are controlling the particle acceleration statistics. We attempt to uncover this connection by studying the relationship between flow topology and inertial particle accelerations.

Flow topology can be characterized by invariant plots of the velocity-gradient tensor $A_{ij} = \partial u_i/\partial x_j$, the symmetric strain-rate tensor $S_{ij} = 1/2\left(A_{ij} + A_{ji}\right)$ and the anti-symmetric deviatoric rotation-rate tensor $W_{ij} = 1/2\left(A_{ij} - A_{ji}\right)$, where by definition $A_{ij} = S_{ij} + W_{ij}$. Detailed information on the subject can be found in previous work (Cantwell 1992, 1993, Chong et al. 1990, da Silva & Pereira 2008, Ooi et al. 1999, Soria et al. 1994). Each of these tensors satisfies a characteristic polynomial of the form,

$$\lambda_i^3 + P\lambda_i^2 + Q\lambda_i + R = 0\,, \tag{3.7}$$

where λ_i are the eigenvalues and P, Q and R are the first, second and third tensor

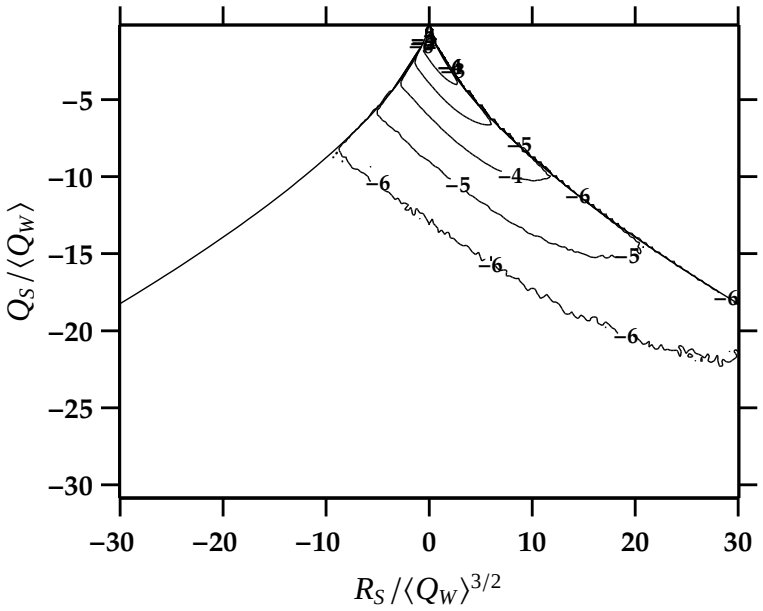

Figure 3.9: Joint PDF of invariants (R_S, Q_S) for fluid particles. The exponents of the decade are indicated on the contour lines.

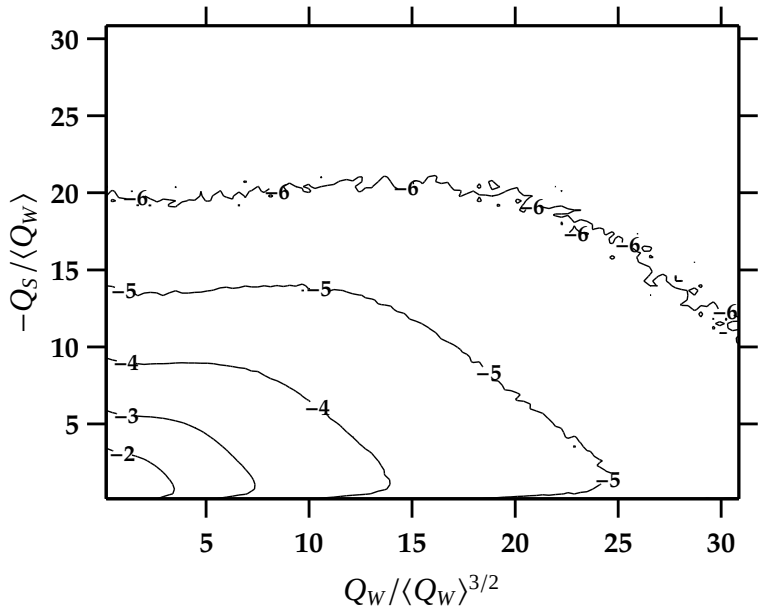

Figure 3.10: Joint PDF of invariants $(Q_W, -Q_S)$ for fluid particles. The exponents of the decade are indicated on the contour lines.

invariants respectively. For incompressible flows $P = A_{ii} = S_{ii} = 0$. The other invariants are given by,

$$Q_A = -\frac{1}{2}A_{ij}A_{ji} = -\frac{1}{2}\left(S_{ij}S_{ij} - W_{ij}W_{ij}\right) , \tag{3.8}$$

$$R_A = -\frac{1}{3}A_{ij}A_{jk}A_{ki} = -\frac{1}{3}\left(S_{ij}S_{jk}S_{ki} + 3W_{ij}W_{jk}S_{ki}\right) . \tag{3.9}$$

The invariants Q_S and R_S are obtained by setting the W_{ij} terms to zero in Equations 3.8 and 3.9,

$$Q_S = -\frac{1}{2}S_{ij}S_{ij} = -\frac{1}{2}S^2 \tag{3.10}$$

$$R_S = -\frac{1}{3}S_{ij}S_{jk}S_{ki} , \tag{3.11}$$

and the only non-zero invariant of W_{ij} is given by setting the S_{ij} terms to zero in Equation 3.8,

$$Q_W = \frac{1}{2}W_{ij}W_{ij} = -\frac{1}{2}W^2 . \tag{3.12}$$

The physical interpretation of these tensor invariants and classification of flows based on their values is described in the aforementioned literature. Here we will give a succinct overview of the main observations. The invariant Q_S is related to the turbulent kinetic energy dissipation rate by viscosity through $\varepsilon = -4\nu Q_S$. Hence regions of the flow with intense dissipation will have high values of $|Q_S|$. The invariant Q_W is essentially enstrophy $\omega^2 = \omega_i\omega_i$, as one can write $Q_W = 1/4\omega_i\omega_i$, where $\omega_i = \epsilon_{ijk}\partial u_k/\partial u_j$ is vorticity and ϵ_{ijk} is the Levi-Civita permutation symbol. Regions with high values of Q_W have been identified with tube-like structures (Jimenez et al. 1993, Kaneda & Ishihara 2006, She et al. 1991, Siggia 1981, Toschi & Bodenschatz 2009, Vincent & Meneguzzi 1991) while regions of high $|Q_S|$ tend to be identified with sheet-like or ribbon structures (Kaneda & Ishihara 2006, Moisy & Jimenez 2004). The invariant R_S appears as a source/sink term in the evolution equation for the rate-of-strain $S^2 = S_{ij}S_{ij}$

(Davidson 2004, Ooi et al. 1999). If we denote the eigenvalues of the strain-rate tensor by α_S, β_S, and γ_S then $R_S = -1/3\left(\alpha_S^3 + \beta_S^3 + \gamma_S^3\right) = -\alpha_S\beta_S\gamma_S$. Furthermore, continuity requires that $\alpha_S + \beta_S + \gamma_S = 0$. If we order the eigenvalues such that $\alpha_S \geq \beta_S \geq \gamma_S$, this means that for $R_S > 0$ (strain production), α_S, $\beta_S > 0$ and $\gamma_S < 0$. So there is extension along two axes and a large compression along one axis, resembling a sheet-like structure (Batchelor 1953). If $R_S < 0$, then $\alpha_S > 0$ and β_S, $\gamma_S < 0$ and the resulting structure is tube-like (Batchelor 1953). The interpretation of Q_A and R_A is dependent on the sign of each. Strain-dominated regions correspond to $Q_A < 0$, whereas rotation dominates for $Q_A > 0$. In Equation 3.9 the term $3W_{ij}W_{jk}S_{ki}$ can be written as $3/4\omega_i\omega_j S_{ij}$ and represents the vortex stretching term in the evolution equation for enstrophy. If $Q_A \gg 0$, then $R_A \sim -1/4\omega_i\omega_j S_{ij}$ and $R_A < 0$ is associated with vortex stretching (enstrophy production) while $R_A > 0$ is associated with vortex compression (enstrophy destruction). On the other hand, if $Q_A \ll 0$, then $R_A \sim -1/3 S_{ij}S_{jk}S_{ki} = -\alpha_S\beta_S\gamma_S$. In this scenario, $R_A > 0$ is associated with biaxial strain whereas $R_A < 0$ is identified with uni-axial strain. For homogeneous turbulence it can be shown that $\langle R_A \rangle = \langle Q_A \rangle = 0$, which implies $1/4\langle\omega_i\omega_j S_{ij}\rangle = -\langle\alpha_s\beta_s\gamma_s\rangle$ (Betchov 1956, Townsend 1951). The mean rate of enstrophy generation by vortex-stretching is expressed as the average product of the strain-rate tensor eigenvalues. Experimental and numerical evidence has shown that the mean enstrophy generation in turbulence is a positive quantity (Gotoh et al. 2002, Kerr 1985, Sreenivasan & Antonia 1997, Taylor 1938, Tsinober et al. 1992), therefore there is a preference for situations where $\alpha_S\gamma_S\beta_S < 0$, associated with conditions of biaxial strain.

The invariants are commonly presented in the form of joint PDFs. Figures 3.8 through 3.10 show the joint PDFs of (R_A, Q_A), (R_S, Q_S) and $(Q_W, -Q_S)$ for fluid particles computed from our DNS, respectively. The tear-drop or pear shape of

the (R_A, Q_A) joint PDF is common to variety of turbulent flows such as isotropic turbulence (Ooi et al. 1999), plane mixing layers (Soria et al. 1994), channel flows (Blackburn et al. 1996), boundary layer flows (Chacin & Cantwell 2000, Chacin et al. 1996), separated boundary layer flows (Chong et al. 1998), plane jets (da Silva & Pereira 2008) and the atmospheric surface layer (Gulitski et al. 2007). The tent-like lines in Figures 3.8 and 3.9 are the solutions to $D_A = 0$ and $D_S = 0$, where D_A and D_S are the discriminants of A_{ij} and S_{ij} respectively. These are given by,

$$D_A = \frac{27}{4} R_A^2 + Q_A^3 \,, \tag{3.13}$$

$$D_S = \frac{27}{4} R_S^2 + Q_S^3 \,. \tag{3.14}$$

For $D_A > 0$ there will be two complex-conjugate eigenvalues and one real eigenvalue. For $D_A \leq 0$ there are three real eigenvalues. From Figure 3.8 we can infer that (i) small velocity gradients are more likely, (ii) there is a strong correlation between $Q_A < 0$ and $R_A > 0$ (sheet-like structures) along the line $D_A = 0$ and (iii) for $D_A > 0$, values of $Q_A > 0$ are correlated with $R_A < 0$ (tube-like structures). Because S_{ij} is real and symmetric, $D_S \leq 0$ and all points in Figure 3.9 lie below or at the $D_S = 0$ line. The probability of events where $R_S > 0$ (expansion) is larger than those where $R_S < 0$ (contraction), indicating the prevalence of biaxial strain. By defining the ratio $a = \beta_S / \alpha_S$, R_S can be written as (Blackburn et al. 1996),

$$R_S = (-Q_S)^{3/2} \, a \, (1 + a) \left(1 + a + a^2\right)^{-3/2} \,. \tag{3.15}$$

The positive branch of the $D_S = 0$ curve is a limiting case that corresponds to $a = 1$ (axisymmetric expansion). The negative branch is obtained by setting $a = -1/2$ (axisymmetric contraction). The case $a = 0$ corresponds to two-dimensional flow. It is found that the most probable strain rate configuration in

Table 3.2: Classification of the (R, Q) invariant plane. $Q_A^\star = -3(R_A^2/4)^{2/3}$. See Davidson (2004) for more details.

	$R_A > 0$	$R_A < 0$
$Q_A > Q_A^\star$	vortex compression $\omega_i\omega_j S_{ij} < 0$	vortex stretching $\omega_i\omega_j S_{ij} > 0$
$Q_A < Q_A^\star$	biaxial strain $\alpha_S\beta_S\gamma_S < 0$	uni-axial strain $\alpha_S\beta_S\gamma_S > 0$

Table 3.3: Classification of the $(Q_W, -Q_S)$ invariant plane. $\downarrow\downarrow$ represents small values whereas $\uparrow\uparrow$ represents large values.

	$\downarrow\downarrow Q_W$	$\uparrow\uparrow Q_W$
$\downarrow\downarrow \lvert Q_S\rvert$	small velocity gradients large-scale structures	intense rotation tube-like structures
$\uparrow\uparrow \lvert Q_S\rvert$	irrotational dissipation ribbon-like structures	vortex sheets intense strain and rotation

many turbulent flows is well approximated by $\alpha_S : \beta_S : \gamma_S = 3 : 1 : -4$ (biaxial strain), where $a = 1/3$ (Ashurst et al. 1987, Kerr 1987, Tsinober et al. 1992). In our simulation we find $\langle\alpha_S\rangle/\langle S^2\rangle^{1/2} : \langle\beta_S\rangle/\langle S^2\rangle^{1/2} : \langle\gamma_S\rangle/\langle S^2\rangle^{1/2} = 0.54 : 0.13 : -0.67$ with $\langle a\rangle = 0.24$. This result is close to that found in experiments (Lüthi et al. 2005) and simulations (Girimaji & Pope 1990, Goto & Kida 2003). Our attention now turns to Figure 3.10. The region of low Q_W and high $-Q_S$ is of intense dissipation and approximately irrotational. On the other hand, regions of high Q_W and low $-Q_S$ resemble solid body rotation. High values of $-Q_S$ and Q_W are associated with vortex sheets, as found in studies of mixing layers (Soria et al. 1994). The PDF in Figure 3.10 shows asymmetry towards high values of Q_W, indicating that at a given point in the flow, the local value of Q_W tends to be larger than the value of $-Q_S$. Tables 3.2 and 3.3 present a rudimentary classification of the different regions on the (R, Q) and $(Q_W, -Q_S)$ invariant planes, respectively.

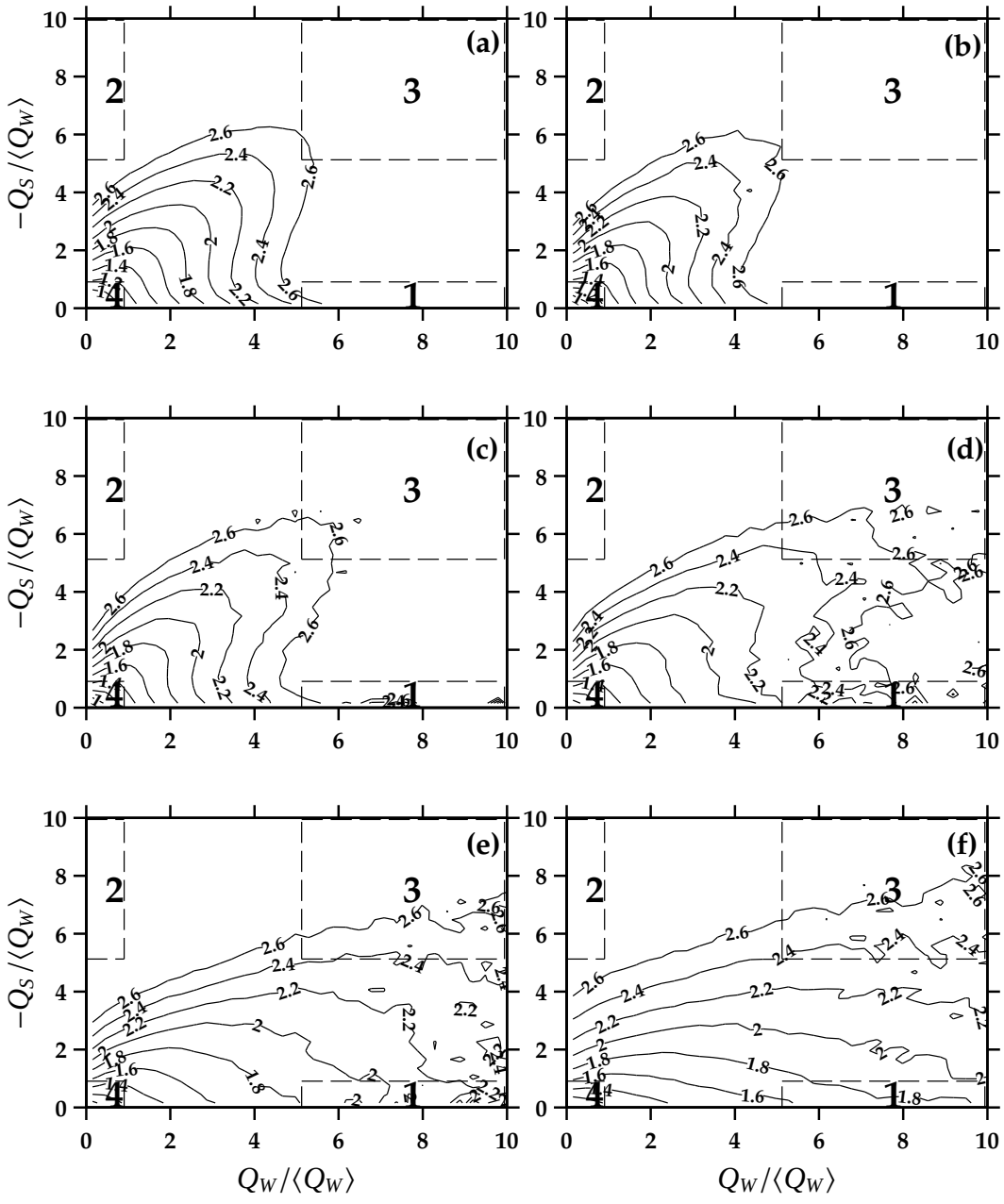

Figure 3.11: Acceleration contour plots $|a|/a_{\mathrm{rms}}(St)$ on the $(Q_W, -Q_S)$ invariant plane for (a) $St = 0.025$, (b) $St = 0.1$, (c) $St = 0.2$, (d) $St = 0.5$, (e) $St = 1$, and (f) $St = 2$. The areas outlied by dashed lines correspond to 1 - high Q_W and low Q_S, 2 - high Q_S and low Q_W, 3 - high Q_W and high Q_S, and 4 - low Q_W and low Q_S. The values for the ratio $|a|/a_{\mathrm{rms}}(St)$ are indicated on the contour lines.

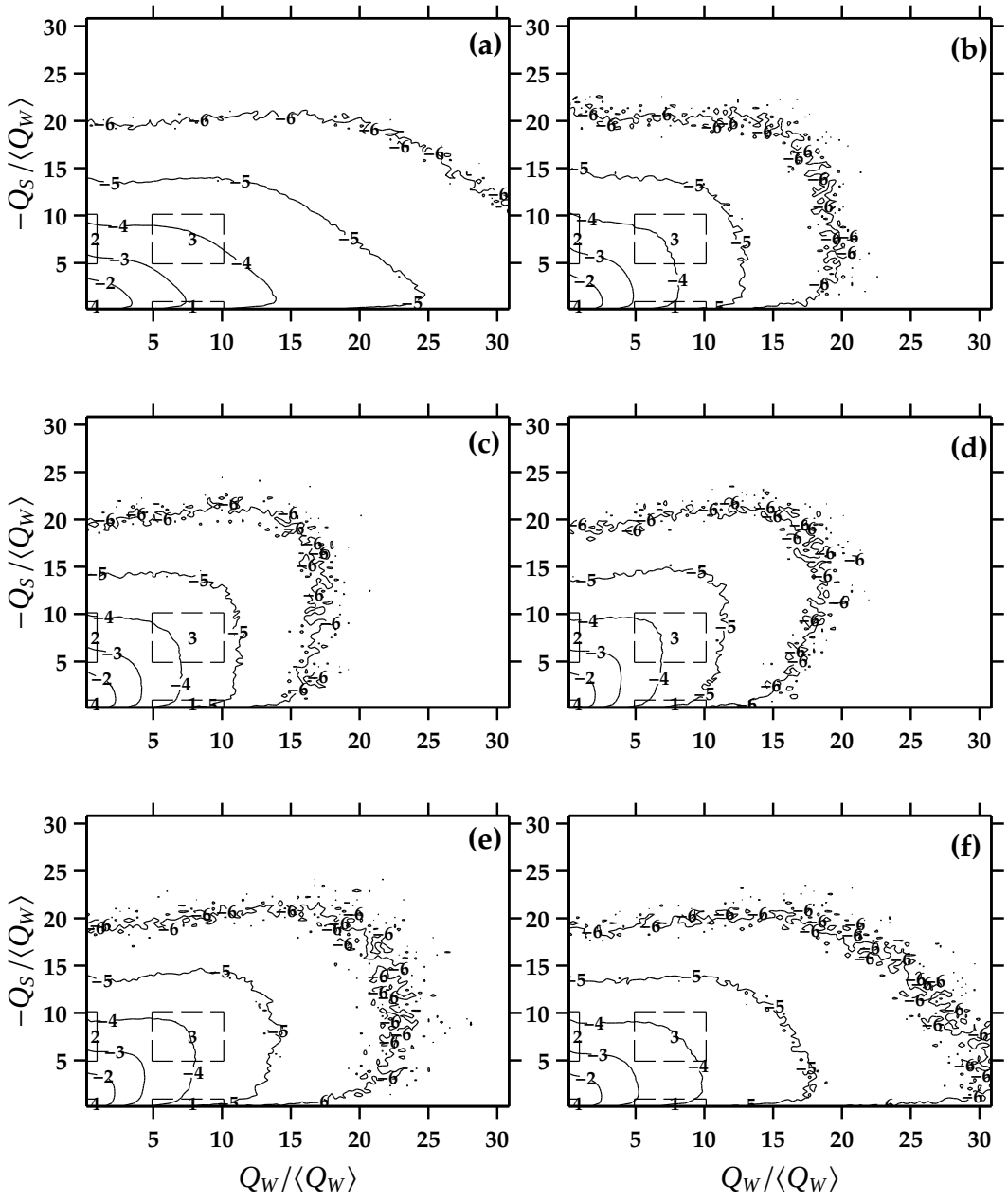

Figure 3.12: Joint PDF of the invariant pair $(Q_W, -Q_S)$ for (a) $St = 0.025$, (b) $St = 0.1$, (c) $St = 0.2$, (d) $St = 0.5$, (e) $St = 1$, and (f) $St = 2$. The areas outlied by dashed lines correspond to 1 - high Q_W and low Q_S, 2 - high Q_S and low Q_W, 3 - high Q_W and high Q_S, and 4 - low Q_W and low Q_S. The exponents of the decade are indicated on the contour lines.

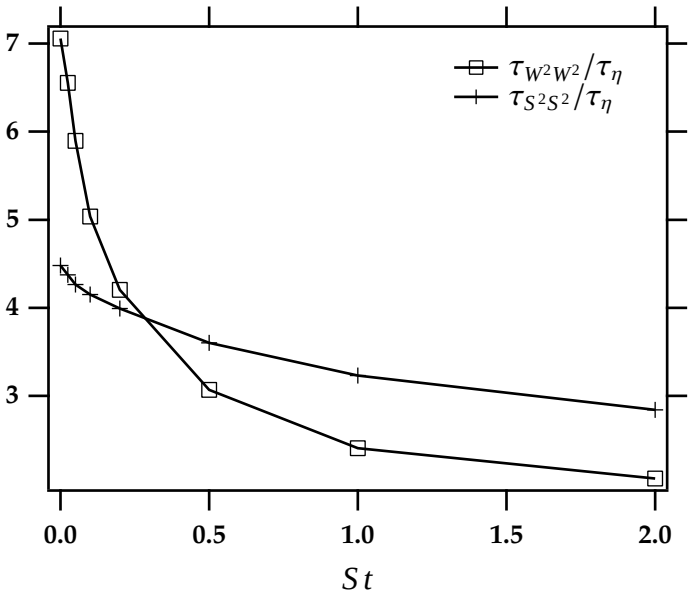

Figure 3.13: Correlation times of the rotation rate and strain rate as a function of Stokes number.

Acceleration contour plots

In order to understand how inertial particle acceleration relates to flow topology, in particular the acceleration magnitude and its higher order moments, we associate a given acceleration event to a position in the $(Q_W, -Q_S)$ plane. This procedure leads to the acceleration magnitude contour plots shown in Figure 3.11. The main effect of inertia is to stretch the isocontours of acceleration magnitude towards larger values of Q_W. This effect becomes quite significant for $St > 0.2$. With increasing St, in the limit of $Q_S \rightarrow 0$, a given value of $|a|$ is attained at a much larger value of Q_W than would be required for Q_S in the limit of $Q_W \rightarrow 0$. This trend is consistent with the notion that high-inertia particles are less susceptible to vortex trapping. We also observe a region in the $(Q_W, -Q_S)$ plane where the acceleration magnitude is approximately independent of Q_W. We reason that a possible cause for this is that as the particle inertia

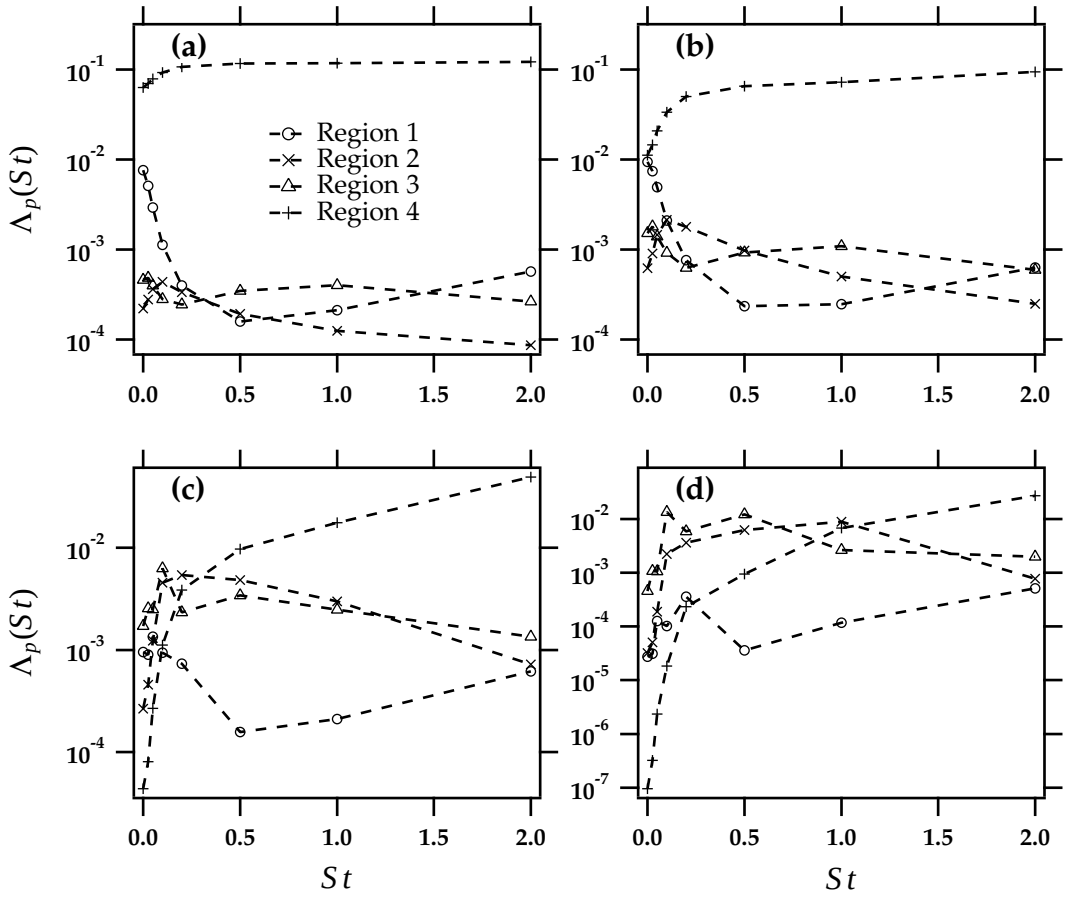

Figure 3.14: Contribution of the regions outlined in the $(Q_W, -Q_S)$ plane of Figures 3.11 and 3.12 to higher-order acceleration moments for (a) $p = 2$, (b) $p = 4$, (c) $p = 6$, and (d) $p = 8$.

increases, the persistence of strain as seen by the inertial particle becomes larger than that of rotation, allowing the inertial particle more time to be influenced by strain than by rotation, therefore the observed behavior. In order to verify the assumption about the persistence of strain and rotation, we calculate the normalized Lagrangian autocorrelation function and the resulting correlation

time,

$$\rho_{XY}(t) = \frac{\langle [X(0) - \langle X \rangle] [Y(t) - \langle Y \rangle] \rangle}{\sigma_X \sigma_Y} , \tag{3.16}$$

$$\tau_{XY} = \int_0^\infty \rho_{XY}(t) dt , \tag{3.17}$$

where ρ_{XY} is the autocorrelation function of X and Y, τ_{XY} is the correlation time and σ_X and σ_Y are the standard deviations of X and Y respectively. Figure 3.13 shows $\tau_{W^2W^2}$ and $\tau_{S^2S^2}$ as a function of Stokes number. It is seen that for fluid particles $\tau_{W^2W^2}$ is larger, however at $St \approx 0.3$ the trend is reversed and $\tau_{S^2S^2}$ becomes larger. So it seems that the primary effect of increasing inertia on acceleration is to diminish significantly the effect of rotation. We note that $S^2 = -2Q_S$ and $W^2 = 2Q_W$.

Although the acceleration contour plots provide an interesting view of how acceleration relates to flow topology, they must be viewed in conjunction with the $(Q_W, -Q_S)$ joint PDFs shown in Figure 3.12. A certain value of $(Q_W, -Q_S)$ may be associated with a large acceleration event, however the probability of that event may be very low, such that the overall contribution to the variance and higher-order moments is not significant. The converse is also true. We see from Figure 3.12 that increasing inertia leads to a reduction in the asymmetry of the PDF. This effect peaks at $St \approx 0.5$ and then the asymmetry increases at larger St. This trend more or less coincides with the peak in particle clustering (Reade & Collins 2000, Sundaram & Collins 1997) and is consistent with the ejection of low St particles from regions of large Q_W. In Figures 3.11 and 3.12 we have identified four regions, where each corresponds to a particular flow topology. We assess the contribution of each of these regions to acceleration variance and

higher-order moments through the following expression

$$\Lambda_p = \frac{\langle [a_i a_i]^p \left| Q_W^U \le Q_W \le Q_W^L,\ -Q_S^L \le -Q_S \le -Q_S^U \right\rangle}{\langle [a_i a_i]^p \rangle} = \frac{\int_{Q_W^L}^{Q_W^U} \int_{-Q_S^L}^{-Q_S^H} g_p(Q_W, -Q_S) f(Q_W, -Q_S) dQ_W(-dQ_S)}{\int_0^\infty \int_0^\infty g_p(Q_W, -Q_S) f(Q_W, -Q_S) dQ_W(-dQ_S)}, \tag{3.18}$$

where $g_p(Q_W, -Q_S)$ is the value of $[a_i a_i]^p$ evaluated at $(Q_W, -Q_S)$, $f(Q_W, -Q_S)$ is the joint PDF, Q_W^U, Q_W^L, $-Q_S^U$, $-Q_S^L$ delimitate the lower (L) and upper bounds (U) of the region of interest in the $(Q_W, -Q_S)$ plane and p is a non-negative integer. The computed values for Λ_p are shown in Figure 3.14. We see that the region labeled as "1" corresponds to high Q_W and low $-Q_S$ events, which resemble solid body rotation. For fluid particles ($St = 0$) this region dominates over the region labeled as "2", of low Q_W and high $-Q_S$, associated with intense dissipation events. However, as St increases, region "1" contributes less towards $\langle \left[a_i a_i^p \right] \rangle$, attaining a minimum at $0.5 \le St \le 1$, coinciding with the peak in clustering at $St \approx 0.7$ (Reade & Collins 2000, Sundaram & Collins 1997). The region labeled as "4", of low Q_W and low $-Q_S$, dominates for moments $p \le 2$ at all St. Note that this is also the region with the smallest area in the $(Q_W, -Q_S)$ plane. For $p > 2$ and low St this region contributes less to the total moment than the other regions. The contribution of region "3", of high Q_W and high $-Q_S$ exhibits less St dependence than other regions and is more or less of similar magnitude for all values of p. Region "2" shows a peak at low St. We believe this is related to the accumulation of these particles in regions of high strain and low rotation, as can be seen in Figure 3.12, combined with the higher acceleration events associated with this region for $0 < St \le 0.5$. The analysis performed here is of a semi-quantitative nature, in that other regions could have been chosen and the statistical convergence of the moments $p > 2$ is not as good.

Conditional mean trajectories on the invariant plane

Following the methodology of Ooi et al. (1999) we compute conditional mean trajectories (CMTs) on the invariant planes. These are obtained by calculating the mean rate of change of an invariant pair $\langle DX/Dt \rangle$ and $\langle DY/Dt \rangle$ conditioned on a particular value $(X = X_0, Y = Y_0)$ on the invariant plane, where X and Y form the invariant pair. We have,

$$\left\langle \frac{DX}{Dt} \middle| (X = X_0, Y = Y_0) \right\rangle = \frac{1}{N_{X,Y}} \sum_{X_0-\Delta_X/2}^{X_0+\Delta_X/2} \sum_{Y_0-\Delta_Y/2}^{Y_0+\Delta_Y/2} \frac{X(t+\Delta t) - X(t)}{\Delta t}, \tag{3.19}$$

$$\left\langle \frac{DY}{Dt} \middle| (X = X_0, Y = Y_0) \right\rangle = \frac{1}{N_{X,Y}} \sum_{X_0-\Delta_X/2}^{X_0+\Delta_X/2} \sum_{Y_0-\Delta_Y/2}^{Y_0+\Delta_Y/2} \frac{Y(t+\Delta t) - Y(t)}{\Delta t}, \tag{3.20}$$

where Δ_X is the bin width of X, Δ_Y is the bin width of Y, and $N_{X,Y}$ is the number of samples in the region $X_0-\Delta_X/2 \leq X \leq X_0+\Delta_X/2$ and $Y_0-\Delta_Y/2 \leq Y \leq Y_0+\Delta_Y/2$. The result is a displacement vector for each position on the invariant plane (X, Y). From the vectors we can compute CMTs on the invariant plane. These represent the succession of flow topologies experienced on average by the particles. Figure 3.15 shows CMTs for the $(Q_W, -Q_S)$ plane as a function of St. For all St we observe the existence of a stable focus at $(Q_W/\langle Q_W \rangle, -Q_S/\langle Q_W \rangle) \approx (1, 1)$. This focus moves slightly towards a lower value of Q_W with increasing St, reaching a minimum value of Q_W at $St \approx 0.5$, then increasing towards $Q_W/\langle Q_W \rangle = 1$ at $St = 2$. A CMT beginning from a region of high $-Q_S$ and low Q_W (intense dissipation) moves towards a region of high $-Q_S$ and high Q_W (vortex sheet), then to a region of low $-Q_S$ and high Q_W (vortex tubes), followed by a region of low $-Q_S$ and low Q_W, spiraling towards the focus. We note that with increasing St less time is spent in the regions of low $-Q_S$ and high Q_W. This promotes a rupture in the topological evolution for $St = 2$ particles, allowing for trajectories from regions of high $-Q_S$ and high Q_W towards the focus, avoiding regions that

resemble vortex tubes. Values for the displacement vector of inertial particles on the $(Q_W, -Q_S)$ plane are largest in the regions of intense strain and intense rotation, especially the latter. For fluid particles, large values of of the displacement vector are not common in regions of low Q_W. In general, displacement vectors increase in magnitude with distance from the origin of the $(Q_W, -Q_S)$ plane. The DNS study of Ooi et al. (1999) does not show the stable focus seen here. Furthermore, in the referred study some of the CMTs that move towards regions of high $-Q_S$ and high Q_W do not return the origin. We find no evidence of this behavior, as all our CMTs eventually converge to the focus.

In addition to the $(Q_W, -Q_S)$ invariant plane, we observe some interesting features in the (R_S, Q_S) and the (R, Q) planes. Figure 3.16 shows CMTs on the (R_S, Q_S) plane. The plot for $St = 0$ shows a stable focus situated at $(R_S/\langle Q_W\rangle^{3/2}, Q_S/\langle Q_W\rangle) \approx (0.3, -1.5)$. Because it is located at a positive value of R_S, $\alpha_S\beta_S\gamma_S < 0$ and there is extension along two axes and a large compression along a third axis. As St increases the focus moves along the null-discriminant curve towards larger values of R_S. However, our data is insufficient to fully resolve this focus at higher St. The displacement of the focus is in agreement with the (R_S, Q_S) joint PDF (not shown), which indicates that with increasing St there is a tendency to favor regions of higher Q_S in the $R_S > 0$ region, whereas the opposite occurs within the $R_S < 0$ region (see Figure 3.10). The CMTs begin somewhere along the null-discriminant curve and move towards the focus. Those that originate on the left branch of the null-discriminant curve move towards the $R_S > 0$ region, whereas those that originate on the right branch of the null-discriminant curve tend to remain in the $R_S > 0$ region, but unlike the former CMTs, they initially move towards larger values of Q_S in a spiraling trajectory towards the focus. The study of Ooi et al. (1999) also shows a focus in the

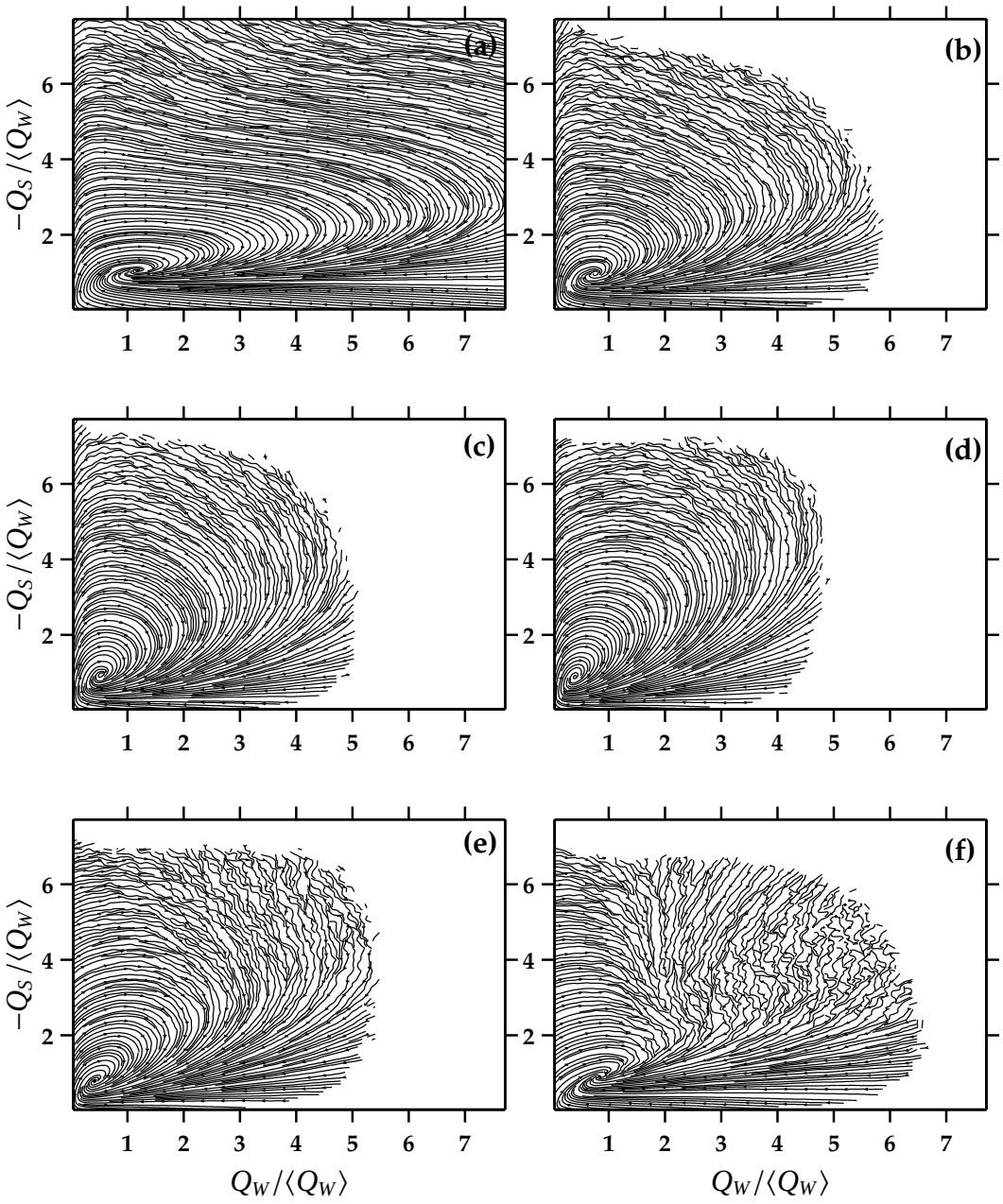

Figure 3.15: Conditional mean trajectories on the $(Q_W, -Q_S)$ invariant plane for (a) $St = 0.025$, (b) $St = 0.1$, (c) $St = 0.2$, (d) $St = 0.5$, (e) $St = 1$, and (f) $St = 2$. Only regions with a number of samples $N_{Q_W,-Q_S} \geq 300$ are shown.

(R_S, Q_S) plane, however one that is unstable. In the aforementioned study CMTs begin at the focus and end at the null-discriminant curve. We see the exact opposite from our data. The recent experimental study of da Silva & Pereira (2008) finds trajectories that resemble the ones presented here. For all St the magnitude of the displacement vectors increase with the distance from the focus.

Figure 3.17 shows the CMTs on the (R_A, Q_A) invariant plane. We immediately recognize the tear-drop shape reported for a variety of turbulent flows. The CMTs evolve in a clockwise spiral towards the origin, with multiple crossings of the null-discriminant curve. As pointed out in Ooi et al. (1999), this suggests that on average particles move from regions dominated by large velocity gradients (small-scales) to regions of small velocity gradients (large-scales). In Figure 3.17 we have not made any restrictions on the number of samples N_{R_A,Q_A} in order to more clearly demonstrate the dependence on St. Perhaps the most interesting trend is that with increasing St the CMTs spiral more rapidly towards the origin. It also seems that with increasing St, particles are less likely to inhabit the region $R_A > 0$ above the null-discriminant curve. Following the classification of Chong et al. (1990), we recall this region represents one which is rotation dominated and of vortex compression. This trend peaks with the maximum in the inertial particle clustering, subsiding at larger St, where the particle relaxation time becomes too large for particles to maintain a significant correlation with the local flow topology (Bec et al. 2006).

Additional finding related to flow topology

Collins & Keswani (2004) studied the R_λ dependence of clustering in the low St limit. They were able to relate clustering to the difference $\langle S^2 - W^2 \rangle$, where the

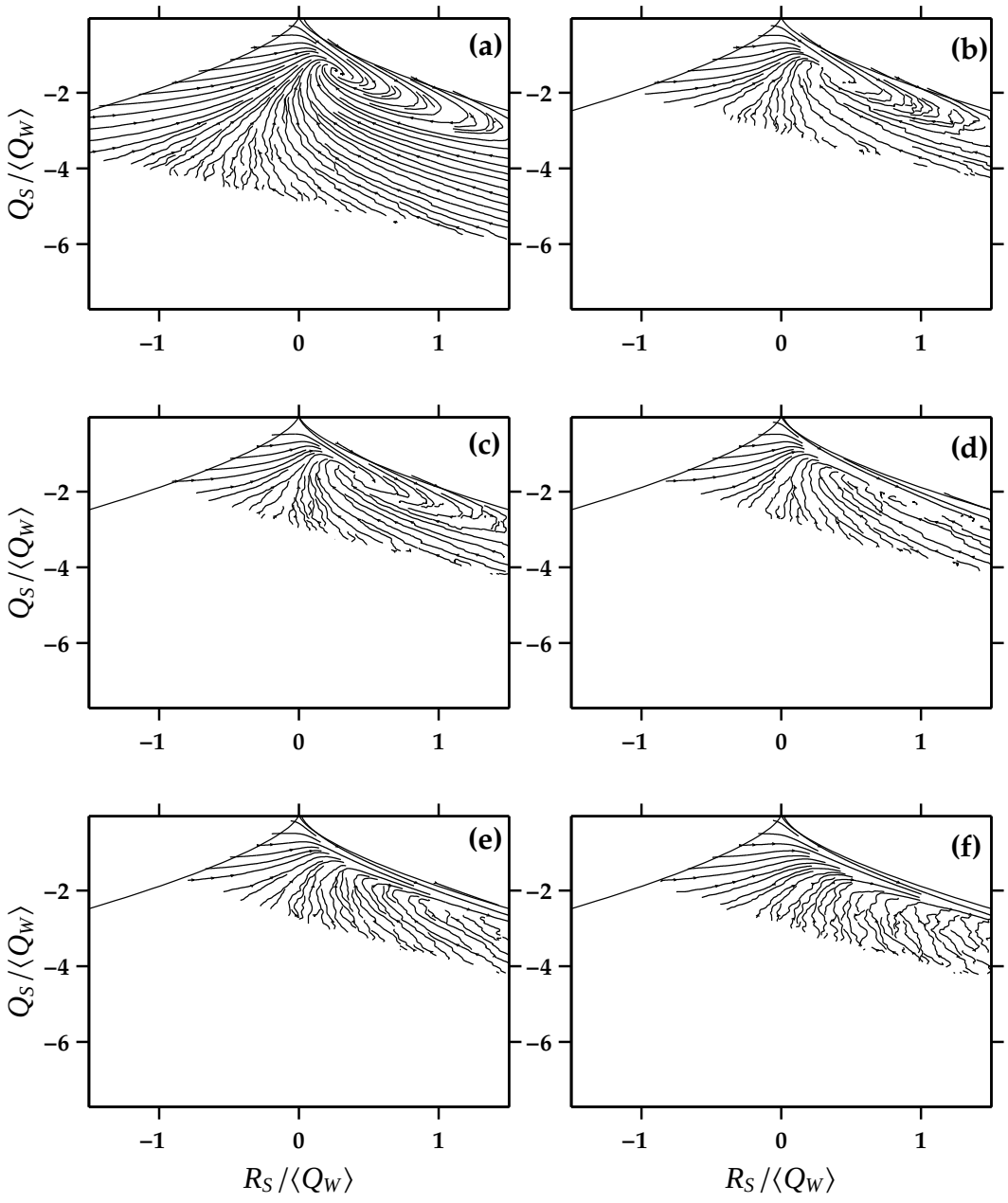

Figure 3.16: Conditional mean trajectories on the (R_S, Q_S) invariant plane for (a) $St = 0.025$, (b) $St = 0.1$, (c) $St = 0.2$, (d) $St = 0.5$, (e) $St = 1$, and (f) $St = 2$. Only regions with a number of samples $N_{R_S,Q_S} \geq 300$ are shown.

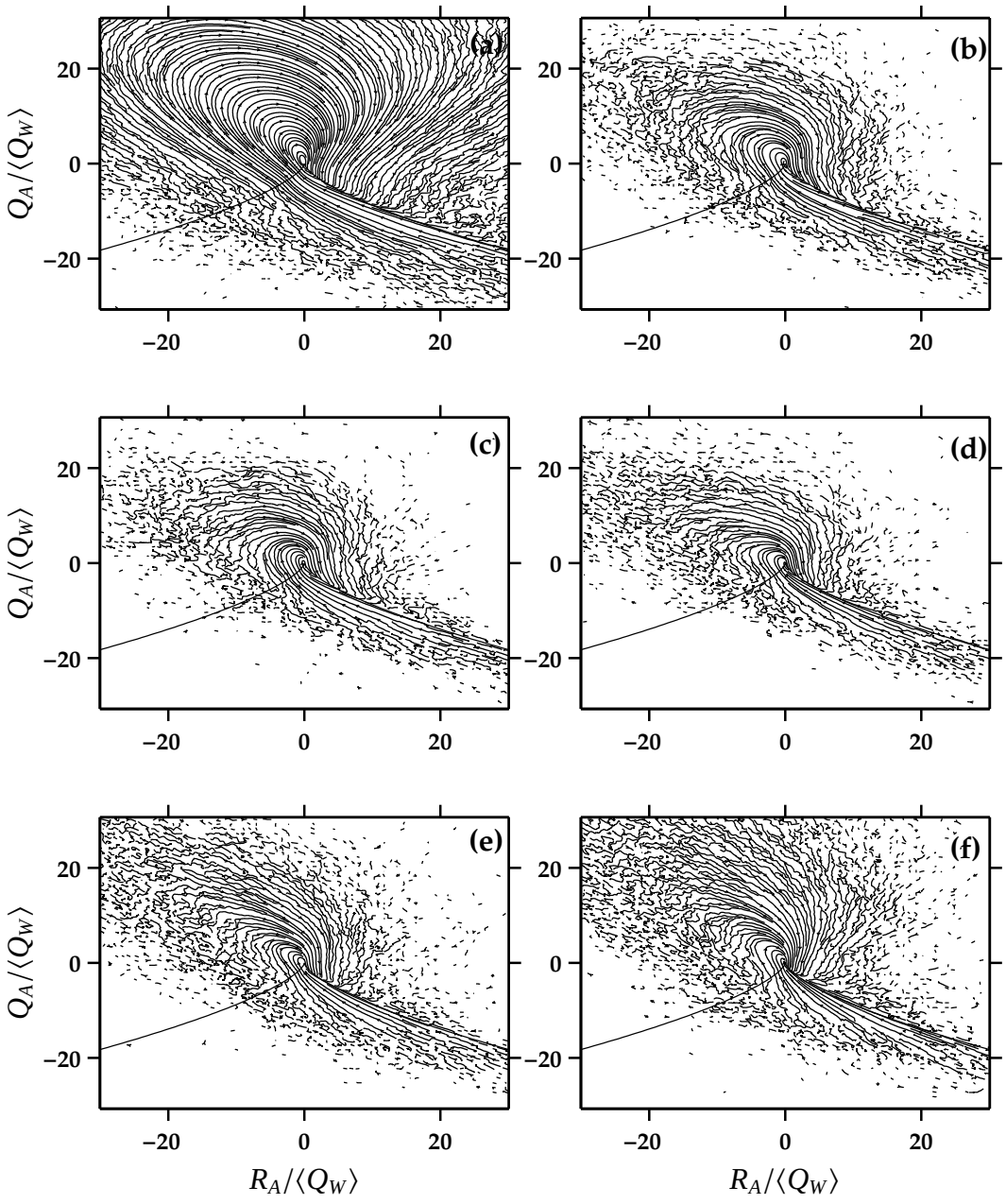

Figure 3.17: Conditional mean trajectories on the (R_A, Q_A) invariant plane for (a) $St = 0.025$, (b) $St = 0.1$, (c) $St = 0.2$, (d) $St = 0.5$, (e) $St = 1$, and (f) $St = 2$. No restriction on the number of samples N_{R_A,Q_A} is made.

ensemble is taken along inertial particle trajectories. This quantity is precisely $2\langle Q_W - Q_S \rangle$ as experienced by inertial particles. In the limit $St \to 0$ the theory presented in Chun et al. (2005) allows one to compute these statistics with knowledge only of fluid particle trajectories. An overview with the derivation of the main result of the theory is presented in §3.4. Collins & Keswani (2004) found that $\langle S^2 \rangle$ decreased with increasing R_λ and conjectured that clustering saturated at large R_λ. In Figure 3.18 we further extend the range of R_λ of that study and confirm its findings. Moreover, we note that $\langle S^2 \rangle$ for $St \ll 1$ not only decreases with R_λ but also goes below the respective value for fluid particles. This suggests that low inertia particles are ejected not only from regions of high rotation, but also from regions of high strain. A careful analysis of Figure 3.12 reveals that with increasing inertia particles are ejected from regions of overlapping high strain and high rotation, while there is an increase in the number of particles in regions of high strain and low rotation. Also shown in the figure is the result from the theory of Chun et al. (2005), which predicts the correct slope for $\langle S^2 \rangle$ and $\langle W^2 \rangle$. To the best knowledge of the authors, this result has not been reported previously.

3.4 Conclusions

The effect of filtering and biased sampling on inertial particle acceleration has been studied. In particular, we find that biased sampling does not capture the complete effect of the particle inertia, even at low Stokes numbers. The effect of biased filtering, i.e., the dependence of the acceleration time scale on the magnitude of the acceleration event, is also important, especially for higher order moments. Our results confirm the findings in Ayyalasomayajula et al. (2008),

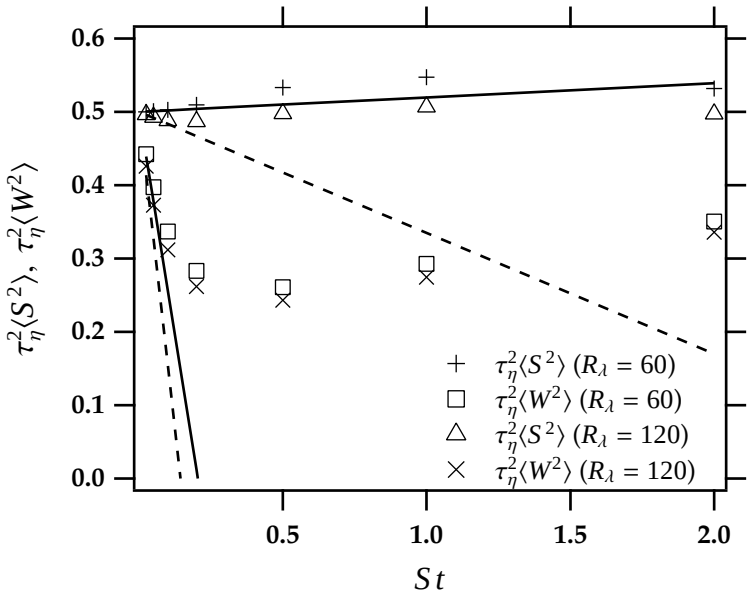

Figure 3.18: Second invariants of the strain and rotation-rate tensors as a function of St. The solid and dashed lines are predictions from the theory presented in Chun et al. (2005) for $R_\lambda = 60$ and $R_\lambda = 120$ respectively.

and highlight the need for models that incorporate aspects of flow structure. In order to better understand how acceleration is related to flow topology, we compute invariants of the velocity-gradient tensor, the strain-rate and rotation-rate tensor along particle trajectories. The joint PDFs of invariant pairs along with acceleration contour plots on invariant planes allow us to compute the contribution of specific flow topologies to the acceleration moments. We find further confirmation that inertial particles are ejected from regions of high-rotation and that these contribute the least to the acceleration moments precisely as clustering or preferential concentration peaks at $St \approx 0.7$ (Sundaram & Collins 1997). Following the methodology presented in Ooi et al. (1999), we compute conditional mean trajectories on the invariant planes for inertial particles for the first time. These trajectories represent the mean displacement of particles on the invariant plane and in principle do not correspond to actual individual particle

trajectories. Nonetheless, they are useful in providing a picture for the evolution of flow topology. Interesting findings include the existence of a stable focus in the invariant plane formed by the second invariant of the strain-rate and rotation-rate tensor. The unstable focus in the invariant plane formed by the second and third invariants of the strain-rate tensor reported in Ooi et al. (1999) has been found to be stable in our study. In addition we extend the R_λ range presented in the investigation of Collins & Keswani (2004), where the conjecture was made that inertial particle clustering saturates at high R_λ. Our results support this contention and moreover, we find that for $St < 0.5$ inertial particles on average sample less strain than fluid particles. We believe this work will contribute to a better understanding of the effects of inertia on acceleration and how flow topology relates to the latter.

This work was supported by the National Science Foundation under grant CBET-0756510. J.P.L.C.S. acknowledges support from the Brazilian Ministry of Education through the CAPES agency.

APPENDIX

Let P be the probability of a given point and let averages be defined as

$$\langle \phi \rangle_p = \int_V \phi P d\mathbf{x} \,, \tag{3.21}$$

where ϕ is an arbitrary quantity. The assumption is that P for fluid points is constant ($P = 1/V$), which implies a uniform weighting. The governing equation for P is

$$\frac{\partial P}{\partial t} + \frac{\partial P v_i}{\partial x_i} = 0 \,, \tag{3.22}$$

under the assumption that the particles are non-diffusing. Note that this expression is general, so long as v_i is the velocity of the particle of interest. Therefore this applies equally to fluid particles (in which $v_i = u_i$) as well as inertial particles. The expression above can be rearranged as follows

$$\frac{\partial P}{\partial t} + v_i \frac{\partial P}{\partial x_i} = -P \frac{\partial v_i}{\partial x_i} \,. \tag{3.23}$$

Next we apply a perturbation expansion for the probability and velocity in terms of the particle Stokes number

$$P = P^{(0)} + St P^{(1)} + \cdots \,, \tag{3.24}$$

$$v_i = v_i^{(0)} + St v_i^{(1)} + \cdots \,. \tag{3.25}$$

The equation of motion for the particles is

$$\frac{dv_i}{dt} = \frac{u_i - v_i}{\tau_p} \,, \tag{3.26}$$

which can be written as

$$St \frac{dv_i}{dt} = \frac{u_i - v_i}{\tau_\eta} \,. \tag{3.27}$$

Substituting the asymptotic expansion and evaluating orders yields

$$St^0 : v_i^{(0)} = u_i \,, \tag{3.28}$$

$$St^1 : \frac{dv_i^{(0)}}{dt} = -\frac{v_i^{(1)}}{\tau_\eta} \,. \tag{3.29}$$

Substituting the first result into the second gives

$$v_i^{(1)} = -\tau_\eta \frac{du_i}{dt} \,, \tag{3.30}$$

where the RHS involves the *Lagrangian* derivative. The RHS can be evaluated by taking the divergence of Eq. (3.30)

$$\frac{\partial v_i^{(1)}}{\partial x_i} = -\tau_\eta \frac{\partial}{\partial x_i}\left[\frac{\partial u_i}{\partial t} + u_j \frac{\partial u_i}{\partial x_j}\right] = -\tau_\eta \frac{\partial u_j}{\partial x_i}\frac{\partial u_i}{\partial x_j} \,. \tag{3.31}$$

Defining the rate-of-strain and rate-of-rotation tensors as follows

$$S_{ij} \equiv \frac{1}{2}\left(\frac{\partial u_j}{\partial x_i} + \frac{\partial u_i}{\partial x_j}\right) \,, \tag{3.32}$$

$$W_{ij} \equiv \frac{1}{2}\left(\frac{\partial u_j}{\partial x_i} - \frac{\partial u_i}{\partial x_j}\right) \,, \tag{3.33}$$

we can express the velocity divergence as follows

$$\frac{\partial v_i^{(1)}}{\partial x_i} = -\tau_\eta (S^2 - W^2) \,, \tag{3.34}$$

where $S^2 \equiv S_{ij}S_{ij}$ and $W^2 \equiv W_{ij}W_{ij}$.

Next we apply the perturbation expansion to Eq. (3.23)

$$St^0 : \frac{\partial P^{(0)}}{\partial t} + u_i \frac{\partial P^{(0)}}{\partial x_i} = -P^{(0)}\frac{\partial u_i}{\partial x_i} = 0 \,, \tag{3.35}$$

$$St^1 : \frac{\partial P^{(1)}}{\partial t} + u_i \frac{\partial P^{(1)}}{\partial x_i} + v_i^{(1)}\frac{\partial P^{(0)}}{\partial x_i} = -P^{(1)}\frac{\partial u_i}{\partial x_i} - P^{(0)}\frac{\partial v_i^{(1)}}{\partial x_i} \,. \tag{3.36}$$

We can simplify the second equation using continuity and the fact that $P^{(0)}$ is constant to obtain

$$\frac{\partial P^{(1)}}{\partial t} + u_i \frac{\partial P^{(1)}}{\partial x_i} = -P^{(0)}\frac{\partial v_i^{(1)}}{\partial x_i} \,, \tag{3.37}$$

which we can express in terms of the substantial derivative as follows

$$\frac{dP^{(1)}}{dt} = -P^{(0)}\frac{\partial v_i^{(1)}}{\partial x_i} \,. \tag{3.38}$$

Substituting Eq. (3.34)

$$\frac{dP^{(1)}}{dt} = P^{(0)}\tau_\eta(S^2 - W^2) \tag{3.39}$$

We can formally integrate this (along a *fluid* particle trajectory) to yield

$$\therefore\ P^{(1)} = P^{(0)}\tau_\eta \int_{-\infty}^{t} \left[S^2(s) - W^2(s)\right] ds \tag{3.40}$$

We now have the tools to compute averages. We define the unweighted and weighted averages, respectively

$$\langle\phi\rangle = \int \phi(t)P^{(0)}d\mathbf{x} \,, \tag{3.41}$$

$$\langle\phi\rangle_p = \int \phi(t)Pd\mathbf{x} \,. \tag{3.42}$$

Substituting the asymptotic expansion $P = P^{(0)} + StP^{(1)} + \cdots$ into the second expression

$$\langle\phi\rangle_p = \langle\phi\rangle + St\tau_\eta \int_{-\infty}^{t} \langle\phi(t)\left[S^2(s) - W^2(s)\right]\rangle ds \,. \tag{3.43}$$

We can express this as

$$\begin{aligned}\langle\phi\rangle_p =& \langle\phi\rangle + St\tau_\eta \int_{-\infty}^{t} \langle[\phi(t) - \langle\phi\rangle]\left[S^2(s) - \langle S^2\rangle\right]\rangle ds \\ &- St\tau_\eta \int_{-\infty}^{t} \langle[\phi(t) - \langle\phi\rangle]\left[W^2(s) - \langle W^2\rangle\right]\rangle ds \,,\end{aligned} \tag{3.44}$$

since $\langle S^2\rangle = \langle W^2\rangle = \epsilon/2\nu$. We then define the correlation coefficient as

$$\rho_{XY}(t) \equiv \frac{\langle X'(0)Y'(t)\rangle}{\sigma_X\sigma_Y} \,, \tag{3.45}$$

where $X' = X - \langle X\rangle$, $Y' = Y - \langle Y\rangle$, $\sigma_X = \sqrt{\langle X'^2\rangle}$ and $\sigma_Y = \sqrt{\langle Y'^2\rangle}$. Substituting into Eq. (3.44) yields

$$\langle\phi\rangle_p = \langle\phi\rangle + \tau_\eta St\sigma_\phi\sigma_{S^2} \int_{-\infty}^{t} \rho_{S^2\phi}(t-s)ds - \tau_\eta St\sigma_\phi\sigma_{W^2} \int_{-\infty}^{t} \rho_{W^2\phi}(t-s)ds \,. \tag{3.46}$$

Letting $\tau = t - s$ and $d\tau = -ds$ we have following rearrangement

$$\langle \phi \rangle_p = \langle \phi \rangle + \tau_\eta S\, t \sigma_\phi \sigma_{S^2} \int_0^\infty \rho_{S^2\phi}(\tau) d\tau - \tau_\eta S\, t \sigma_\phi \sigma_{W^2} \int_0^\infty \rho_{W^2\phi}(\tau) d\tau \ . \tag{3.47}$$

We then define time correlations

$$T_{XY} = \int_0^\infty \rho_{XY}(t) dt \ . \tag{3.48}$$

Substituting yields the final expression

$$\therefore \ \langle \phi \rangle_p = \langle \phi \rangle + \tau_\eta \sigma_\phi S\, t \left(\sigma_{S^2} T_{S^2\phi} - \sigma_{W^2} T_{W^2\phi} \right) \ . \tag{3.49}$$

REFERENCES

Ashurst WT, Kerstein AR, Kerr RM, Gibson CH. 1987. Alignment of vorticity and scalar gradient with strain rate in simulated navier-stokes turbulence. *Phys. Fluids* 30:2343–2353

Ayyalasomayajula S, Gylfason A, Collins LR, Bodenschatz E, Warhaft Z. 2006. Lagrangian measurements of inertial particle accelerations in grid generated wind tunnel turbulence. *Phys. Rev. Lett.* 97:144507

Ayyalasomayajula S, Warhaft Z, Collins LR. 2008. Modeling inertial particle acceleration statistics in isotropic turbulence. *Phys. Fluids* 20:095104

Batchelor GK. 1953. *The Theory of Homogeneous Turbulence*. Cambridge: Cambridge University Press

Bec J, Biferale L, Boffetta G, Celani A, Cencini M, et al. 2006. Acceleration statistics of heavy particles in turbulence. *J. Fluid Mech.* 550:349–358

Bec J, Biferale L, Cencini M, Lanotte A, Musacchio S, Toschi F. 2007. Heavy particle concentration in turbulence at dissipative and inertial scales. *Phys. Rev. Lett.* 98:084502

Benzi R, Biferale L, Calzavarini E, Lohse D, Toschi F. 2009. Velocity-gradient statistics along particle trajectories in turbulent flows: The refined similarity hypothesis in the lagrangian frame. *Phys. Rev. E* 80:066318

Berg J, Lüthi B, Mann J, Ott S. 2006. Backwards and forwards relative dispersion in turbulent flow: An experimental investigation. *Phys. Rev. E* 74:016304

Berg J, Ott S, Mann J, Luthi B. 2009. Experimental investigation of lagrangian structure functions in turbulence. *Phys. Rev. E* 80:026316

Berrut JP, Trefethen LN. 2004. Barycentric lagrange interpolation. *Siam Rev.* 46:501–517

Betchov R. 1956. An inequality concerning the production of vorticity in isotropic turbulence. *J. Fluid Mech.* 1:497–504

Biferale L, Bodenschatz E, Cencini M, Lanotte A, Ouellette NT, et al. 2008. Lagrangian structure functions in turbulence: A quantitative comparison between experiment and direct numerical simulation. *Phys. Fluids* 20:065103

Biferale L, Boffetta G, Celani A, Devenish BJ, Lanotte A, Toschi F. 2004. Multifractal statistics of Lagrangian velocity and acceleration in turbulence. *Phys. Rev. Lett.* 93:064502

Biferale L, Boffetta G, Celani A, Devenish BJ, Lanotte A, Toschi F. 2005. Lagrangian statistics of particle pairs in homogeneous isotropic turbulence. *Phys. Fluids* 17:115101

Blackburn HM, Mansour NN, Cantwell BJ. 1996. Topology of fine-scale motions in turbulent channel flow. *J. Fluid Mech.* 310:269–292

Bourgoin M, Ouelette NT, Xu H, Berg J, Bodenschatz E. 2006. The role of pair dispersion in turbulent flow. *Science* 311:835–838

Brown RD, Warhaft Z, Voth GA. 2009. Acceleration statistics of neutrally buoyant spherical particles in intense turbulence. *Phys. Rev. Lett.* 103:194501

Brucker KA, Isaza JC, Vaithianathan T, Collins LR. 2007. Efficient algorithm for simulating homogeneous turbulent shear flow without remeshing. *J. Comp. Phys.* 225:20–32

Calzavarini E, Volk R, Bourgoin M, Leveque E, Pinton JF, Toschi F. 2009. Acceleration statistics of finite-sized particles in turbulent flow: the role of faxen forces. *J. Fluid Mech.* 630:179–189

Cantwell BJ. 1992. Exact solution of a restricted euler equation for the velocity-gradient tensor. *Phys. Fluids A* 4:782–793

Cantwell BJ. 1993. On the behavior of velocity-gradient tensor invariants in direct numerical simulations of turbulence. *Phys. Fluids A* 5:2008–2013

Chacin JM, Cantwell BJ. 2000. Dynamics of a low reynolds number turbulent boundary layer. *J. Fluid Mech.* 404:87–115

Chacin JM, Cantwell BJ, Kline SJ. 1996. Study of turbulent boundary layer structure using the invariants of the velocity gradient tensor. *Exp. Therm. and Fluid Sci.* 13:308–317

Chen L, Goto S, Vassilicos JC. 2006. Turbulent clustering of stagnation points and inertial particles. *J. Fluid Mech.* 553:143–154

Chong MS, Perry AE, Cantwell BJ. 1990. A general classification of three-dimensional flow fields. *Phys. Fluids A* 2:765–777

Chong MS, Soria J, Perry AE, Chacin J, Cantwell BJ, Na Y. 1998. Turbulence structures of wall-bounded shear flows found using dns data. *J. Fluid Mech.* 357:225–247

Chun J, Koch DL, Rani S, Ahluwalia A, Collins LR. 2005. Clustering of aerosol particles in isotropic turbulence. *J. Fluid Mech.* 536:219–251

Coleman SW, Vassilicos JC. 2009. A unified sweep-stick mechanism to explain

particle clustering in two- and three-dimensional homogeneous, isotropic turbulence. *Phys. Fluids* 21:113301

Collins LR, Keswani A. 2004. Reynolds number scaling of particle clustering in turbulent aerosols. *New J. Phys.* 6:119

da Silva CB, Pereira JCF. 2008. Invariants of the velocity-gradient, rate-of-strain, and rate-of-rotation tensors across the turbulent/nonturbulent interface in jets. *Phys. Fluids* 20:055101

Davidson PA. 2004. *Turbulence: an introduction for scientists and engineers*. Oxford

Eaton JK, Fessler JR. 1994. Preferential concentration of particles by turbulence. *Int. J. Multiphase Flow* 20:169–209

Elghobashi S. 2006. An updated classification map of particle-laden turbulent flows. In *IUTAM Symposium on Computational Approaches to Multiphase Flow*, eds. S Balachandar, A Prosperetti, Fluid Mechanics and Its Applications. Springer Netherlands, 3–10

Gerashchenko S, Sharp NS, Neuscamman S, Warhaft Z. 2008. Lagrangian measurements of inertial particle accelerations in a turbulent boundary layer. *J. Fluid Mech.* 617:255–281

Gibert M, Xu H, Bodenschatz E. 2009. Inertial effects on two-particle relative dispersion in turbulent flows. *Europhys. Lett.* Submitted

Girimaji SS, Pope SB. 1990. Material-element deformation in isotropic turbulence. *J. Fluid Mech* 220:427–458

Goto S, Kida S. 2003. Enhanced stretching of material lines by antiparallel vortex pairs in turbulence. *Fluid Dyn. Res.* 33:403–431

Goto S, Vassilicos JC. 2008. Sweep-stick mechanism of heavy particle clustering in fluid turbulence. *Phys. Rev. Lett.* 100:035504

Gotoh T, Fukayama D, Nakano T. 2002. Velocity field statistics in homogeneous steady turbulence obtained using a high-resolution direct numerical simulation. *Phys. Fluids* 14:1065–1081

Gulitski G, Kholmyansky M, Kinzelbach W, Luthi B, Tsinober A, Yorish S. 2007. Velocity and temperature derivatives in high-reynolds-number turbulent flows in the atmospheric surface layer. part 1. facilities, methods and some general results. *J. Fluid Mech.* 589:57–81

Gylfason A, Ayyalasomayajula S, Warhaft Z. 2004. Intermittency, pressure and acceleration statistics from hot-wire measurements in wind-tunnel turbulence. *J. Fluid Mech.* 501:213–229

IJzermans RHA, Reeks MW, Meneguz E, Picciotto M, Soldati A. 2009. Measuring segregation of inertial particles in turbulence by a full lagrangian approach. *Phys. Rev. E* 80:015302

Ishihara T, Kaneda Y, Yokokawa M, Itakura K, Uno A. 2007. Small-scale statistics in high-resolution direct numerical simulation of turbulence: Reynolds number dependence of one-point velocity gradient statistics. *J. Fluid Mech.* 592:335–366

Jimenez J, Wray AA, Saffman PG, Rogallo RS. 1993. The structure of intense vorticity in isotropic turbulence. *J. Fluid Mech.* 255:65–90

Jung J, Yeo K, Lee C. 2008. Behavior of heavy particles in isotropic turbulence. *Phys. Rev. E* 77:016307

Kaneda Y, Ishihara T. 2006. High-resolution direct numerical simulation of turbulence. *J. Turbulence* 7:1–17

Kerr RM. 1985. Higher-order derivative correlations and the alignment of small-scale structures in isotropic numerical turbulence. *J. Fluid Mech.* 153:31–58

Kerr RM. 1987. Histograms of helicity and strain in numerical turbulence. *Phys. Rev. Lett.* 59:783–786

La Porta A, Voth GA, Crawford AM, Alexander J, Bodenschatz E. 2001. Fluid particle accelerations in fully developed turbulence. *Nature* 409:1017–1019

Lavezzo V, Soldati A, Warhaft Z, Collins LR. 2009. High-inertia particle acceleration statistics in a turbulent channel flow. *J. Fluid Mech.* In review.

Lüthi B, Ott S, Berg J, Mann J. 2007. Lagrangian multi-particle statistics. *J. Turbulence* 8:N45

Lüthi B, Tsinober A, Kinzelbach W. 2005. Lagrangian measurement of vorticity dynamics in turbulent flow. *J. Fluid Mech.* 528:87–118

Malik NA, Dracos T, Papantoniou D. 1993. Partile tracking velocimetry in three-dimensional flows. Part II: Particle tracking. *Exp. Fluids* 15:279–294

Maxey MR. 1987. The gravitational settling of aerosol particles in homogeneous turbulence and random flow fields. *J. Fluid Mech.* 174:441–465

Maxey MR, Riley JJ. 1983. Equation of motion for a small rigid sphere in a nonuniform flow. *Phys. Fluids* 26:883–889

Moisy F, Jimenez J. 2004. Geometry and clustering of intense structures in isotropic turbulence. *J. Fluid Mech.* 513:111–133

Mordant N, Crawford AM, Bodenschatz E. 2004a. Experimental lagrangian acceleration probability density function measurement. *Physica D* 193:245–251

Mordant N, Crawford AM, Bodenschatz E. 2004b. Three-dimensional structure of the lagrangian acceleration in turbulent flows. *Phys. Rev. Lett.* 93:214501

Ooi A, Martin J, Soria J, Chong MS. 1999. A study of the evolution and characteristics of the invariants of the velocity-gradient tensor in isotropic turbulence. *J. Fluid Mech.* 381:141–174

Ott S, Mann J. 2000. An experimental investigation of the relative diffusion of particle pairs in three-dimensional turbulent flow. *J. Fluid Mech.* 422:207–223

Ouellette NT, Xu H, Bodenschatz E. 2006a. A quantitative study of three-dimensional particle tracking algorithms. *Exp. Fluids* 40:301–313

Ouellette NT, Xu H, Burgoin M, Bodenschatz E. 2006b. An experimental study of turbulent relative dispersion models. *New J. Phys.* 8:109

Pope SB. 1985. Pdf methods for turbulent reactive flows. *Prog. Energy Combust. Sci.* 11:119–192

Pope SB. 1994. Lagrangian PDF methods for turbulent flows. *Ann. Rev. Fluid Mech.* 26:23–63

Pope SB. 2002. A stochastic lagrangian model for acceleration in turbulent flows. *Phys. Fluids* 14:2360–2375

Qureshi NM, Arrieta U, Baudet C, Cartellier A, Gagne Y, Bourgoin M. 2008. Acceleration statistics of inertial particles in turbulent flow. *Eur. Phys. J. B* 66:531–536

Reade WC, Collins LR. 2000. Effect of preferential concentration on turbulent collision rates. *Phys. Fluids* 12:2530–2540

Reynolds AM, Mordant N, Crawford AM, Bodenschatz E. 2005. On the distribution of lagrangian accelerations in turbulent flows. *New J. Phys.* 7:58

Salazar JPLC, Collins LR. 2009. Two-particle dispersion in isotropic turbulent flows. *Ann. Rev. Fluid Mech.* 41:405–432

Salazar JPLC, De Jong J, Cao LJ, Woodward SH, Meng H, Collins LR. 2008. Experimental and numerical investigation of inertial particle clustering in isotropic turbulence. *J. Fluid Mech.* 600:245–256

Saw EW, Shaw RA, Ayyalasomayajula S, Chuang PY, Gylfason A. 2008. Inertial clustering of particles in high-reynolds-number turbulence. *Phys. Rev. Lett.* 100:214501

Sawford BL. 1991. Reynolds number effects in lagrangian stochastic models of turbulent dispersion. *Phys. Fluids A* 3:1577–1586

Sawford BL. 2001. Turbulent relative dispersion. *Ann. Rev. Fluid Mech.* 33:289–317

Sawford BL, Yeung PK, Borgas MS, La Porta PVA, Crawford AM, Bodenschatz E. 2003. Conditional and unconditional acceleration statistics in turbulence. *Phys. Fluids* 15:3478–3489

Shaw RA, Reade WC, Collins LR, Verlinde J. 1998. Preferential concentration of cloud droplets by turbulence: effects on the early evolution of cumulus cloud droplet spectra. *J. Atmos. Sci.* 55:1965–1976

She Z, Jackson E, Orszag SA. 1991. Structure and dynamics of homogeneous turbulence: models and simulations. *Proc. R. Soc. Lond. A* 434:101–124

Siggia ED. 1981. Numerical study of small-scale intermittency in three-dimensional turbulence. *J. Fluid Mech.* 107:375–406

Soria J, Sondergaard R, Cantwell BJ, Chong MS, Perry AE. 1994. A study of the fine-scale motions of incompressible time-developing mixing layers. *Phys. Fluids* 6:871–884

Squires KD, Eaton JK. 1991a. Measurements of particle dispersion from direct numerical simulations of isotropic turbulence. *J. Fluid Mech.* 226:1–35

Squires KD, Eaton JK. 1991b. Preferential concentration of particles by turbulence. *Phys. Fluids A* 3:1169–1178

Sreenivasan KR, Antonia RA. 1997. The phenomenology of small-scale turbulence. *Ann. Rev. Fluid Mech.* 29:435–72

Sundaram S, Collins LR. 1997. Collision statistics in an isotropic, particle-laden turbulent suspension i. direct numerical simulations. *J. Fluid Mech.* 335:75–109

Taylor GI. 1938. Production and dissipation of vorticity in a turbulent fluid. *Proc. Roy. Soc. Lond. A Mat.* 164:15–23

Tennekes H, Lumley JL. 1972. *A first course in turbulence*. Cambridge: MIT Press

Toschi F, Bodenschatz E. 2009. Lagrangian properties of fully developed turbulence. *Ann. Rev. Fluid Mech.* 41:375–404

Townsend AA. 1951. The diffusion of heat spots in isotropic turbulence. *Proc. R. Soc. Lond. A* 209:418–430

Tsinober A, Kit E, Dracos T. 1992. Experimental investigation of the field of velocity-gradients in turbulent flows. *J. Fluid Mech.* 242:169–192

Vedula P, Yeung PK. 1999. Similarity scaling of acceleration and pressure statistics in numerical simulations of isotropic turbulence. *Phys. Fluids* 11:1208–1220

Vincent A, Meneguzzi M. 1991. The spatial structure and statistical properties of homogeneous turbulence. *J. Fluid Mech.* 225:1–20

Virant M, Dracos T. 1997. 3d ptv and its application to lagrangian motion. *Meas. Sci. Tech.* 8:1539–1552

Volk R, Calzavarini E, Verhille G, Lohse D, Mordant N, et al. 2008. Acceleration of heavy and light particles in turbulence: Comparison between experiments and direct numerical simulations. *Physica D* 237:2084–2089

Voth GA, La Porta A, Crawford AM, Alexander J, Bodenschatz E. 2002. Measurement of particle accelerations in fully developed turbulence. *J. Fluid Mech.* 469:121–160

Voth GA, Satyanarayan K, Bodenschatz E. 1998. Lagrangian acceleration measurements at large reynolds numbers. *Phys. Fluids* 10:2268–2280

Wang LP, Maxey MR. 1993. Settling velocity and concentration distribution of heavy particles in homogeneous isotropic turbulence. *J. Fluid Mech.* 256:27–68

Wood AM, Hwang W, Eaton JK. 2005. Preferential concentration of particles in homogeneous and isotropic turbulence. *Int. J. Multiphase Flow* 31:1220–1230

Xu H, Bodenschatz E. 2008. Motion of inertial particles with size larger than kolmogorov scale in turbulent flows. *Physica D* 237:2095–2100

Xu H, Bourgoin M, Ouellette NT, Bodenschatz E. 2006a. High order lagrangian velocity statistics in turbulence. *Phys. Rev. Lett.* 96:024503

Xu H, Ouellette NT, Bodenschatz E. 2006b. Multifractal dimension of lagrangian turbulence. *Phys. Rev. Lett.* 96:114503

Xu H, Ouellette NT, Bodenschatz E. 2008. Evolution of geometric structures in intense turbulence. *New J. Phys.* 10:013012

Yeung PK. 1994. Direct numerical simulation of two-particle relative diffusion in isotropic turbulence. *Phys. Fluids A* 6:3416

Yeung PK. 1997. One- and two-particle Lagrangian acceleration correlations in numerically simulated homogeneous turbulence. *Phys. Fluids* 9:2981–2990

Yeung PK. 2001. Lagrangian characteristics of turbulence and scalar transport in direct numerical simulations. *J. Fluid Mech.* 427:241–274

Yeung PK. 2002. Lagrangian investigations of turbulence. *Ann. Rev. Fluid Mech.* 34:115–142

Yeung PK, Borgas MS. 2004. Relative dispersion in isotropic turbulence. part 1. direct numerical simulations and reynolds-number dependence. *J. Fluid Mech.* 503:93–124

Yeung PK, Pope SB. 1989. Lagrangian statistics from direct numerical simulations of isotropic turbulence. *J. Fluid Mech.* 207:531–586

Yeung PK, Pope SB, Kurth EA, Lamorgese AG. 2007. Lagrangian conditional statistics, acceleration and local relative motion in numerically simulated isotropic turbulence. *J. Fluid Mech.* 582:399–422

Yeung PK, Pope SB, Lamorgese AG, Donzis DA. 2006a. Acceleration and dissipation statistics of numerically simulated isotropic turbulence. *Phys. Fluids* 18:065103

Yeung PK, Pope SB, Sawford BL. 2006b. Reynolds number dependence of Lagrangian statistics in large numerical simulations of isotropic turbulence. *J. Turbulence* 7:1–12

Zaichik LI, Alipchenkov VM. 2008. Acceleration of heavy particles in isotropic turbulence. *Int. J. Multiphase Flow* 34:865–868